REINDEER

D4.1

System design study for energy-neutral devices interacting with the RadioWeaves infrastructure

Project number:	101013425
Project acronym:	**REINDEER**
Project title:	REsilient INteractive applications through hyper Diversity in Energy Efficient RadioWeaves technology
Project Start Date:	1st January, 2021
Duration:	42 months
Programme:	H2020-ICT-52-2020
Deliverable Type:	Report
Reference Number:	ICT-52-2020 / D4.1 / 1.00
Workpackage:	WP 4
Due Date:	30th September, 2022
Actual Submission Date:	10th October, 2022
Responsible Organisation:	TU GRAZ
Editor:	Benjamin J. B. Deutschmann
Dissemination Level:	PU
Revision:	1.00
Abstract:	This document provides fundamental performance limits of a RadioWeaves infrastructure with respect to the interaction with energy neutral devices. In particular, the maximum regulatory-compliant power budget and achievable initial access distance are derived, and backscatter communication schemes and data rates are discussed. Emphasis has been put on an efficiency model as well as a channel model representing wireless power transfer in a physically correct manner and the verification thereof using realistic measurements.
Keywords:	RF, WPT, array near field, energy neutral devices, DMIMO

The REINDEER project has received funding from the European Union's Horizon 2020 research and innovation programme under grant agreement No 101013425.

Editor

Benjamin J. B. Deutschmann (TU GRAZ)

Contributors (ordered according to beneficiary numbers)

Chesney Buyle, Bert Cox, Daan Delabie (KU Leuven)

Benjamin J. B. Deutschmann, Maximilian Graber, Thomas Wilding, Klaus Witrisal (TU GRAZ)

Ulrich Mühlmann (NXP)

Internal reviewers

Erik G. Larsson (LIU), Liesbet Van der Perre (KU Leuven), Ahmet Kaplan (LIU)

Disclaimer

The information in this document is provided as is, and no guarantee or warranty is given that the information is fit for any particular purpose. The content of this document reflects only the author's view – the European Commission is not responsible for any use that may be made of the information it contains. The users use the information at their sole risk and liability.

Executive Summary

This deliverable examines the fundamental performance limits of a RadioWeaves infrastructure with respect to the interaction with energy neutral (EN) devices. In particular, the maximum regulatory-compliant power budget and achievable initial access distance are derived, and backscatter communication schemes and data rates are discussed. While batteryless ultra high frequency (UHF) radio frequency identification (RFID) tags exhibit read-ranges limited to a few meters and data rates in the $\mathrm{kbit/s}$ range, we demonstrate that RadioWeaves pushes these performance indicators by orders of magnitude.

We define an efficiency model that reflects the losses incurring in every individual building block of a complete wireless power transfer (WPT) system. Major gains are expected to be made in the RF-to-RF link due to the massive antenna deployment in a RadioWeaves infrastructure. Existing channel models do not sufficiently model array gains and signal amplitudes for radio frequency (RF) WPT in geometry-based environment models. Therefore, we derive a channel model capable of representing RF WPT in a physically correct manner such that the RF-to-RF transmission efficiency is accurately modeled. The channel model is verified by means of synthetic aperture measurements with a vector network analyzer (VNA), where results of both measurements and simulations show a close correspondence. With the ability of conducting realistic simulations, we have analyzed exemplary RadioWeaves deployments and found that this future distributed radio infrastructure shows several beneficial properties regarding regulatory compliance. Based on our findings, we derive the maximum regulatory-compliant power budget of EN devices at various sub-$10\,\mathrm{GHz}$ bands. Building upon the expertise on state-of-the-art RFID technology that is available within the REINDEER consortium, we are able to compute the achievable initial access distances for EN devices. Furthermore, we already propose a first initial access scheme and reveal how beam diversity can be exploited to overcome impairments due to strong multipath propagation. Our system analysis is rounded-off with a discussion of transponder architectures and performance evaluations thereof. Circuit-level simulations and RF measurements hint at typical efficiency limits of integrated transponder designs and reveal demanding design challenges (e.g., matching an antenna to a nonlinear rectifier impedance) that require particular attention for a high overall system efficiency.

With the WPT channel model derived and measurement procedures defined, we have set the stage for algorithmic developments which will strongly build on the realistic synthetic and measured data from our simulation framework and measurement testbeds, respectively. These algorithms will be published in the REINDEER deliverable D4.2 [43]. Our findings in this document reveal that many of the achievable gains of RadioWeaves rely on its geometric environment-awareness. Therefore, our algorithms for WPT will have a strong connection to algorithms for position estimation and environment learning that will be covered in deliverable D3.3 [42].

Contents

List of Acronyms

2D two-dimensional. 12

3D three-dimensional. 12

AFE analog front end. 48

AM amplitude modulation. 45

AR augmented reality. 33

ASK amplitude shift keying. VIII, 34

AWGN additive white Gaussian noise. 8

BER bit error rate. 37

CMOS complementary metal oxide semiconductor. 6

CSE channel state estimation. 31

CSI channel state information. 13

DAS distributed antenna systems. 27

DC direct current. 4

DM diffuse multipath. 8

EC European Commission. 17

EIRP equivalent isotropically radiated power. 16, 17

EN energy neutral. I, II, 1

ERP equivalent radiated power. 17

ESD electrostatic discharge. 46

ETSI European Telecommunications Standards Institute. 17

FDMA frequency division multiple access. 40

FEM finite element analysis. 52

FSK frequency shift keying. VIII, 34

GSM Global System for Mobile Communications. 1

IC integrated circuit. 46

IoT Internet of Things. 1

ISM industrial, scientific and medical. 16

JFET junction field effect transistor. 37

LoS line-of-sight. 8

LTI linear time-invariant. 5

MIMO multiple-input multiple-output. 12

MISO multiple-input single-output. 5

mmWave millimeter wave. 16, 27, 30

MN matching network. 48

MOSFET metal-oxide semiconductor field effect transistor. 48

MPC multipath component. 33

MRT maximum ratio transmission. 11

NFC near-field communication. 1

nMOS n-channel metal-oxide semiconductor. 6

OOK on-off keying. 38

PSK phase shift keying. VIII, 34

QAM quadrature amplitude modulation. 34

RCS radar cross section. VIII, 10

RF radio frequency. II, 3

RFID radio frequency identification. II, 1

RW RadioWeaves. 3

SAR specific absorption rate. 20

SMC specular multipath component. 8

SNR signal-to-noise ratio. 33

S-parameters scattering parameters. 5

SISO single-input single-output. 5

SRD short-range device. 17

TOSM through – open – short – match. 11

UHF ultra high frequency. II, 30

ULA uniform linear array. 11

URA uniform rectangular array. 24

UWB ultrawideband. 11

VNA vector network analyzer. II, 5

WB wideband. 46

WPT wireless power transfer. I, II, 2

XETS cross exponentially tapered slot. 11

List of Figures

List of Tables

Chapter 1

Introduction

Driving sustainability is an important success factor to transform today's society into a vivid realm. The semiconductor industry can support this ambition by minimizing the number of batteries needed to supply millions of Internet of Things (IoT) devices used worldwide. However, state-of-the-art communication technology does not provide a suitable platform to implement and interact with this type of energy neutral (EN) device infrastructure in an efficient way. Today, on the one hand, we have the Global System for Mobile Communications (GSM) technology with all its varieties reaching from 2G to 5G, which, together with near-field communication (NFC), Wi-Fi and Bluetooth, used for short range communication and human interaction, comprises the key foundation of modern wireless connectivity. On the other hand, we have industry standards regulating the use of radio frequency identification (RFID) tags not only applied in small shops or warehouses but also utilized in large-scale distribution centers helping to organize the transport of food and goods around the globe. Tags used in the supply chain management system are EN devices in the basic sense. Hence, it is obvious that this kind of technology can form the basic asset to leverage the objectives of this project building an EN device infrastructure enabling a new set of use-cases for the next generations to come. Therefore, it is key do derive fundamental requirements and architectures on how these EN devices can supplement wireless connectivity in 6G and beyond.

The interaction with EN devices deployed at massive scale is a targeted feature of a RadioWeaves infrastructure. It enables efficient, resilient, yet cost-effective and sustainable opportunities for future use cases in the realms of IoT, Industry 4.0, logistics, healthcare, and many more [14]. The functional and computational capabilities of new generations of EN devices will go far beyond what is achieved with state-of-the-art RFID tags today: Leveraging the achievable gains of a distributed radio architecture with massive apertures lifts the available power budgets to unprecedented levels. Allowing the integration of on-device sensors, actuators and capable processors will map future use cases to the digital domain. The distributed computing abilities of RadioWeaves shift the computational burden from the device-side to the infrastructure-side, resulting in less complex EN devices and more affordable, sustainable deployments. This deliverable investigates the fundamental achievable gains and validates envisioned paradigm shifts necessary to turn this vision into a reality.

This document is dedicated not only to the definition of requirements but also it discusses new opportunities regarding the innovative RadioWeaves infrastructure.
The individual chapters first examine the state-of-the-art and demonstrate the achievable gains and paradigm shifts achievable with a future distributed radio architecture like RadioWeaves.

We analyze the fundamental building blocks of a wireless power transfer (WPT) system in Section 2.1. On top of that we derive a WPT channel model to compute the achievable gains of a RadioWeaves infrastructure in Section 2.2 and validate the model through realistic real-life measurements in Section 2.3.
The investigation of regulatory compliance limits plays a central role in the design of any WPT system, as they define the upper bounds of the transmittable and receivable power. We list applicable regulations in Section 3.1, and investigate the regulatory compliance of distributed, or physically large radio infrastructures in Section 3.2.
After defining a realistic system and channel model, and having regulations examined, we derive the maximum regulatory-compliant power budget in Section 4.1. Energy-efficient communication schemes suitable for low-power EN devices are discussed and achievable data rates are analyzed in Section 4.2.
In Section 5, circuit level simulations are conducted along with measurements of complete semiconductor chips to demonstrate the feasibility of manufacturing real-life EN devices and unveil the associated challenges.

Chapter 2

System efficiency and channel model

This chapter establishes an efficiency model for radio frequency (RF) wireless power transfer in a RadioWeaves (RW) environment. It serves as a basis to derive power budget and performance analyses for the operation of EN devices in RW. The chapter is organized into three sections. Section 2.1 discusses the main building blocks of a complete RF wireless power transfer system and associated efficiencies. The channel model of an RW infrastructure, which directly correlates with the RF-to-RF transmission efficiency, is covered in Section 2.2. In the last section, the proposed RW channel model is validated through realistic real-life measurements. Chapter 5 further focuses on the hardware requirements and practical efficiencies of the energy harvesting circuits at the EN device side.

2.1 Efficiency model

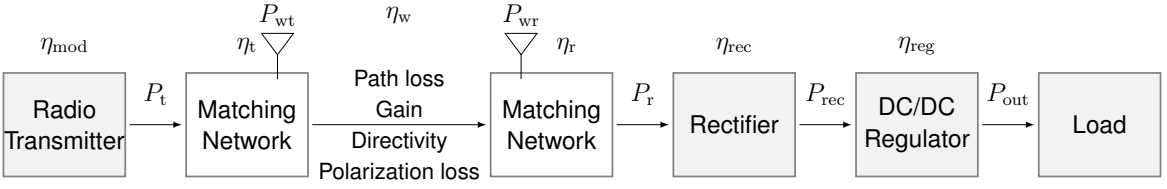

Figure 2.1: Transmission and efficiency model for RF power transfer.

In order to perform a power budget and performance analysis for an energy-constrained device in an RW environment, we first need to model the efficiency of the entire power transfer link. A general transmission and efficiency model for a wireless power transfer channel is depicted in Figure 2.1. It shows the main building blocks of both an RF transmitter and an energy harvesting device. An overview of the most prominent efficiencies and available models are covered in the following subsections.

2.1.1 DC-to-RF conversion efficiency η_{mod}

The first part of the WPT chain involves the generation and power amplification of the transmitted signal in the Radio Transmitter block. A power amplifier converts the low power, modulated RF signal from the signal generator into a signal with significant power.

The Radio Transmitter block takes a direct current (DC) supply as input and passes the modulated and amplified signal at its output terminals on to the matching network of a transmit antenna. Its efficiency η_{mod} is largely determined by the efficiency of the power amplifier. Various classes of power amplifiers are available, each having their own advantages and disadvantages. The evaluation and design of the hardware resources for RF WPT will be studied in the REINDEER deliverable D2.3 [41].

2.1.2 Matching efficiencies η_{t}, η_{r}

Impedance matching is crucial throughout the full power transfer link as it ensures maximum power transfer between each source and load component. However, two impedance matching blocks are included in particular since these apply to the RF chain and are therefore most complex: one between the radio transmitter and the transmit antenna, and the second between the receiver antenna and the rectifier. Maximum power transfer occurs when the output impedance of the source Z_{S} is equal to the complex conjugate input impedance of the load Z_{L}, i.e.,

$$Z_{\mathrm{L}} = Z_{\mathrm{S}}^{*}\,. \tag{2.1}$$

In the case of an impedance mismatch, power losses will occur. The impedance matching efficiency η can be expressed as

$$\eta = 1 - |\Gamma|^2 \tag{2.2}$$

where Γ is the reflection coefficient as a ratio of the complex amplitude of the reflected wave to that of the incident wave, and given as follows:

$$\Gamma = \frac{Z_{\mathrm{L}} - Z_{\mathrm{S}}^{*}}{Z_{\mathrm{L}} + Z_{\mathrm{S}}}. \tag{2.3}$$

Power amplifiers and rectifiers contain nonlinear elements such as diodes and transistors. Consequently, their impedance is highly dependent on the operating frequency, input power and load impedance, which makes impedance matching design challenging [46]. The situation becomes even more complicated when a large bandwidth is desired. A frequency shift impacts the impedance of the reactive components in the circuits, which in turn makes balancing tricky. Often the requirements become impractical as the frequency range increases. Moreover, no circuit component is ever perfect and hence parasitic components will cause energy losses.

2.1.3 RF-to-RF transmission efficiency η_{w}

The path between the transmit power P_{t}, incident to the transmit matching network, and the receive power P_{r}, available at the output of the receive matching network is essentially modeled

by the well-known Friis transmission equation[1]

$$\frac{P_\mathrm{r}}{P_\mathrm{t}} = \underbrace{\left(1-|\Gamma_\mathrm{t}|^2\right)}_{\text{TX matching } \eta_\mathrm{t}} \underbrace{\left(1-|\Gamma_\mathrm{r}|^2\right)}_{\text{RX matching } \eta_\mathrm{r}} \underbrace{\left(\frac{\lambda}{4\,\pi\,d}\right)^2 G_\mathrm{t}\,G_\mathrm{r}\ \overbrace{\left|\boldsymbol{\rho}_\mathrm{t}\cdot\boldsymbol{\rho}_\mathrm{r}\right|^2}^{\text{Polarization gain}}}_{\text{Path gain } \eta_\mathrm{w}} \tag{2.4}$$

in the case of free-space propagation of a single-input single-output (SISO) system model. Note that (2.4) only considers matching losses due to possible impedance mismatches between the matching networks and the connected antennas. Power losses due to lossy components are not included.

The path gain η_w defined in (2.4) models the free-space transmission efficiency, i.e., a ratio, in terms of *powers* between two antennas. Consequently, the way it is stated, it is valid for a SISO system. In its essence, it describes the power density caused at a distance d from the transmitting antenna with a gain G_t. The power density is impinging on a receiving antenna with a (maximum) effective aperture $A_\mathrm{r} = G_\mathrm{r}\,\frac{\lambda^2}{4\pi}$, which then describes the portion of power that is received by the receiving antenna (refer to Section 2.2.1 for a detailed description). Depending on the orientation of the polarization vectors $\boldsymbol{\rho}_\mathrm{t}$ and $\boldsymbol{\rho}_\mathrm{r}$ of the transmitting and receiving antennas, a polarization loss can occur. That is, the term $\left|\boldsymbol{\rho}_\mathrm{t}\cdot\boldsymbol{\rho}_\mathrm{r}\right|^2 \in [0,1]$ models a polarization gain[2] associated with a polarization mismatch (equivalent to the $\cos^2(\alpha)$ for an angle α between the polarization vectors). Since (2.4) is defined for powers, it holds no information about the phases at which power waves are impinging on the receiving antenna, i.e., the individual terms are real-valued.

To be able to use the Friis transmission equation for multiple-input single-output (MISO) systems capable of exploiting array gain, the equation needs to be transferred to the *amplitude* domain, i.e., using complex-valued terms that reflect the phases of impinging power wave amplitudes. In Section 2.2, we define a channel model based on the Friis transmission model and bistatic radar range equation for power wave amplitudes. Formulated through scattering parameters (S-parameters) for amplitudes, it sustains the superposition property of linear time-invariant (LTI) systems, which is essential for exploiting array gains. The model allows to simulate WPT in a physically correct manner. We show simulations of power transfer in Sections 3.2 and 4.1 and validate the model correctness through realistic vector network analyzer (VNA) measurements in Section 2.3.

2.1.4 RF-to-DC conversion efficiency η_rec

The collection of the receiver antenna, matching network and rectifier is better known as the rectenna. Its primary function is to convert RF power into DC power at the highest efficiency possible. In order to obtain the best overall efficiency, every block in the rectenna must be perfectly tuned with respect to the others.

The antenna is the collector of RF energy and converts the electromagnetic field into a voltage at a given impedance, i.e., power. The maximization of the antenna efficiency comes down to transfer as much of the incident RF power to its output as possible. Consequently, materials should be selected that minimize conduction and dielectric losses [7]. The subsequent matching network

[1] The Friis transmission equation is here for reference, the individual quantities are introduced in Sections 2.1.2 and 2.1.3.

[2] The term *gain* merely relates to the fact that $\left|\boldsymbol{\rho}_\mathrm{t}\cdot\boldsymbol{\rho}_\mathrm{r}\right|^2 \leq 1$ appears as a multiplicative factor in (2.4), contrary to a *loss* that would appear as a multiplicative inverse.

ensures a maximum power transfer from the antenna to the rectifier. The antenna efficiency η_{ant} can be calculated according to [7]

$$\eta_{\mathrm{ant}} = \frac{P_{\mathrm{r}}}{P_{\mathrm{wr}}} = \eta_{\mathrm{c}}\eta_{\mathrm{d}}(1 - |\Gamma_{\mathrm{ant}}|^2) \tag{2.5}$$

where η_{c} is the conduction efficiency, η_{d} is the dielectric efficiency and Γ_{ant} is the reflection coefficient as a result of the impedance mismatch.

The rectifier is the heart of the receiver device where the high-frequency signal is converted into DC power. The efficiency of this block is essential to the overall system efficiency. Often, a diode is considered for rectification. This not only makes rectifier design challenging, it also complicates the tuning of all other blocks as impedance becomes dependent on the operating frequency, input power and load. To maximize the RF-to-DC power conversion efficiency, one can initially optimize with respect to two key design parameters [31]: the input voltage at the rectifier and the threshold voltage of the diode. A large input voltage increases the ratio of output to input voltage, while a small threshold voltage increases the rectification voltage interval. A higher input voltage at the rectifier can be obtained through a high-Q resonator, yet has an inverse effect on the bandwidth of the system [31]. In addition, the threshold cannot be reduced endlessly as it is connected to the reverse breakdown voltage of the diode at semiconductor level [33]. This latter voltage determines the efficiency of the rectifier at higher input powers.

To date, Schottky diodes are often used for rectification since they have a low threshold voltage, low power consumption, low parasitic effects, and high switching speed [7]. Moreover, they are reliable and cheap [23]. Recently, there has been a shift towards complementary metal oxide semiconductor (CMOS) integrations. In CMOS technology, a diode can effectively be created through a diode-connected transistor, e.g., through connecting the gate and drain of an n-channel metal-oxide semiconductor (nMOS) transistor. The lower threshold voltage of CMOS provides a better sensititivty at low operating voltages compared to Schottky diodes. This lower threshold, however, comes with an increased leakage current, which means that certain design trade-offs need to be considered. Furthermore, CMOS is an interesting alternative because of its simple implementation, which entails a low cost and small form factor [48]. Next to Schottky diodes and CMOS, alternative types of diodes have been developed, such as tunnel and spin diodes, each having certain advantages and disadvantages [23].

There exist several rectifier topologies of which the half-wave, full-wave and bridge rectifier are the most common. However, a single rectifier might not be able to deliver a sufficiently high voltage for the device to operate. Hence, a voltage multiplier is often employed in rectifier design. It is a special type of rectifier circuit that not only converts the incoming AC voltage in a DC signal, but at the same time increases the output voltage through rectifier stacking [48]. This in turn affects the input impedance and consequently, the power conversion efficiency. Common configurations are the Dickson charge pump and Cockcroft-Walton multipliers [48].

A baseline model for the output power P_{rec} of a rectifier circuit in dependence of the input power P_{r} is presented in [1]:

$$P_{\mathrm{rec}} = f\left(P_{\mathrm{r}}\right) \tag{2.6}$$

where

$$f(x) \triangleq \begin{cases} 0 & x \in [0, P_{\text{in}}^{\text{sen}}], \\ e(x) \cdot x & x \in [P_{\text{in}}^{\text{sen}}, P_{\text{in}}^{\text{sat}}], \\ e(P_{\text{in}}^{\text{sat}}) \cdot P_{\text{in}}^{\text{sat}} & x \in [P_{\text{in}}^{\text{sat}}, \infty). \end{cases} \tag{2.7}$$

Function $e(\cdot)$ represents the harvesting efficiency for a given rectifier circuit as a function of the input power over the interval $[P_{\text{in}}^{\text{sen}}, P_{\text{in}}^{\text{sat}}]$. $P_{\text{in}}^{\text{sen}}$ and $P_{\text{in}}^{\text{sat}}$ respectively denote the rectifier *sensitivity* and *saturation* threshold of the rectifier circuit.

When P_{r} is smaller than $P_{\text{in}}^{\text{sen}}$, no power can be harvested at the output of the rectifier. Once this sensitivity threshold is exceeded, P_{rec} must be a monotonically increasing function of P_{r}. Ultimately, as P_{r} continues to increase, P_{rec} will reach a maximum as the rectifier gets saturated.

Several models have been proposed that allow to determine an explicit formula for $f(\cdot)$ given any rectifier circuit [2]. In general, these models assume a specific parametrization for $e(\cdot)$ such as a polynomial or sigmoid function and then apply parameter fitting based on measured efficiency data of the rectifier circuit.

2.1.5 DC-to-DC conversion efficiency η_{reg}

A DC-DC converter can be used to convert the output voltage of the rectifier to the desired supply voltage of the device. Since the rectifier's output voltage can also be tuned by means of a voltage multiplier rectifier topology, this block can actually be omitted. However, when the harvested power is stored in an energy buffer such as a capacitor or battery, the desired output voltage can vary in a much larger interval. For example, in the case of a lithium-ion cell, the voltage often ranges between $3.6\,\text{V}$ and $4.2\,\text{V}$, and for a capacitor even between $0\,\text{V}$ and the maximum operating voltage specified by the manufacturer. Consequently, a linear regulator or switched-mode power supply (e.g., buck converter) may need to be applied to down-convert the voltage level, where the efficiency depends on the used DC-DC converter class. In the case of a linear regulator, the efficiency can be modelled as:

$$\eta_{\text{DC-DC,linear}} = \frac{V_{\text{out}}}{V_{\text{in}}} \tag{2.8}$$

where V_{in} and V_{out} are respectively the input voltage to and output voltage of the linear DC-DC regulator.

2.2 Channel model

To compute a WPT power budget and conduct performance analyses for RW, the RF-to-RF transmission efficiency η_{w} has to be modeled through a MISO channel model. For that purpose, we employ the geometry-based channel model defined in [10]. It models the path between TX antennas and an RX antenna by means of the path gain, as indicated in the center of Figure 2.1, where an array gain due to a desired precoding method is taken into account.

For simplicity, lossless antennas are assumed where direction-dependent gain patterns are used and antenna polarizations are regarded by means of polarization vectors. We consider an RW panel centered at a position $\boldsymbol{p}_{\text{RW}} = [x_{\text{RW}}, y_{\text{RW}}, z_{\text{RW}}]^{\mathsf{T}}$ consisting of L_{t} antennas and transmitting power wirelessly to an EN device at position $\boldsymbol{p}_{\text{EN}} = [x_{\text{EN}}, y_{\text{EN}}, z_{\text{EN}}]^{\mathsf{T}}$. The ℓ^{th} array-element

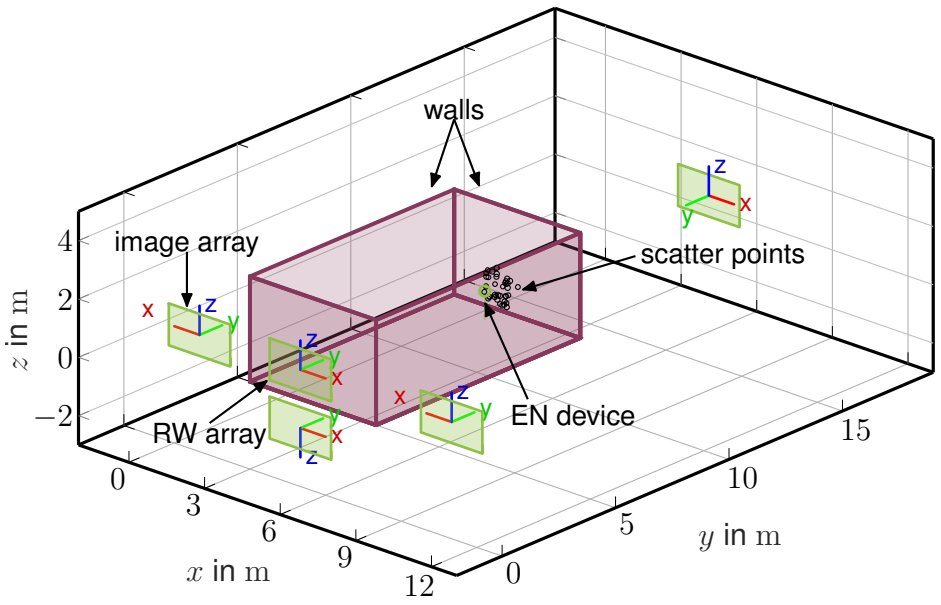

Figure 2.2: A possible scenario that can be represented with the channel model in Section 2.1.3 and has been simulated in [10]. The walls of a $(5\,\mathrm{m} \times 9\,\mathrm{m} \times 3.5\,\mathrm{m})$ large room are modeled by virtual mirror arrays. Scatter points are distributed in proximity of the EN device.

position is denoted as $\boldsymbol{p}_{\mathrm{RW}}^{(\ell)} = [x_{\mathrm{RW}}^{(\ell)}, y_{\mathrm{RW}}^{(\ell)}, z_{\mathrm{RW}}^{(\ell)}]^{\mathsf{T}}$. We employ a MISO channel model where the EN device receives a complex-valued baseband amplitude, i.e., a phasor,

$$y = \sum_{k=1}^{K} \boldsymbol{h}_k^{\mathsf{T}} \boldsymbol{s} + \sum_{k=1}^{K} \boldsymbol{h}_{\mathrm{sc},k}^{\mathsf{T}} \boldsymbol{s} + n \tag{2.9}$$

where $\boldsymbol{h}_k = [h_{k,1}, \ldots, h_{k,L_{\mathrm{t}}}]^{\mathsf{T}} \in \mathbb{C}^{L_{\mathrm{t}} \times 1}$ is the channel vector of the k^{th} specular multipath component (SMC), $\boldsymbol{h}_{\mathrm{sc},k}^{\mathsf{T}}$ the diffuse multipath (DM) channel vector of the k^{th} SMC, and $\boldsymbol{s} = [s_1, \ldots, s_{L_{\mathrm{t}}}]^{\mathsf{T}} \in \mathbb{C}^{L_{\mathrm{t}} \times 1}$ the transmit signal vector of the panel in complex baseband.

The first term in (2.9) models deterministic reflections as a sum of scalar products of the separate channel-vectors for K SMCs, including the line-of-sight (LoS). The second term models DM by means of point source scatterers. The third term $n \in \mathbb{C}$ denotes complex additive white Gaussian noise (AWGN) with variance σ_{n}^2. The following sections describe the models for SMCs and DM in detail, ultimately aiming to derive the RF-to-RF transmission efficiency

$$\eta_{\mathrm{w}} = \frac{|y|^2}{\|\boldsymbol{s}\|^2} \tag{2.10}$$

by means of these models.

2.2.1 Specular multipath

Deterministic SMCs are modeled according to an image-source model [32] based on a geometric environment model, allowing to compute the position $\boldsymbol{p}_{\mathrm{RW},k}$ of the image source representing the k^{th} SMC. The ℓ^{th} element of the channel vector $\boldsymbol{h}_k$ is thus modeled as

$$[\boldsymbol{h}_k]_\ell = \underbrace{\sqrt{G_{\mathrm{r}}} \frac{\lambda}{\sqrt{4\pi}}}_{\sqrt{A_{\mathrm{r}}}} \sqrt{G_{\mathrm{t}}} \frac{1}{\sqrt{4\pi} d_{k,\ell}} g_{\mathrm{SMC},k}\, g_{\mathrm{p},k,\ell}\, e^{-j\frac{2\pi}{\lambda} d_{k,\ell}} \tag{2.11}$$

where $d_{k,\ell} = \|\boldsymbol{p}_{\mathrm{EN}} - \boldsymbol{p}_{\mathrm{RW},k}^{(\ell)}\|$ is the distance between the transmit antenna $\ell \in \{1, \ldots, L_{\mathrm{t}}\}$ of the image source k and the EN device, the operator $\|\cdot\|$ denotes the vector norm and $[\,\cdot\,]_\ell$ denotes the ℓ^{th} vector element. G_{t} and G_{r} denote angle-dependent antenna gains[3] of transmit and receive antennas, while $g_{\mathrm{SMC,k}}$ and $g_{\mathrm{p},k,\ell}$ denote gain factors due to specular reflections and antenna polarizations, respectively.

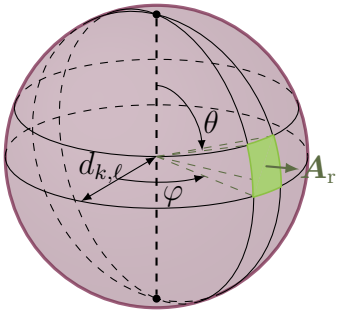

Figure 2.3: Schematic illustration of a sphere with radius $d_{k,\ell}$. The power transmitted by an antenna ℓ at its origin spreads over the spherical surface. The receiving aperture $\boldsymbol{A}_{\mathrm{r}}$ of the EN device collects a part of the transmitted power.

The channel model for specular multipath consists of six factors: The first (combined) factor in (2.11) models the square root of the aperture $A_{\mathrm{r}} = G_{\mathrm{r}} \frac{\lambda^2}{4\pi}$ of a receiving antenna. The third factor models the spread of power over the surface of a sphere with a radius $d_{k,\ell}$. The factor $g_{\mathrm{SMC},k} \in \mathbb{C}$ represents an amplitude gain and phase-shift associated with reflection k, while the term

$$g_{\mathrm{p},k,\ell} = \left|\boldsymbol{\rho}_{\mathrm{t},\ell}^{\mathsf{T}}\, \boldsymbol{R}_{k,\ell}\, \boldsymbol{\rho}_{\mathrm{r}}\right| \tag{2.12}$$

models a possible polarization loss due to a mismatch of the transmit and receive polarization vectors $\boldsymbol{\rho}_{\mathrm{t},\ell}$ and $\boldsymbol{\rho}_{\mathrm{r}}$ of the respective *linearly polarized* antennas. The rotation matrix $\boldsymbol{R}_{k,\ell}$ models a possible rotation of the polarization vector of a transmitted signal in the plane orthogonal to the direction of propagation, which incurs due to reflection k (see Appendix A.2 for a definition). Note that the polarization gain $g_{\mathrm{p},k,\ell} \in \mathbb{R}^{[0,1]}$ attains 1 in case of perfectly aligned polarization vectors and 0 in case of orthogonal polarization vectors. A combination of e.g. linearly polarized transmit antennas and a *circularly polarized* receive antenna will result in a polarization gain of $g_{\mathrm{p},k,\ell} = -3\,\mathrm{dB}$, regardless of the linear polarization orientation [21] (see Appendix A.1 for a derivation). Finally, the complex exponential term models the phase shift due to the distance $d_{k,\ell}$ traveled [4].

With the transmit signal vector $\boldsymbol{s}$ given as a vector of complex-valued power wave amplitudes in the dimension $\sqrt{\text{power}}$, (2.11) models the Friis transmission equation in (2.4) for power wave amplitudes[4]. That is, the received power P_{wr} and transmitted power P_{wt} follow the relation

$$\frac{P_{\mathrm{wr}}}{P_{\mathrm{wt}}} = \frac{|y|^2}{\|\boldsymbol{s}\|^2} = PG = \eta_{\mathrm{w}} \tag{2.13}$$

[3]The notation has been kept the same as in the Friis transmission equation, where the gains G are the maximum of the antenna gain patterns $G(\theta, \varphi)$, i.e., $G = \max\{G(\theta, \varphi)\}$. However, (2.11) is valid for using the gain patterns $G(\theta, \varphi)$ in dependence on the angles of incidence and departure, which vary for each transmit antenna ℓ and SMC k. For brevity, the angular dependency is omitted in the notation.

[4]In contrast to the actual Friis transmission equation in (2.4), which is formulated for powers, (2.13) is formulated for complex-valued power wave amplitudes. Thus, it sustains the *superposition* property of LTI systems, essential for applying any kind of beamforming.

where PG is the path gain, equivalent to the RF-to-RF transmission efficiency η_{w} for WPT. The entries $[\boldsymbol{h}_k]_\ell$ of the SMC channel vector are consequently unitless transmission coefficients, i.e., S-parameters.

2.2.2 Diffuse multipath

The second term of the channel model in (2.9) represents stochastic scattering at small, distributed objects, or surfaces that are rough with respect to the signal wavelength λ [29]. The DM is modeled by a number of M_{sc} point scatterers at positions $\boldsymbol{p}_{\mathrm{sc},m} = [x_{\mathrm{sc}}^{(m)}, y_{\mathrm{sc}}^{(m)}, z_{\mathrm{sc}}^{(m)}]^{\mathsf{T}},\ m \in \{1, \ldots, M_{\mathrm{sc}}\}$ where all impinging specular waves are rescattered, assuming only single-bounce scattering. The resulting channel vectors for each SMC k are defined as

$$\boldsymbol{h}_{\mathrm{sc},k}^{\mathsf{T}} = \boldsymbol{h}_{\mathrm{RX}}^{\mathsf{T}}\, \boldsymbol{\Sigma}_{\mathrm{sc}}\, \boldsymbol{H}_{\mathrm{TX},k} \tag{2.14}$$

where $\boldsymbol{H}_{\mathrm{TX},k} \in \mathbb{C}^{M_{\mathrm{sc}} \times L_{\mathrm{t}}}$ is the transmit scatter channel matrix from the k^{th} mirror array to the scatterers and $\boldsymbol{h}_{\mathrm{RX}} \in \mathbb{C}^{M_{\mathrm{sc}} \times 1}$ is the channel vector from the scatterers to the EN device. $\boldsymbol{\Sigma}_{\mathrm{sc}}$ is a diagonal matrix modeling the radar cross sections (RCSs) of all scatterers.

The diffuse multipath model consists of two parts: First, the transmission of a power wave from an antenna ℓ of SMC k to a scatterer m, located at a distance $d_{k,\ell,m}$ away from the antenna (schematically depicted in Figure 2.4). Second, the reradiation of power from a scatterer m to the EN device, located at a distance d_m (schematically depicted in Figure 2.5).

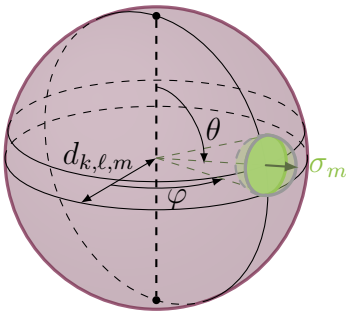

Figure 2.4: Schematic illustration of a sphere with radius $d_{k,\ell,m}$. The power of a wave transmitted by an antenna ℓ at its origin spreads over the spherical surface. At a distance $d_{k,\ell,m}$, it impinges on a scatterer m with RCS σ_m.

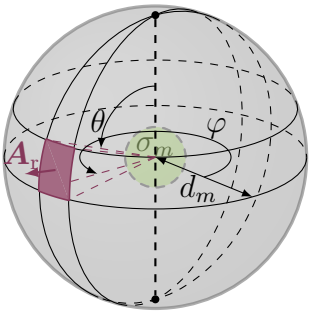

Figure 2.5: A scatterer m located at the origin of a sphere reradiates power isotropically. The reradiated power spreads over the surface of the sphere with radius d_m. At the distance d_m from the scatterer, it impinges on the receiving aperture $\boldsymbol{A}_{\mathrm{r}}$ of the EN device.

The entries of the scatter channel matrix

$$[\boldsymbol{H}_{\mathrm{TX},k}]_{\ell,m} = \sqrt{G_{\mathrm{t}}}\, \frac{1}{\sqrt{4\pi}\, d_{k,\ell,m}}\, g_{\mathrm{SMC},k}\, g_{\mathrm{p,sc}}\, e^{-j\frac{2\pi}{\lambda} d_{k,\ell,m}} \tag{2.15}$$

model the power density caused by an isotropic antenna ℓ at a distance $d_{k,\ell,m}$ (see Figure 2.4), where any incurring polarization losses are denoted as $g_{\mathrm{p,sc}}$ for brevity. At this distance, a transmitted power wave impinges on a scatterer m with a RCS σ_m. The matrix $\boldsymbol{\Sigma}_{\mathrm{sc}} = \mathrm{diag}\left\{[\sqrt{\sigma_1} e^{j\varphi_1}, \ldots, \sqrt{\sigma_{M_{\mathrm{sc}}}} e^{j\varphi_{M_{\mathrm{sc}}}}]\right\} \in \mathbb{C}^{M_{\mathrm{sc}} \times M_{\mathrm{sc}}}$ is a diagonal matrix containing the RCS σ_m of point source scatterer $m \in \{1, \ldots, M_{\mathrm{sc}}\}$ and an associated phase-shift φ_m on its main

diagonal. The product $\boldsymbol{\Sigma}_{\mathrm{sc}}\,\boldsymbol{H}_{\mathrm{TX},k}$ is a unitless S-parameter matrix. It models the transmission coefficients from every antenna ℓ of SMC k to every scatter point m.

The entries of the receive channel vector

$$[\boldsymbol{h}_{\mathrm{RX}}]_m = \underbrace{\sqrt{G_{\mathrm{r}}}\,\frac{\lambda}{\sqrt{4\pi}}}_{\sqrt{A_{\mathrm{r}}}}\,\frac{1}{\sqrt{4\pi}d_m}\,e^{-j\frac{2\pi}{\lambda}d_m} \tag{2.16}$$

model the power received by a receiving antenna at the location of the EN device from a scatterer m (see Figure 2.5). The distance between the scatterer m and the EN device is $d_m = \|\boldsymbol{p}_{\mathrm{sc},m} - \boldsymbol{p}_{\mathrm{EN}}\|$. The vector $\boldsymbol{h}_{\mathrm{RX}}$ is an S-parameter vector itself, holding the transmission coefficients from the scatterer to the EN device.

The channel vector in (2.14) effectively models the bistatic radar range equation for power wave amplitudes. The equation for the path gain (2.13) allows to model the WPT efficiency of a transmitting RW panel to a receiving EN device in a physically correct manner and is therefore used as a performance metric in the coming sections. Note that the path gain PG does not only depend on the environment-dependent channel vectors $\boldsymbol{h}_k$ and $\boldsymbol{h}_{\mathrm{sc},k}$, but also on the transmit signal vector

$$\boldsymbol{s} = \sqrt{P_{\mathrm{wt}}}\,\boldsymbol{w} \tag{2.17}$$

where $\boldsymbol{w}$ is a vector of chosen beamforming weights. An appropriate choice of beamforming weights can be made to serve a specific goal like the transmission of maximum power (e.g., through maximum ratio transmission (MRT)) to an EN device, or increasing the initial access distance (e.g., by exploiting beam diversity), as the REINDEER consortium has demonstrated [10].

2.3 Measured channel characteristics

We employ VNA measurements to verify the channel model defined in Section 2.2. Figure 2.6 shows the measurement scenario used to verify our model with one synthetic transmitting uniform linear array (ULA) spaced at $\frac{\lambda}{2}$ (at $f_{\mathrm{c}} \approx 3.8\,\mathrm{GHz}$) with $L_{\mathrm{t}} = 51$ antennas transmitting power to a hypothetical EN device with a single receiving antenna. A Rohde & Schwarz ZVA24 is connected to the transmit and receive antennas and used for two-port measurements. The VNA is calibrated using a through – open – short – match (TOSM) calibration kit to remove linear systematic errors introduced by cables and connectors leading to the antennas. This effectively shifts the reference planes of the measurement to the antenna ports. We used two cross exponentially tapered slot (XETS) antennas [8] both for the transmitting array and the receiving EN device. The antennas are linearly polarized ultrawideband (UWB) patch antennas that ideally radiate predominantly in the direction of the x-axis[5] in Figure 2.6. Our measurements conducted between $3\,\mathrm{GHz} \leq f \leq 10\,\mathrm{GHz}$ are evaluated at a frequency $f_{\mathrm{c}} = 3.79\,\mathrm{GHz}$. We characterized the antenna matching $S_{11} = \Gamma_{\mathrm{t}}$ of the transmit antenna and $S_{22} = \Gamma_{\mathrm{r}}$ of the receiving antenna to account for the matching efficiencies η_{t} and η_{r} as described in (2.2). Furthermore, an antenna characterization conducted in an anechoic chamber enables us to make use of the gain patterns $G_{\mathrm{t}}(\theta,\varphi)$ and $G_{\mathrm{r}}(\theta,\varphi)$. The polarization vectors of the antennas are well aligned such that polarization losses should be negligible and the backlobe of the transmitting antenna from the $\frac{\lambda}{2}$-ULA is removed using an absorber to avoid undesired reflections from the wall. We scan

[5] Each antenna has two dominant lobes in both the positive and negative direction along the x-axis. The lobe of transmitting antenna facing the wall is removed through an absorber.

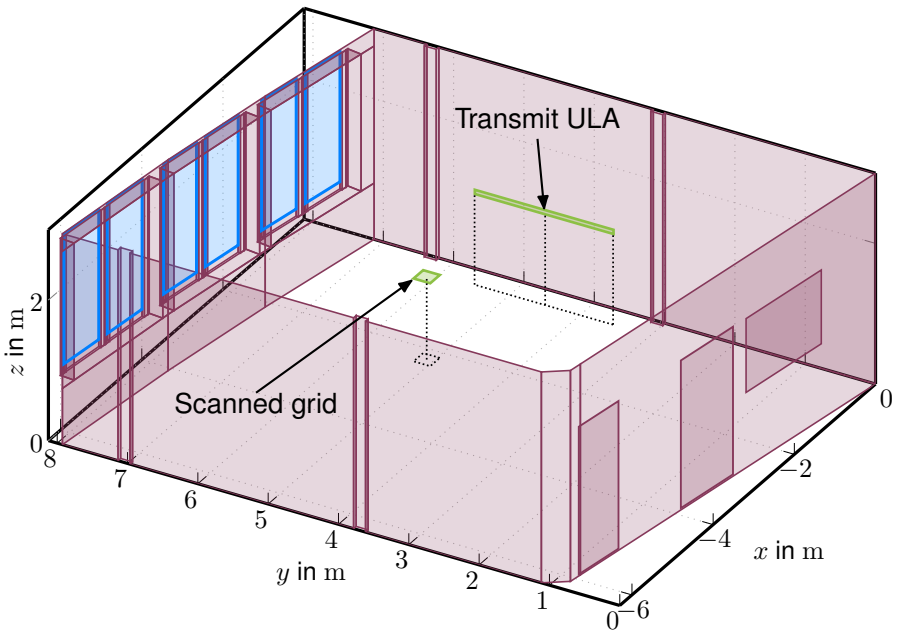

Figure 2.6: A three-dimensional (3D) floorplan (model) of the room in which the synthetic aperture (array) measurements have been conducted. The transmitting $\frac{\lambda}{2}$-ULA along the wall is indicated along with the measured grid in the horizontal plane that has been scanned in $\frac{\lambda}{4}$-spacing to visualize the PG distribution around the focal point (see Figure 2.7).

the region around the desired focal point (i.e., the EN device) on a $\frac{\lambda}{4}$-spaced grid to visualize the PG distribution in its vicinity using real-life measured data. Both the ULA along the wall and the scanned grid parallel to the xy-plane are synthetic apertures formed using two two-dimensional (2D) positioners. By subsequently measuring the channel between each transmitting antenna position and each receiving antenna position of the synthetic apertures, some idealizations are made that will not be present in real phased array: Parasitic mutual coupling in the antenna near fields of any adjacent antennas changes both their radiation patterns and the input impedances. This effect is not present in our idealized synthetic aperture measurements. However, Costa et al. who invented the XETS antenna measured the mutual coupling and evaluated the suitability of using the antennas in a multiple-input multiple-output (MIMO) configuration. In [8], they found that there is limited mutual coupling between adjacent XETS antennas and confirm their suitability for MIMO sytems.

In the following, we denote the *modeled* channel vector

$$\boldsymbol{h}_{\text{model}} = \sum_{k=1}^{K} \boldsymbol{h}_{k,\text{model}} \,. \tag{2.18}$$

The individual SMCs $\boldsymbol{h}_{k,\text{model}}$ are individually modeled according to (2.11) entirely from geometric environment information and are thus known.
The channel vector

$$\boldsymbol{h}_{\text{meas}} = \sum_{k=1}^{K} \boldsymbol{h}_{k,\text{meas}} \tag{2.19}$$

denotes the *measured* channel vector. That is, it is entirely measured and not modeled. The individual SMCs $\boldsymbol{h}_{k,\text{meas}}$ are unknown, as the sum in (2.19) is inherently present in the measurement

of $\boldsymbol{h}_{\mathrm{meas}}$ and a decomposition would have to be applied to extract $\boldsymbol{h}_{k,\mathrm{meas}}$. We use the VNA to measure the channel vector elements from each antenna ℓ to the receiving EN device using

$$[\boldsymbol{h}_{\mathrm{meas}}]_\ell = S_{21,\ell} \tag{2.20}$$

where $S_{21,\ell}$ is the complex-valued forward transmission coefficient from antenna ℓ to the receiving antenna[6]. Since our channel model defined in Section 2.2 models the channel vector $\boldsymbol{h}_{\mathrm{model}}$ as a unitless S-parameter vector of transmission coefficients, both the measured channel vector and the geometrically modeled channel vector are directly comparable. When applying MRT to the modeled channel vector, we yield a path gain (including matching losses) of

$$PG_{\mathrm{model}}\,\eta_{\mathrm{t}}\eta_{\mathrm{r}} = \eta_{\mathrm{w}}\,\eta_{\mathrm{t}}\eta_{\mathrm{r}} = \left|\boldsymbol{h}_{\mathrm{model}}^{\mathsf{T}}\,\boldsymbol{w}\right|^2\,\eta_{\mathrm{t}}\eta_{\mathrm{r}} \approx -28.40\,\mathrm{dB} \qquad \text{with} \qquad \boldsymbol{w} = \frac{\boldsymbol{h}_{\mathrm{model}}^{*}}{\|\boldsymbol{h}_{\mathrm{model}}\|} \tag{2.21}$$

at the known position of the EN device, assuming a free-space LoS environment[7]. Figure 2.7 (a) depicts a simulation result of the path gain distribution around the targeted focal point, where (for this initial analysis) free-space propagation is assumed and all walls have been removed from the environment.

Figure 2.7 (b) depicts the path gain distribution around the EN device, when applying MRT to the measured channel vector. A light standing wave pattern is caused by reflections at walls, floor and ceiling. When MRT is employed to focus power to a single point, the power in the point reaches an optimum. However, points in its vicinity may suffer from destructive interference caused by SMCs. At the desired location of the EN device, we yield a path gain (including matching losses) of

$$PG_{\mathrm{meas}}\,\eta_{\mathrm{t}}\eta_{\mathrm{r}} = \left|\boldsymbol{h}_{\mathrm{meas}}^{\mathsf{T}}\,\boldsymbol{w}\right|^2 \approx -27.49\,\mathrm{dB} \qquad \text{with} \qquad \boldsymbol{w} = \frac{\boldsymbol{h}_{\mathrm{meas}}^{*}}{\|\boldsymbol{h}_{\mathrm{meas}}\|} \tag{2.22}$$

where the slight improvement of $\Delta PG = PG_{\mathrm{meas}} - PG_{\mathrm{model}} \approx 1.23\,\mathrm{dB}$ results from the exploitation of SMCs in a simultaneous multibeam-transmission, e.g., via walls, the floor, and ceiling, to increase the path gain over what is achievable with an LoS-beam only. This exploitation of multipath propagation to increase the power budget is inherent to using MRT for computing the beamforming weights $\boldsymbol{w}$.

Simulating the path gain using a free-space model only, i.e., neglecting the presence of SMCs (other than the LoS), yields a path gain of $-28.40\,\mathrm{dB}$ in (2.21) and Figure 2.7 (a). Geometric environment information can also be used to *predict* channel vectors. This is of particular significance when it comes to the initial-access problem, i.e., waking up an EN device with unknown channel state information (CSI) and thus no measurement $\boldsymbol{h}_{\mathrm{meas}}$ available, as is discussed in Section 4.1.2. Employing an entirely *modeled* channel vector, predicted only using geometric environment information and under the assumption of free-space propagation (only using the LoS), applied on channel *measurements* yields

$$PG_{\mathrm{predict}}\,\eta_{\mathrm{t}}\eta_{\mathrm{r}} = \left|\boldsymbol{h}_{\mathrm{meas}}^{\mathsf{T}}\,\boldsymbol{w}_{\mathrm{model}}\right|^2 \approx -28.45\,\mathrm{dB} \qquad \text{with} \qquad \boldsymbol{w}_{\mathrm{model}} = \frac{\boldsymbol{h}_{\mathrm{model}}^{*}}{\|\boldsymbol{h}_{\mathrm{model}}\|}\,, \tag{2.23}$$

which comes close to the result of using entirely simulated data. Figure 2.7 (c) depicts the distribution of path gain around the hypothetical EN device position, where a standing wave pattern

[6] Since the reference planes of the measurement are located before the antennas, i.e., not removing errors introduced by the imperfect matching, these are inherently present in the measured channel vector.

[7] In this initial analysis, the presence of walls is neglected in the modeled path gain from (2.21) and (2.23), although their impact could be modeled if the gains g_{SMC} associated with reflections were known.

is originating from SMCs in contrast to true free-space propagation (compare Figure 2.7 (a)). If the exact locations of walls, the floor, and ceiling from the whole environment in Figure 2.6 were known along with the gains $g_{\mathrm{SMC},k}$ for each SMC k, a result as shown in Figure 2.7 (b) could be attained.

The significance of the measurements and simulations in Figure 2.7 and computations in (2.21), (2.22), and (2.23) is manifold: They demonstrate that we have derived a channel model that allows to model spherical wavefront beamforming for WPT in a physically correct manner, i.e., power waves are modeled correctly in terms of amplitude. Defining the channel model through unitless S-parameters allows to directly relate the model to the measurements conducted with a VNA. After its validation through the above measurements, the channel model can be used to spatially simulate path gains in chosen environment configurations in the upcoming sections. Furthermore, the result in Figure 2.7 (b) validates our assumption that multipath propagation can be exploited to improve the power budget, over using an LoS-beam only. We have shown that weight vectors for spherical wavefront beamforming can be predicted from geometric environment information. In this initial analysis, we have only presented results using the LoS. However, we will publish measurement results which show that SMCs from a more complex geometric environment can also be used to predict a channel vector, and thus model a weight vector, for a simultaneous multibeam transmission that is able to improve the power budget exploiting multipath propagation without measured CSI available.

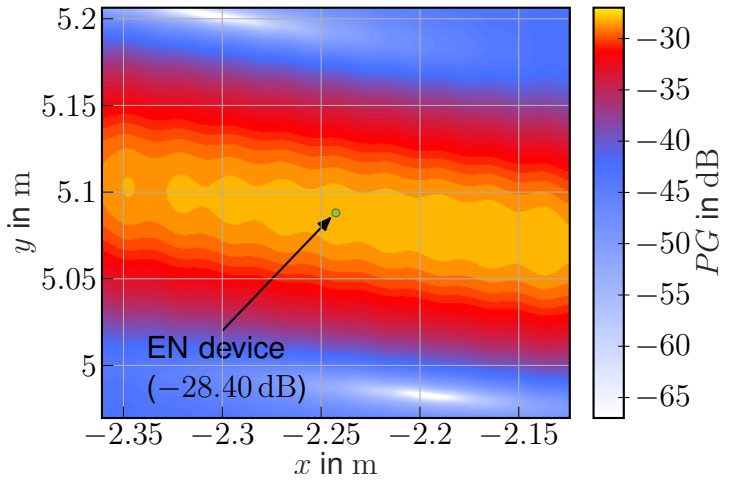

(a) Path gain PG computed from simulated (modeled) channel vectors $\boldsymbol{h}_{\mathrm{model}}$ at each grid point. Weights $\boldsymbol{w}$ computed from modeled CSI $\boldsymbol{h}_{\mathrm{model}}$ including only the LoS.

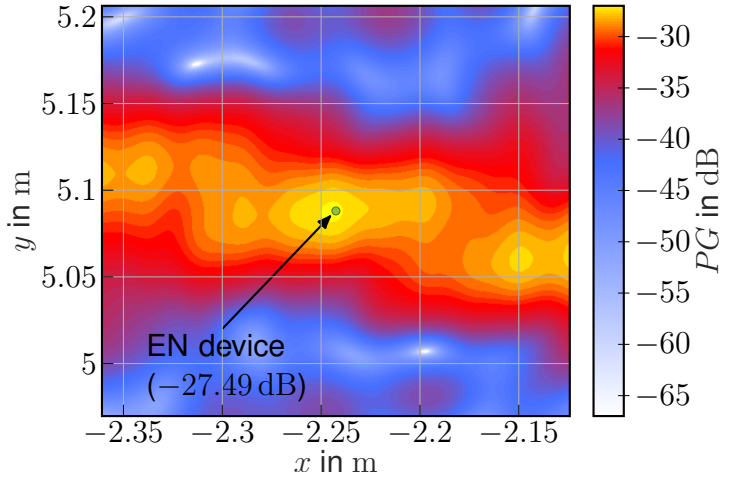

(b) Path gain PG computed from measured channel vectors $\boldsymbol{h}_{\mathrm{meas}}$ at each grid point. Weights $\boldsymbol{w}$ computed from full measured CSI $\boldsymbol{h}_{\mathrm{meas}}$ (inlcuding all SMCs).

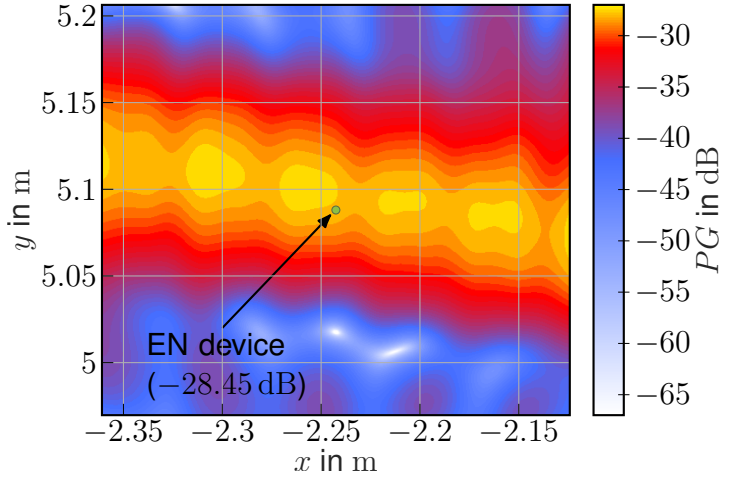

(c) Path gain PG computed from measured channel vectors $\boldsymbol{h}_{\mathrm{meas}}$ at each grid point. Weights $\boldsymbol{w}$ computed from modeled CSI $\boldsymbol{h}_{\mathrm{model}}$, where only the LoS is used.

Figure 2.7: PG measurements (including matching losses $\eta_{\mathrm{t}}\eta_{\mathrm{r}}$): MRT beamforming weights $\boldsymbol{w}$ applied to modeled/measured channel vectors at the EN device location. The 13×13 grid of measured points spaced at $\frac{\lambda}{4}$ in parallel to the xy-plane has been interpolated to increase the resolution of the visualized distribution.

Chapter 3

Regulatory compliance

In RF WPT systems, regulatory compliance plays a central role since the involved power demands are usually high and regulatory limits need to be adhered to. These limits need to be studied to make a RW infrastructure regulatory compliant and based on them, regulatory-compliant performance bounds can be derived. This chapter is divided into two sections: First, existing regulations applicable to RW are examined. Second, the potential of RW in the context of WPT is discussed with respect to radiation exposure. This is done by comparing physically large arrays with physically small arrays.

In Section 3.1, applicable regulatory standards are investigated with respect to a RW deployment for WPT. The maximum transmittable power, i.e., power budget, in accordance with regulatory standards is analyzed later in Section 4.1.1. We make connections to our channel model in Section 2.2 that allow us to relate regulated quantities to our simulation framework.
In Section 3.2, we analyze the spatial distribution of power density where we compare a *physically large array* and *physically small array*. The REINDEER consortium envisions the use of sub-$10\,\mathrm{GHz}$ frequencies. The corresponding relatively large wavelengths λ allow to form physically large apertures with antennas spaced at Nyquist rate[1]. An aperture being physically large or *distributed* and EN devices well located in the array near field results in power constructively interfering in a focal point rather than a beam, which in turn yields in a high receivable power within the focal point and a low radiation exposure everywhere else[2].
However, using higher frequencies up to the mmWave range results in physically small, i.e., *concentrated*, arrays where power is focused in a beam rather than a focal point. The unfavorable fact that the power density of concentrated arrays increases in proximity of the array makes them less suitable for WPT, especially with respect to human exposure restrictions.
Throughout this chapter, quantities denoted in bold, e.g., $\boldsymbol{A}$, are vector quantities, while their equivalent scalar magnitudes are denoted non-bold, e.g., A.

3.1 Applicable regulations

3.1.1 Regulation of EIRP

There are multiple regulatory standards limiting the equivalent isotropically radiated power (EIRP) for sub-$10\,\mathrm{GHz}$ frequencies. We list the EIRP limits for industrial, scientific and medical (ISM)

[1] The distance $\Delta_{i,j}$ between the two closest neighboring antennas ℓ_i and ℓ_j within a panel is at most $\Delta_{i,j} \leq \frac{\lambda}{2}$.
[2] This substantial fact is demonstrated in Figure 3.1, later in this section.

Table 3.1: Excerpt of harmonised frequency bands and technical parameters for short-range devices (SRDs) defined in the annex of European Commission (EC) recommendation 2006/771/EC [16] amended by commission implementing decision (EU) 2022/180. D denotes a possible duty cycle.

Band no	Frequency band	SRD category	Transmit power limit	Additional parameters
47a	$865\,\mathrm{MHz}$ - $868\,\mathrm{MHz}$	RFID	$2\,\mathrm{W}$ ERP	$B \leq 200\,\mathrm{kHz}$
47b	$865\,\mathrm{MHz}$ - $868\,\mathrm{MHz}$	Non-specific	$500\,\mathrm{mW}$ ERP	$B \leq 200\,\mathrm{kHz}$, $D \leq 10\,\%$
57a	$2400\,\mathrm{MHz}$ - $2483.5\,\mathrm{MHz}$	Non-specific	$10\,\mathrm{mW}$ EIRP	
57c	$2400\,\mathrm{MHz}$ - $2483.5\,\mathrm{MHz}$	Wideband devices	$100\,\mathrm{mW}$ EIRP	Frequency hopping
58	$2446\,\mathrm{MHz}$ - $2454\,\mathrm{MHz}$	RFID	$500\,\mathrm{mW}$ EIRP	Interference mitigation
61	$5725\,\mathrm{MHz}$ - $5875\,\mathrm{MHz}$	Non-specific	$25\,\mathrm{mW}$ EIRP	
62	$5795\,\mathrm{MHz}$ - $5815\,\mathrm{MHz}$	Transport/traffic	$2\,\mathrm{W}$ EIRP	Road tolling only

bands at $868\,\mathrm{MHz}$ in Table 3.2, at $2.4\,\mathrm{GHz}$ in Table 3.3, and at $5\,\mathrm{GHz}$ in Table 3.4 according to the respective European Telecommunications Standards Institute (ETSI) standards. It must be noted, however, that ETSI is a standardization organization and thus their standards are voluntary [45] in contrast to binding *regulations*, *directives*, and *decisions* passed by the EC. Table 3.1 shows an excerpt of the frequency allocation table defined in the annex of EC decision 2006/771/EC [16]. It specifies compliance limits for short-range devices (SRDs) in the frequency range between $9\,\mathrm{kHz}$ and $246\,\mathrm{GHz}$.

Decision 2006/771/EC is a binding act and thus compliance with the EIRP limits defined in Table 3.1 is compulsory. We found that distributed radio infrastructures have several beneficial effects regarding regulatory compliance. The compliance of RadioWeaves with EIRP limits is investigated in Section 3.2.2.

Table 3.2: Overview of regulatory standards for the $868\,\mathrm{MHz}$ and $915\,\mathrm{MHz}$ bands.

Band No. EC decision 2017/1483/EU [17]	Start freq. (MHz)	Stop freq. (MHz)	Band-width (MHz)	Device category	Max. e.r.p. (mW)	Duty cycle	Additional restrictions	Relevant ETSI standard
46a	863	865	2	Non-specific short-range devices	25	Polite access, or $\leq 0.1\,\%$		EN 300 220-2
46b	863	865	2	High duty cycle/ continuous transmission devices	10	No restriction	Wireless audio and multimedia streaming devices only.	
84	863	868	5	Wideband data transmission devices	25	Polite access, and $\leq 10\,\%$ for network access points $\leq 2.8\,\%$ otherwise	Wideband SRDs in data networks only.	
47	865	868	3	Non-specific short-range devices	25	Polite access, or $\leq 1\,\%$	Analogue audio applications other than voice are excluded. Analogue video applications are excluded.	EN 300 220-2
47a	865	868	3	Radio Frequency Identification (RFID) devices	2000	Polite access only		EN 302 208
47b	865	868	3	Non-specific short-range devices	500, APC or comparable	Polite access, and $\leq 10\,\%$ for network access points $\leq 2.5\,\%$ otherwise	Data networks only.	
48	868	868.6	0.6	Non-specific short-range devices	25	Polite access, or $\leq 1\,\%$	Analogue video applications are excluded.	EN 300 220-2
49	868.6	868.7	0.1	Low duty cycle/ high reliability devices	10	$1\,\%$	Alarm systems only.	EN 300 220-3
50	868.7	869.2	0.5	Non-specific short-range devices	25	Polite access, or $\leq 0.1\,\%$	Analogue video applications are excluded.	EN 300 220-2
51	869.2	869.25	0.05	Low duty cycle/ high reliability devices	10	$0.1\,\%$	Social alarm systems only.	
52	869.25	869.3	0.05	Low duty cycle/ high reliability devices	10	$0.1\,\%$	Alarm systems only.	EN 300 220-3
53	869.3	869.4	0.1	Low duty cycle/ high reliability devices	10	$1\,\%$	Alarm systems only.	EN 300 220-3
54	869.4	869.65	0.25	Non-specific short-range devices	500	Polite access, or $\leq 10\,\%$	Analogue video applications are excluded.	EN 300 220-2
55	869.65	869.7	0.05	Low duty cycle/ high reliability devices	25	$10\,\%$	Alarm systems only.	EN 300 220-3
56a	869.7	870	0.3	Non-specific short-range devices	5	No restriction	Audio and video applications are excluded. Voice applications allowed with advanced mitigation techniques.	EN 300 220-2
56b	869.7	870	0.3	Non-specific short-range devices	25	Polite access, or $\leq 1\,\%$	Analogue audio applications other than voice are excluded. Analogue video applications are excluded.	EN 300 220-2
Band No. EC decision 2018/1538/EU [18]								
1	874	874.4	0.4	Non-specific short-range devices	500, APC or comparable	Polite access, and $\leq 10\,\%$ for network access points $\leq 2.5\,\%$ otherwise	Only available for data networks. All devices within the data network shall be under the control of network access points.	
2	917.4	919.4	2	Wideband data transmission devices	25	Polite access, and $\leq 10\,\%$ for network access points $\leq 2.8\,\%$ otherwise	Only available for wideband short-range devices in data networks. All devices within the data network shall be under the control of network access points.	
3	916.1	918.9	2.8	Radio Frequency Identification (RFID) devices	4000	Polite access only		EN 302 208
4	917.3	918.9	1.6	Non-specific short-range devices	500, APC or comparable	Polite access, and $\leq 10\,\%$ for network access points $\leq 2.5\,\%$ otherwise	Only available for data networks. All devices within the data network shall be under the control of network access points.	
5	917.4	919.4	2	Non-specific short-range devices	25	Polite access and $\leq 1\,\%$	Only available for short-range devices in data networks. All devices within the data network shall be under the control of network access points.	

Table 3.3: Overview of regulatory standards for the $2.4\,\mathrm{GHz}$ ISM band.

Band No. EC decision 2017/1483/EU [17]	Start freq. (MHz)	Stop freq. (MHz)	Band-width (MHz)	Device category	Max. e.i.r.p. (mW)	Duty cycle	Additional restrictions	Relevant ETSI Standard
57a	2400	2483.5	83.5	Non-specific short-range devices	10	No restriction		EN 300 440
57b	2400	2483.5	83.5	Radio determination devices	25	No restriction		EN 300 440
57c	2400	2483.5	83.5	Wideband data transmission devices	100	Polite access	Max. e.i.r.p. density: $100\,\mathrm{mW}/100\,\mathrm{kHz}$ for frequency hopping modulation $10\,\mathrm{mW}/\mathrm{MHz}$ for other modulation types	EN 300 328
58	2446	2454	8	Radio Frequency Identification (RFID) devices	500	Polite access		EN 300 440
	2446	2454	8	Radio Frequency Identification (RFID) devices	4000	Polite acces, or $\leq 15\,\%$ over any $200\,\mathrm{ms}$	In-building only FHSS only	EN 300 440

Table 3.4: Overview of regulatory standards for the $5\,\mathrm{GHz}$ ISM band.

EC decision	Start freq. (MHz)	Stop freq. (MHz)	Band-width (MHz)	Device category	Max e.i.r.p. (mW)	Duty cycle	Additional restrictions	Relevant ETSI Standard
2022/179/EU [20]	5150	5250	100	Wireless Access Systems (WAS)/ Radio Local Area Networks (RLANs)	200	Polite access	Indoor, limited outdoor use, max. mean e.i.r.p. density $10\,\mathrm{mW}/\mathrm{MHz}$ in any $1\,\mathrm{MHz}$	EN 301 893
2022/179/EU [20]	5250	5350	100	Wireless Access Systems (WAS)/ Radio Local Area Networks (RLANs)	200	Polite access	Indoor only, max. mean e.i.r.p. density $10\,\mathrm{mW}/\mathrm{MHz}$ in any $1\,\mathrm{MHz}$	EN 301 893
2022/179/EU [20]	5470	5725	255	Wireless Access Systems (WAS)/ Radio Local Area Networks (RLANs)	1000	Polite access	Max. mean e.i.r.p. density $50\,\mathrm{mW}/\mathrm{MHz}$ in any $1\,\mathrm{MHz}$	EN 301 893
2017/1483/EC [17]	5725	5875	150	Non-specific short-range devices	25	No restriction		EN 300 440
-	5725	5875	150	Wireless Industrial Applications (WIA)	400	Polite access		EN 303 258

3.1.2 Regulation of power density

Human body exposure to electromagnetic fields between $0\,\mathrm{Hz}$ and $300\,\mathrm{GHz}$ is limited through the European Council recommendation 1999/519/EC [15], which is harmonized in EN IEC 62311 [19]. Its dosimetric/exposimetric limits are given in Annex II and Annex III, where the former describes the *basic restrictions*, summarized in Table 3.5. The latter describes the *reference levels*, summarized in Table 3.6.

Basic restrictions

For the sub-$10\,\mathrm{GHz}$ frequencies at which RW are operating, the human exposure limits of the basic restrictions are given in terms of the specific absorption rate (SAR) (see Table 3.5). The analysis of SAR for complex body geometries (e.g., complete modeling of a human head) is analytically intractable even for plain wave exposure. The SAR depends on the shape and orientation of the head and varies strongly with the frequency [30]. However, computing the plane wave power density is analytically tractable.

Reference levels

For sub-$10\,\mathrm{GHz}$ frequencies the human exposure limits of the reference levels are given in terms of the plane wave power density for most frequencies targeted by REINDEER (see Table 3.6). Annex III of 1999/519/EC states: *"Respect of all recommended reference levels will ensure respect of basic restrictions."* Therefore we analyze the spatial power density distribution of a RW deployment for WPT, keeping in mind that the *localized* basic restrictions (Table 3.5) regarding SAR still have to be adhered to.

Power density related to path gain

Before computing regulated quantities for a specific application scenario, it is worth pointing out that there is a close relation between the power density, and the path gain introduced in Section 2.1.3. For a receiving aperture $\boldsymbol{A}_\mathrm{r} = A_\mathrm{r}\,\boldsymbol{n}$ located in a plane perpendicular to the direction $\boldsymbol{e}_S$ of maximum radiation, the power density S and the path gain PG are related through

$$P_\mathrm{r} = \int_{A_\mathrm{r}} \boldsymbol{S}\cdot d\boldsymbol{A} = \underbrace{\frac{P_\mathrm{t}\,G_\mathrm{t}}{4\,\pi\,r^2}}_{S} A_\mathrm{r} = P_\mathrm{t}\,\underbrace{\frac{G_\mathrm{t}\,A_\mathrm{r}}{4\,\pi\,r^2}}_{PG} \tag{3.1}$$

where $\boldsymbol{S} = S\,\boldsymbol{e}_S$ is the Poynting vector and $\boldsymbol{n}$ is a unit vector perpendicular to the receiving aperture A_r. There is a linear relationship between the power density and the path gain, as seen

Table 3.5: Excerpt of basic restrictions defined in European Council recommendation 1999/519/EC [15] and harmonized in EN IEC 62311 [19] for frequencies of $10\,\mathrm{MHz}$ and above. The basic restrictions limit the SAR within the frequency range envisioned by the Reindeer consortium.

Frequency range	Whole body SAR	Localized SAR (head / trunk)	Localized SAR (limbs)	Power density
$10\,\mathrm{MHz}$ - $10\,\mathrm{GHz}$	$0.08\,\mathrm{W/kg}$	$2\,\mathrm{W/kg}$	$4\,\mathrm{W/kg}$	-
$10\,\mathrm{GHz}$ - $300\,\mathrm{GHz}$	-	-	-	$10\,\mathrm{W/m^2}$

Table 3.6: Excerpt of reference levels defined in European Council recommendation 1999/519/EC [15] and harmonized in EN IEC 62311 [19] for frequencies of $4\,\mathrm{MHz}$ and above. The reference levels (contrary to the basic restrictions) limit the equivalent plane wave power density rather than the SAR.

Frequency range f	**Equivalent plane wave power density**
$400\,\mathrm{MHz}$ - $2000\,\mathrm{MHz}$	$f^{\dagger}/200\,\mathrm{W/m^2}$
$2\,\mathrm{GHz}$ - $300\,\mathrm{GHz}$	$10\,\mathrm{W/m^2}$

† The symbol f is used to denote the (unitless) value of the frequency given in the left column, identically as stated in the original document [15].

from (3.1). This fact can be exploited as we introduced a model for the path gain in Section 2.1.3 which allows to compute a spatial distribution of the path gain for a specified environment scenario and chosen precoding method. Due to the linear relationship, a simulation of the path gain allows to evaluate the radiation safety in terms of the spatial distribution of power density.

3.2 Regulatory compliance of RadioWeaves

The regulatory limit of $S_{\max} = 10\,\mathrm{W/m^2}$ may be regarded as an upper bound for the spatial distribution of power density for a radio infrastructure unaware of human beings in its surroundings[3]. Traditionally, regulatory standards also limit the maximum permissible EIRP, which is a measure of the maximum power that an antenna radiates in any direction experienced in the far field. Equivalently, it is a measure of the maximum power density the antenna causes at a distance r. Conventionally, in SISO systems or *physically small* array MISO systems, using a more directive transmit antenna, or high array gain, respectively, demands to transmit at lower powers P_{t} in order to satisfy EIRP regulations. In this section, we demonstrate that *physically large* array MISO systems change this paradigm, as near field beam focussing can yield a high array gain in the near field and a low array gain in the far field. We show that a RW infrastructure is capable of transmitting at higher powers while causing both a lower EIRP and a lower maximum power density.

From the Friis equation in (2.4), the EIRP can be found by rearranging the transmitted power P_{t}:

$$P_{\mathrm{r}} = \underbrace{\left(1-|\Gamma_{\mathrm{t}}|^2\right)}_{\text{TX matching}} \underbrace{\left(1-|\Gamma_{\mathrm{r}}|^2\right)}_{\text{RX matching}} \left(\frac{\lambda}{4\,\pi\,d}\right)^2 \underbrace{P_{\mathrm{t}}\,G_{\mathrm{t}}}_{\text{EIRP}}\, G_{\mathrm{r}}\, \underbrace{\left|\boldsymbol{\rho}_{\mathrm{t}}\cdot\boldsymbol{\rho}_{\mathrm{r}}\right|^2}_{\text{Polarization loss}} \tag{3.2}$$

In a SISO system, the EIRP is defined as the product of transmit antenna gain G_{t} and transmitted power P_{t}. That is, having a more directive transmit antenna, i.e., a high antenna gain, the transmitted power has to be reduced in order to yield the same EIRP. For flexible RW panels that exhibit a good power budget in arbitrary directions, we suggest using antennas that ideally radiate uniformly into the half-space facing the inside of the room.

[3]Human body detection and tracking may allow for higher powers if human exposure safety can be ensured. However, awareness of human beings is disregarded throughout this document.

3.2.1 Compliance with power density limits

In addition to human exposure regulations, the maximum permissible EIRP limits the *power density*, i.e., power per unit area, in the direction of maximum radiation[4]. The Poynting vector $\boldsymbol{S}$ is a power density [4], that can be used to express the total received power P that is flowing into a volume V by integrating the power density over its *closed* boundary surface A:

$$P = \oint_{A=\partial V} \boldsymbol{S} \cdot d\boldsymbol{A} \qquad (3.3)$$

$$:= \int_{A_\mathrm{r}} \boldsymbol{S} \cdot d\boldsymbol{A} \qquad (3.4)$$

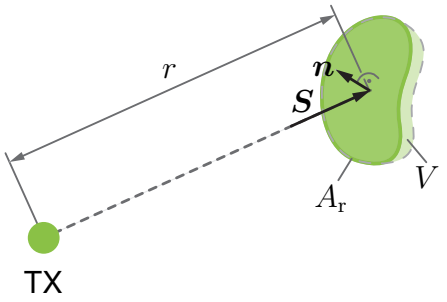

If the incident power is absorbed completely by the volume, only a portion A_r of the entire surface area contributes to the reception of power, i.e, to the integral in (3.3). That portion of its surface area at which the power flux enters the volume may be regarded as a receiving aperture A_r and may not necessarily be closed. The power density[5] at a given distance r from a transmitting antenna is limited by the EIRP through [21, 37]

$$S = \frac{dP_\mathrm{t}}{dA} = \frac{\mathrm{EIRP}}{4\,\pi\,r^2} = \frac{P_\mathrm{t}\,G_\mathrm{t}}{4\,\pi\,r^2}\,. \qquad (3.5)$$

Having a *physically small* antenna array, its maximum effective free-space array gain could linearly increase with the number of antennas L_t if being looked at from the array far field. If the EIRP is limited by regulations, the transmit power P_t must be decreased by a factor of L_t to yield the same power density S at a distance r from the array.

However, having a *physically large* antenna array and focusing power in the array near field, i.e., radiating converging spherical wave fronts rather than planar ones, the array gain pattern G becomes dependent on the range, i.e., $G = f(r, \theta, \varphi)$, and is no longer a function of the direction angles[6] only. The power density S that regulatory standards are limiting is therefore only existing at the focal point, which is ideally at the position of the EN device $G_\mathrm{array} = \max\{G(r, \theta, \varphi)\} = G(\boldsymbol{p}_\mathrm{EN})$. For ranges $r < d$, i.e. at distances r closer to the array than the distance d of the EN device, the array gain pattern $G(r, \theta, \varphi)$ is less than or equal to $G(\boldsymbol{p}_\mathrm{EN})$. That way, the power density can get smaller as one approaches the array (r decreasing), although the power density is inversely proportional to r^2 as is evident from (3.5).

Furthermore, for ranges $r > d$, the array gain pattern decreases as well with respect to $\boldsymbol{p}_\mathrm{EN}$, such that the EIRP of a *physically large* array evaluated at the array far field can be much lower than the EIRP of an equivalent *physically small* array. This fact is analyzed in Section 3.2.2 and visualized in Figure 3.3.

[4]The direction of maximum radiation is the direction (θ, φ) in spherical coordinates, where the near field antenna gain pattern exhibits its maximum $\max\{G(\theta, \varphi)\} = G_\mathrm{t}$.

[5]Evaluated at an infinitesimal area $d\boldsymbol{A}$ with a normal vector $\boldsymbol{n}$ oriented in parallel to the direction of maximum radiation, i.e., $\boldsymbol{S} \cdot d\boldsymbol{A} = \boldsymbol{S} \cdot \boldsymbol{n}\, dA = S\, dA$.

[6]In the antenna far field, assuming planar waves, $G(r_i, \theta, \varphi) \approx G(\infty, \theta, \varphi)\, \forall\, r_i > d_\mathrm{F}$, where d_F is the Fraunhofer distance (or Rayleigh distance) [34].

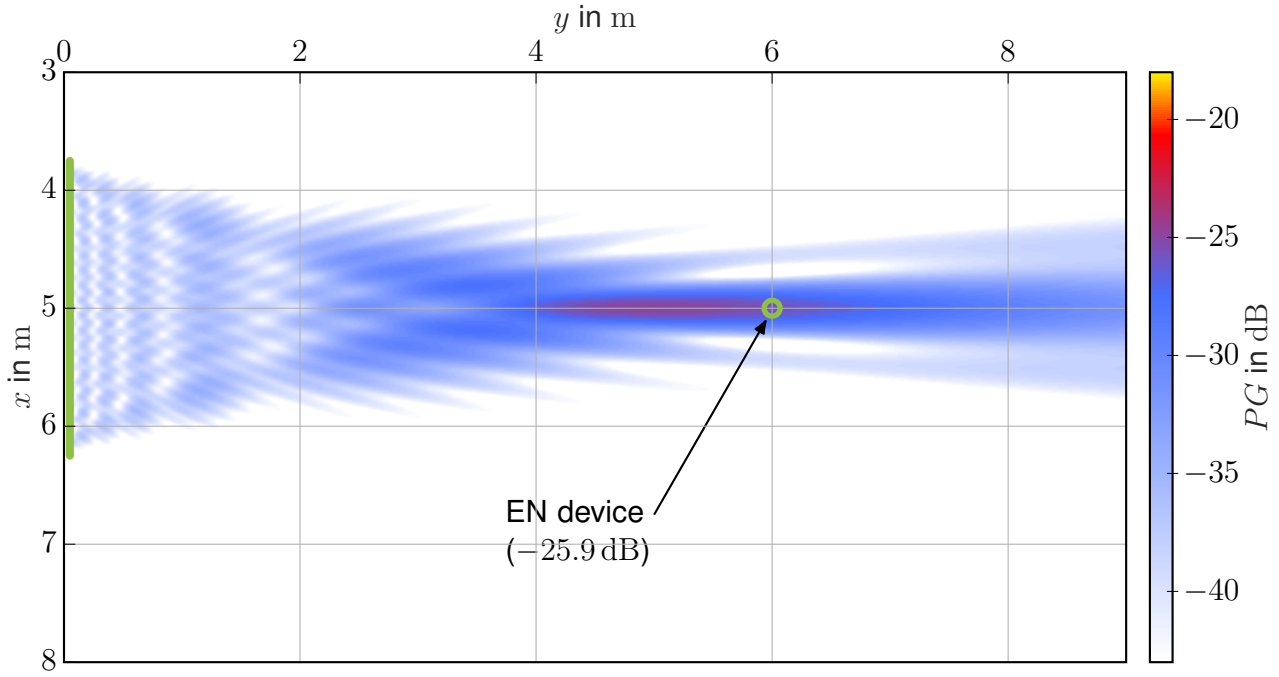

Figure 3.1: Free space MISO path gain PG for a physically large (or distributed) array evaluated on a cutting plane (at $z = 1\,\mathrm{m}$, perpendicular to the center of the array). The $\frac{\lambda}{2}$-URA is of size $(2.5\,\mathrm{m} \times 1.5\,\mathrm{m})$ and operates at $f_\mathrm{c} = 2.4\,\mathrm{GHz}$.

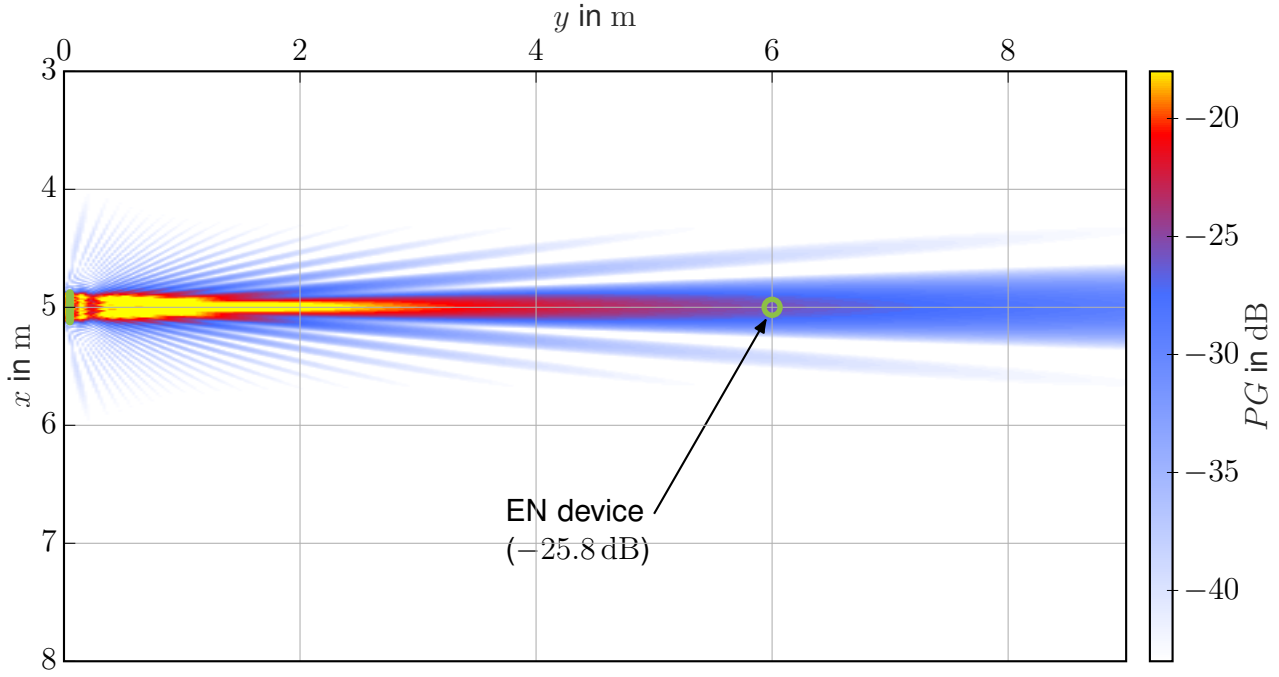

Figure 3.2: Free space MISO path gain PG for a physically small (concentrated) array. A scaling factor of 10 has been used for demonstration such that the $\frac{\lambda}{2}$-URA is of size $(0.25\,\mathrm{m} \times 0.15\,\mathrm{m})$, operating at $\tilde{f}_\mathrm{c} = 24\,\mathrm{GHz}$. The receiving (EN device) aperture is kept the same size as in Figure 3.1. Note that the colorbar is saturated at values lower than the actual maxima, i.e., does not correctly reflect peak powers, for illustration purposes.

To demonstrate these facts, we simulate the free-space path gain, linearly proportional to the power density, of a $(2.5\,\mathrm{m} \times 1.5\,\mathrm{m})$ uniform rectangular array (URA), with MRT chosen as a precoding method to reflect an optimal case[7]. The resulting power budget in Figure 3.1 demonstrates how transmitted power of a *physically large* antenna array is spatially distributed. In this simulation, we assume isotropic transmit and receive antennas and no polarization losses or parasitic coupling. There are no walls (no SMCs) and no scatter points present in the environment such that it corresponds closely to the simplified back-of-the-envelope calculations made in the REINDEER deliverable[8] D2.1 [11]. The computed MISO path gain PG at the EN device location $\boldsymbol{p}_{\mathrm{EN}}$ yields $-25.9\,\mathrm{dB}$.
Contrary to that, we simulate a *physically small* array with the same layout but scaled by a factor of $1/10$. Thus, we have scaled the physical aperture to $(0.25\,\mathrm{m} \times 0.15\,\mathrm{m})$ while increasing the frequency to $\tilde{f}_{\mathrm{c}} = 24\,\mathrm{GHz}$. That way, we also end up with a $\frac{\lambda}{2}$-URA again. Note that we kept the number of antennas the same in both simulations, thus we have different physical sizes but the same *electrical size*, i.e., equal array sizes in terms of wavelengths, for both arrays. For the sake of fairness, we kept the receiving aperture at the same physical size as in the physically large array simulation (from Figure 3.1). That is, we simulated the Friis transmission equation in the form

$$P_{\mathrm{r}} = \int_{A_{\mathrm{r}}} \boldsymbol{S} \cdot d\boldsymbol{A} = \frac{P_{\mathrm{t}}\, G_{\mathrm{t}}}{4\,\pi\, r^2} A_{\mathrm{r}}\,, \tag{3.6}$$

where the gain of the transmitting antennas $G_{\mathrm{t}} = 1$ and

$$A_{\mathrm{r}} = G_{\mathrm{r}}\, \frac{\lambda^2}{4\,\pi} = 1\, \frac{c^2}{4\,\pi\,(2.4\,\mathrm{GHz})^2} \tag{3.7}$$

is the effective aperture[9] of the receiving antenna with the same size as if it was evaluated at $f_{\mathrm{c}} = 2.4\,\mathrm{GHz}$ for a gain $G_{\mathrm{r}} = 1$. As a result, the receiving antenna gets more directive and needs to be physically pointing towards the transmitting array to have the maximum effective aperture computed in (3.7). That way, the path gain at the EN device location $\boldsymbol{p}_{\mathrm{EN}}$ yields $-25.8\,\mathrm{dBm}$, similar as for the physically large array case. The path gain over the whole cutting plane is evaluated for the concentrated antenna array case simulation and depicted in Figure 3.2. Note that the same scale has been used for the path gain in both Figure 3.1 and 3.2. Due to the linear relation between path gain PG and power density S, as is evident from (3.1), the figures demonstrate that physically large or distributed arrays have very positive effects on the spatial distribution of power density. Especially the very low power density levels close to their antennas positively aid the regulatory compliance of RW and reduce human exposure.

3.2.2 Compliance with EIRP limits

This far, the simulations have shown that physically large arrays are beneficial for adhering to power density limits. Using highly directed antennas or phased arrays capable of achieving large array gains may restrict the maximum transmit power through the regulated maximum EIRP limits (see Section 3.1.1). Similar as for the power density, near field beam focusing positively impacts the EIRP of physically large arrays: Although barely visible, behind the EN device, i.e., for ranges $r > d$, the path gain in Figure 3.1 decreases more rapidly than in Figure 3.2. In Figures 3.3

[7] Refer to (3.9) on page 25 for a definition of the corresponding precoding weights.
[8] See Table 6.3 on page 47 of REINDEER deliverable D2.1 [11].
[9] The directional dependence is neglected for simplicity.

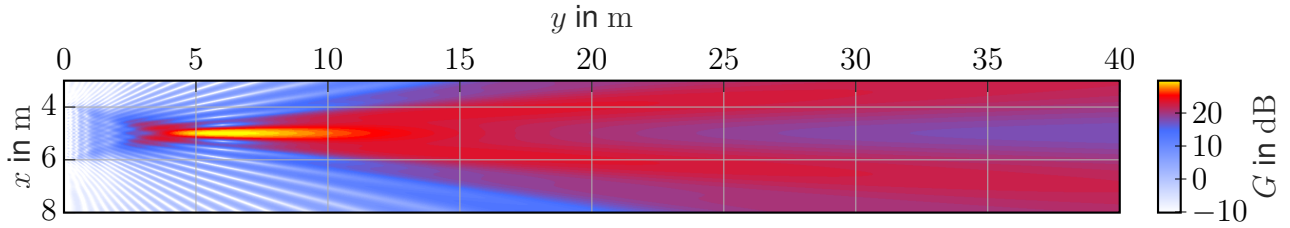

Figure 3.3: Near field array gain pattern $G(r, \theta, \varphi)$ computed for the physically large (or distributed) array operating at $f_\mathrm{c} = 2.4\,\mathrm{GHz}$.

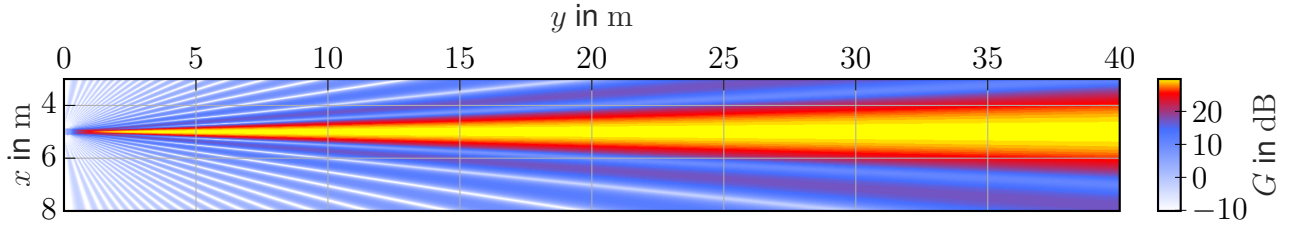

Figure 3.4: Near field array gain pattern $G(r, \theta, \varphi)$ computed for the physically small (concentrated) array operating at $\tilde{f}_\mathrm{c} = 24\,\mathrm{GHz}$.

and 3.4, we computed the *near field array gain pattern* for powers

$$G(\boldsymbol{r}) = \left| \sum_{\ell=1}^{L_\mathrm{t}} w_\ell \, e^{j\, k_0 \, \|\boldsymbol{r}_\ell\|} \right|^2 \tag{3.8}$$

where $\boldsymbol{r}_\ell = \boldsymbol{r} - \boldsymbol{p}_\mathrm{RW}^{(\ell)}$ is a vector from a transmit antenna ℓ to an arbitrary spatial point $\boldsymbol{r}$, $k_0 = \frac{2\pi}{\lambda}$ is the spatial angular frequency, and w_ℓ are the complex-valued beamforming weights computed using MRT from the channel vector[10] $\boldsymbol{h}(\boldsymbol{p}_\mathrm{EN})$ as

$$\boldsymbol{w} = \frac{\boldsymbol{h}^*}{\|\boldsymbol{h}\|} \qquad \text{with} \qquad \boldsymbol{h} = \sum_{k=1}^{K} \boldsymbol{h}_k + \boldsymbol{h}_{\mathrm{sc},k}\,. \tag{3.9}$$

Note that the array gain pattern in (3.8) is not inversely proportional to the squared distance, contrary to the path gain. Figure 3.3 depicts the near field array gain pattern of the physically large array, computed using (3.8). The figure shows a very low gain close to the RW panel, explaining how the path gain, or power density, respectively, can decrease for distances $r \ll d$ close to the array despite the inverse dependency on r^2. Furthermore, a low array gain behind the focal point (for $r \gg d$) is observable.
In the same manner, the near field array gain pattern computed for the physically small (concentrated) array is depicted in Figure 3.4. Although there is a decrease in array gain for distances $r \ll d$ close to the array, the trend is not strong enough to compensate for the inverse dependency on r^2. This explains the high path gain, or power density, respectively, close to the array in Figure 3.2. Furthermore, there is only a slight decrease in array gain observable for $r \gg d$.

[10] In the simulations conducted throughout this chapter we only used the LoS component ($k = 1$) of the SMC channel vector $\boldsymbol{h}_k$ and no scatter channel vector $\boldsymbol{h}_{\mathrm{sc},k}$.

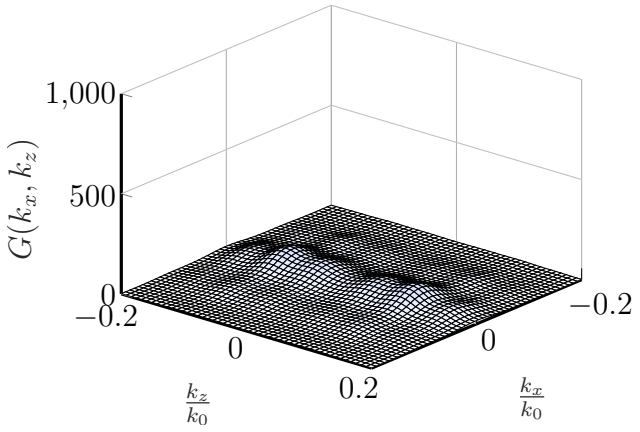

Figure 3.5: Far field array gain pattern of the physically large (or distributed) array operating at $2.4\,\mathrm{GHz}$.

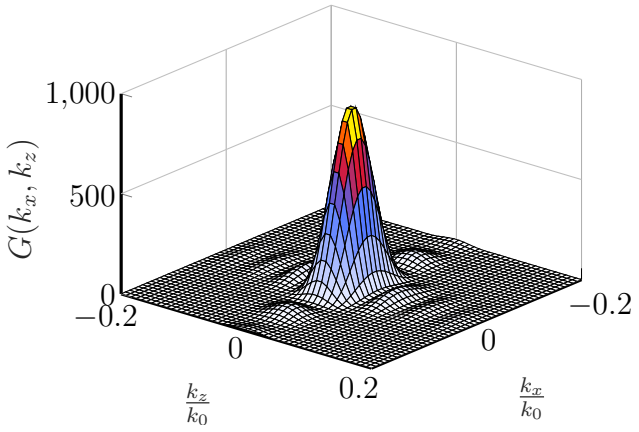

Figure 3.6: Far field array gain pattern of the physically small (or concentrated) array operating at $24\,\mathrm{GHz}$.

To highlight this fact, we compute the *far field array gain pattern* for powers[11]

$$G(\boldsymbol{k}) = \left| \sum_{\ell=1}^{L_\mathrm{t}} w_\ell \, e^{-j\,\boldsymbol{k}^\mathsf{T}\,\boldsymbol{r}_\ell} \right|^2 \overset{12}{=} \left| \sum_{\ell=1}^{L_\mathrm{t}} w_\ell \, e^{j\,\boldsymbol{k}^\mathsf{T}\,\boldsymbol{p}_\mathrm{RW}^{(\ell)}} \right|^2 , \tag{3.10}$$

where $\boldsymbol{k}$ is the wave vector defined as [26, p.43]

$$\boldsymbol{k} = \begin{bmatrix} k_x \\ k_y \\ k_z \end{bmatrix} = k_0 \begin{bmatrix} \sin\theta_\mathrm{a} \cos\varphi_\mathrm{a} \\ \sin\theta_\mathrm{a} \sin\varphi_\mathrm{a} \\ \cos\theta_\mathrm{a} \end{bmatrix} . \tag{3.11}$$

From the relations in (3.11) it becomes evident that, due to their dependence on the angular spherical coordinates $(\theta_\mathrm{a},\, \varphi_\mathrm{a})$ of the local array coordinate system, the wave vector components $(k_x,\, k_y,\, k_z)$ are confined to the *visible region* $[-k_0,\, k_0]$ [53, p.38]. Figures 3.5 and 3.6 show the far field array gain patterns[13] for the physically large and physically small arrays computed using (3.10), where the same MRT weights from (3.9) have been used. Figure 3.5 reflects the two dominant lobes in the xy-plane (along k_x) that are also visible in Figure 3.3. Figure 3.6 reflects the single dominant lobe that is already visible in Figure 3.4. Both figures show the same magnitude scaling for the vertical axis (i.e., the array gain pattern). The far field array gain, i.e., the maximum of the far field array gain pattern $G(\theta_\mathrm{a}, \varphi_\mathrm{a})$, in case of the physically small array is $G_\mathrm{s} \approx 909$. This is only a small decrease when compared to the maximum of the near field array gain pattern $\max\{G(r, \theta, \varphi)\} = L_\mathrm{t} = 960$. The far field array gain in case of the physically large array is $G_\mathrm{l} \approx 104$, i.e., the maximum of the array gain pattern in Figure 3.5. The difference in far field array gain achieved through using a physically large array in the given example is $\Delta G = \frac{G_\mathrm{s}}{G_\mathrm{l}} \approx \frac{909}{104} \approx 8.74 \approx 9.41\,\mathrm{dB}$ while both arrays would yield the same near field array gain

[11] For amplitudes, i.e., without taking the squared magnitude, the expression is what is sometimes termed *array pattern* or *beam pattern* in the literature [26, 53] and corresponds to the Fourier transform of the beamforming weights.

[12] The equality in (3.10) holds because only the relative layout of the antennas with respect to each other matters for the far field array gain pattern. Adding a constant phase shift $e^{j\,\boldsymbol{k}^\mathsf{T}\,\boldsymbol{r}}$, with $\boldsymbol{r}$ pointing in the same direction as $\boldsymbol{k}$, to all antennas ℓ does not affect the gain pattern.

[13] Due to their large extent in the spatial domain and correspondingly narrow beams in the angular domain, only a small portion of the visible region is plotted. However, no aliasing occurs due to Nyquist sampling in the spatial domain.

in the focal point. Thus, a physically large array focusing power in the near field could transmit at much higher transmit powers P_{t} (e.g., increased by ΔG) while exhibiting the same EIRP in the far field.

The advantages of the physically large and distributed architecture of a RW infrastructure can be summarized: The power density, and thus radiation exposure, close to the array is much smaller than in the case of using a physically small array of the same electrical size. This enables to achieve RF WPT with relatively low radiation levels, even if higher overall transmit powers are used. When operating well within the array near field, the interference it will cause in the array far field is quite low. Due to the low EIRP, larger transmit powers may be used. Furthermore, the presented results reinforce the suitability of the sub-$10\,\mathrm{GHz}$ spectrum for WPT, envisioned by the REINDEER consortium, rather than higher frequencies up to the mmWave range.

Regulatory standards for array near field operation

The investigated regulatory standards do not yet reflect range-dependent array gain patterns $G = f(r, \theta, \varphi)$. While this causes no discrepancies with human exposure regulations (see Section 3.1.2), there is no clear indication on how to apply EIRP limits on range-dependent gain patterns. Historically, the EIRP has been a convenient measure to limit the directional power radiation of a concentrated antenna, neglecting a strong increase in power density ($\propto 1/r^2$) close to the antenna. We have demonstrated that physically large arrays operating well within the array near field have very positive effects on the spatial distribution of power density and cause much less interference outside their targeted operation points in space. For radio infrastructures operating with distributed or physically large arrays, an adaptation of existing regulatory standards may become necessary. This will become increasingly significant if promising technologies in the field of wireless communications such as distributed massive MIMO, distributed antenna systems (DAS) and cell-free architectures gain traction in real-life use cases.

Chapter 4

Radio link analyses

In this section, the radio link of a RadioWeaves infrastructure is analyzed with respect to its WPT capabilities. That is, we analyze the WPT power budget in Section 4.1 as the maximum potential receive power. In Section 4.2 we analyze the communication link budget in terms of achievable SNR and data rates.

4.1 WPT power budget (downlink)

In Section 2.2, we have introduced a channel model that allows to compute the path gain PG, i.e., the RF-to-RF transmission efficiency η_{w}, and thus allows to model the received power in a physically correct manner. In Sections 2.3 and 3.2.1, we have measured and simulated the path gain to compute the WPT efficiency of exemplary systems. Building upon the regulatory compliance of RW discussed in Section 3.2, we derive the maximum receivable power under human exposure regulations in Section 4.1.1. Furthermore, we present how beam-diversity can be exploited to solve the initial-access problem, i.e., the first supply with sufficient power and wake-up of an EN device, in Section 4.1.2.

4.1.1 Maximum regulatory-compliant power budget

In Section 3.1 we have identified the EIRP and the power density as the important quantities subject to regulations. In Section 3.2 we have shown that for a single physically large array, focusing power well within the array near field can result in a small far field array gain, which positively impacts its compliance with EIRP limits. The given example may serve as a worst-case example as RadioWeaves is a *distributed* radio infrastructure [51]. Ideally it may consist of many radios that are spatially much more distributed than a single physically large array. Being more distributed will further decrease the far field array gain pattern while maintaining the same near field array gain. Furthermore, as we have discussed, regulations may need to be adapted for distributed or physically large architectures, as the EIRP is no longer a well-defined quantity for ensuring compliance with interference constraints.

The power density limit, however, may be the most stringent constraint that limits the maximum receivable power of a RW deployment. A radio infrastructure unaware of human bodies in its environment[1] must comply with the maximum power density levels of $S_{\max} = 10\,\mathrm{W/m^2}$ spatially

[1] Detection and tracking of human bodies may enable to establish radiation-safe zones around the whole bodies

Table 4.1: Maximum powers receivable through isotropic receive antennas (constant gain antennas) and constant aperture antennas at an incident power density of $10\,\mathrm{W/m^2}$ for a range of different frequencies. The conversion from effective aperture in $\mathrm{cm^2}$ to receivable power in mW is straightforward. Note that a constant aperture antenna would get more directive as the operating frequency increases (i.e., wavelength decreases), as evident from (4.3).

Frequency	**Isotropic antenna**			**Const. aperture antenna**		
	A_r	G_r	$P_\mathrm{r,max}$	A_r	G_r	$P_\mathrm{r,max}$
$868\,\mathrm{MHz}$	$95\,\mathrm{cm^2}$	1	$95\,\mathrm{mW}$	$95\,\mathrm{cm^2}$	1.00	$95\,\mathrm{mW}$
$2.4\,\mathrm{GHz}$	$12.4\,\mathrm{cm^2}$	1	$12.4\,\mathrm{mW}$	$95\,\mathrm{cm^2}$	7.65	$95\,\mathrm{mW}$
$3.8\,\mathrm{GHz}$	$4.96\,\mathrm{cm^2}$	1	$4.96\,\mathrm{mW}$	$95\,\mathrm{cm^2}$	19.2	$95\,\mathrm{mW}$
$5.0\,\mathrm{GHz}$	$2.86\,\mathrm{cm^2}$	1	$2.86\,\mathrm{mW}$	$95\,\mathrm{cm^2}$	33.2	$95\,\mathrm{mW}$
$6.0\,\mathrm{GHz}$	$1.99\,\mathrm{cm^2}$	1	$1.99\,\mathrm{mW}$	$95\,\mathrm{cm^2}$	47.8	$95\,\mathrm{mW}$

everywhere. Using a single receiving antenna, the maximum receivable power budget can be simply derived from (3.6) as

$$P_\mathrm{r,max} = \max\left\{\int_{A_\mathrm{r}} \boldsymbol{S}_\mathrm{max}\cdot d\boldsymbol{A}\right\} = A_\mathrm{r}\,S_\mathrm{max} \tag{4.1}$$

The effective area $A(\theta,\varphi)$ for an incident wave impinging from direction (θ,φ) is [37, 4]

$$A(\theta,\varphi) = G(\theta,\varphi)\,\frac{\lambda^2}{4\,\pi} \tag{4.2}$$

and thus the maximum effective aperture

$$A_\mathrm{r} = \max_{\theta,\varphi}\left\{G(\theta,\varphi)\,\frac{\lambda^2}{4\,\pi}\right\} = G_\mathrm{r}\,\frac{\lambda^2}{4\,\pi} \tag{4.3}$$

would be valid only for the direction of maximum gain. A hypothetical isotropic receiving antenna has a gain $G(\theta,\varphi) = 1$ regardless the incidence direction (θ,φ). If this antenna would stay isotropic for all frequencies, it would be a *constant gain antenna*, i.e., $G(f_i) = G(f_j)\,\forall f_i, f_j$. From (4.3) is becomes evident that the effective aperture A_r of a constant gain antenna decreases if the frequency increases and wavelength λ decreases. In Table 4.1, we compute the (maximum) effective apertures of isotropic antennas at various frequencies. Using (4.1), the maximum effective apertures directly translate into the maximum receivable powers $P_\mathrm{r,max}$. For isotropic antennas that can receive power from all incidence directions equally well, both the (maximum) effective apertures A_r and the maximum receivable powers $P_\mathrm{r,max}$ decrease unfavorably with increasing frequency.

Contrary to a constant gain antenna, the use of a *constant aperture antenna* allows to keep the maximum effective aperture A_r in (4.3) constant versus frequency, i.e., $A_\mathrm{r}(f_i) = A_\mathrm{r}(f_j)\,\forall f_i, f_j$, at the price of making the antenna more directive. That is, the antenna has a constant maximum receivable power $P_\mathrm{r,max}$ regardless of the operating frequency, in the direction where it exhibits its maximum gain $(\theta_\mathrm{max},\varphi_\mathrm{max}) = \arg\max_{\theta,\varphi} G(\theta,\varphi)$. For demonstration, we compute the maximum

where power density limits are adhered to, while using higher power levels outside. However, this is not discussed throughout this document.

receivable powers for a constant aperture antenna in Table 4.1. The maximum effective aperture of the chosen receiving antenna is $A_\mathrm{r} = 95\,\mathrm{cm}^2$, which corresponds to the aperture size of an isotropic antenna operating at $868\,\mathrm{MHz}$. Hypothetically, a constant aperture antenna could maintain high maximum receivable powers also for high frequencies. In reality, however, a range of problems arises if constant aperture antennas are used at high frequencies:

- To achieve the maximum receivable powers, all waves incident to the receiving antenna would have to impinge from a direction $(\theta_\mathrm{max}, \varphi_\mathrm{max})$, which would not be feasible in a distributed radio infrastructure.
- Even if the incident waves would originate from the direction of maximum gain, the achievable focal points or beam widths at high frequencies (e.g., millimeter wave (mmWave)) are small such that they would only cover a small portion of the maximum effective aperture. That is, even if a large receiving aperture A_r is formed with a normal vector $\boldsymbol{n}$ in parallel to the impinging power density $\boldsymbol{S}$, this does not mean that the high powers in the right column of Table 4.1 will be received. If a narrow beam is formed, the spatially dependent power density $\boldsymbol{S}$ will be large only within a small portion of the receiving aperture $\boldsymbol{A}_\mathrm{r}$ and thus the integral in (3.4) can still yield low received powers.
- As demonstrated in Section 3.2 (esp. Figure 3.2), concentrated $\frac{\lambda}{2}$-spaced arrays that would be formed at high frequencies result in high power densities close to the array which would prohibit that the maximum regulatory compliant power density S_max is only formed at the desired location of the receiving antenna.
  However, if an antenna spacing much larger than $\frac{\lambda}{2}$ and consequent grating lobes are acceptable, this does not hold true for distributed or physically large (aliased) arrays at higher frequencies.

For the reasons mentioned above, the values for a constant aperture antenna presented in Table 4.1 must be treated with caution. For the many reasons discussed throughout this document, lower operation frequencies are favorable for WPT. It is therefore no coincidence that RFID systems based on RF WPT have been implemented predominantly in the $900\,\mathrm{MHz}$ ISM band, i.e., ultra high frequency (UHF) RFID, rather than the $2.4\,\mathrm{GHz}$ ISM bands, even though regulatory standards would explicitly allow it.

An environment-aware radio infrastructure, i.e., a system aware of the geometry and reflectivity of its environment, is capable of predicting the spatial distribution of power density in its surroundings. It may optimize its power density radiated towards the focal point while spatially adhering to radiation constraints. For demonstration purposes, we evaluate the path gain across a cutting plane through an exemplary room. Figure 4.1 shows the simulation result from [10], where we simulate the same physically large array analyzed in Figure 3.1. The room has four walls and a floor with a chosen SMC gain of $|g_{\mathrm{SMC},k}| = -3\,\mathrm{dB}$. The EN device is placed at a distance $d = 8.125\,\mathrm{m}$ away from the transmitting array. It is placed in front of a wall that causes a strong standing wave pattern due to constructive and destructive interference between its incident and reflected waves. Randomly distributed scatterers behind the EN device cause diffuse reflections in its vicinity. In the simulated scenario, perfect CSI is assumed and MRT performed to compute the precoding weights $\boldsymbol{w}$. In this best-case scenario the path gain yields $PG = -23.8\,\mathrm{dB}$ assuming both isotropic transmit and receive antennas. At the simulated operating frequency $f_\mathrm{c} = 2.4\,\mathrm{GHz}$ the effective antenna aperture is $A_\mathrm{r} = 12.4\,\mathrm{cm}^2$, as shown in Table 4.1. The power density depends on the path gain trough the relation

$$P_\mathrm{r} = S\,A_\mathrm{r} = P_\mathrm{t}\,PG\,. \tag{4.4}$$

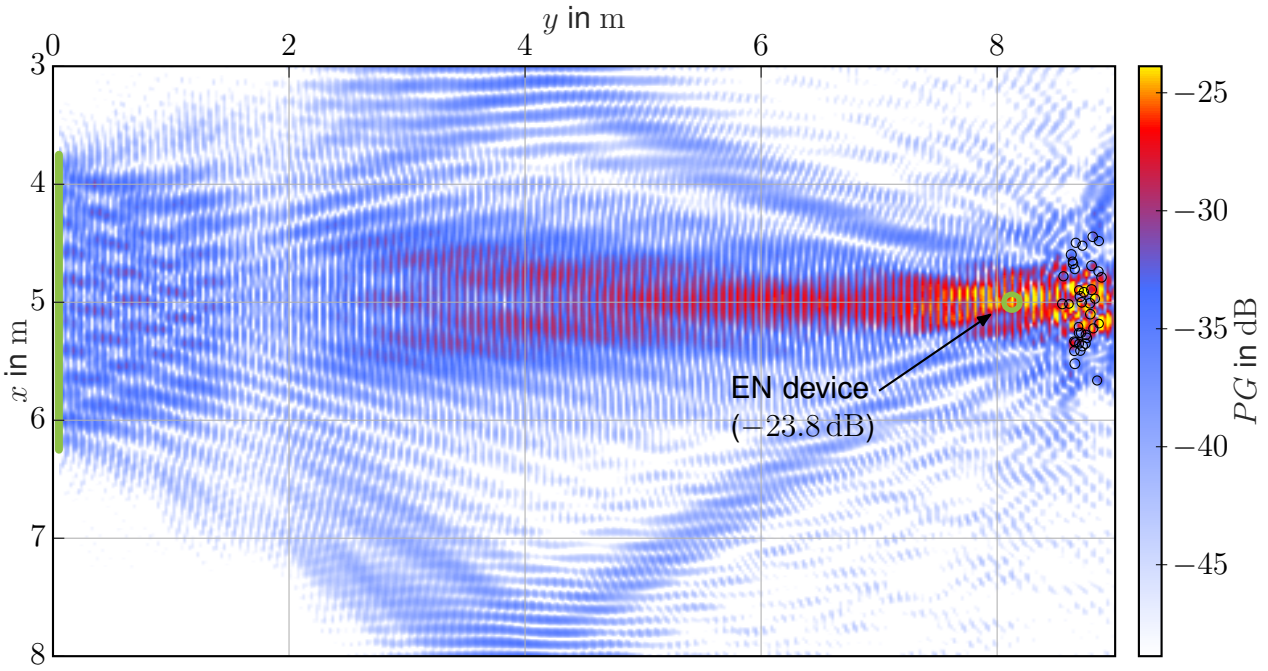

Figure 4.1: A simulation scenario from one of our works dealing with the initial access problem [10]: Path gain PG evaluated on a cutting plane (at $z = 1\,\mathrm{m}$, perpendicular to the center of the array) through the simulated room. MRT has been used for precoding, assuming perfect CSI including point scatterers.

If the array is transmitting at $P_\mathrm{t} = 3\,\mathrm{W}$, the power density within the focal point would be $S \approx 9.99\,\mathrm{W/m^2}$, which is just below the human exposure limit. The power received by the EN device is $P_\mathrm{r} \approx 10.9\,\mathrm{dBm} \approx 12.4\,\mathrm{mW}$. In Figure 4.1, the simulation result shows well how a simultaneous multibeam transmission is the power-optimal transmission scheme, inherent to applying MRT. Both through simulations and measurements in Section 2.3, we have shown that the efficiency, i.e., the path gain, can be increased by intentionally exploiting SMCs via walls, floor and ceiling.

4.1.2 Initial access distance and power budget

Solving the initial-access problem plays a central role in enabling the use of batteryless EN devices. In the initial access phase, the EN device has to be supplied with sufficient power to exceed the device sensitivity, i.e., the minimum power required for wake-up and backscatter communication [11]. Before an EN device has been woken up for the first time, CSI is usually not available, since the device needs some initial power supply to transmit its first signal upon which channel state estimation (CSE) can be performed. In Section 2.3, we have demonstrated on real-life measurements that spherical beamforming weights can be computed using geometric environment information. That is, without measured CSI available, it is possible to spatially focus power to desired points on predicted CSI.

If the positions of possible EN devices in the surroundings are unknown, a possible approach for initial access is beam sweeping, where the transmit array sweeps beams sequentially according to a predefined codebook [57] to power up the EN device for the first time. In indoor scenarios, environment-awareness can aid the choice for predefined codebooks, assuming that the possible locations of EN devices, as well as the propagation environment, are at least partially

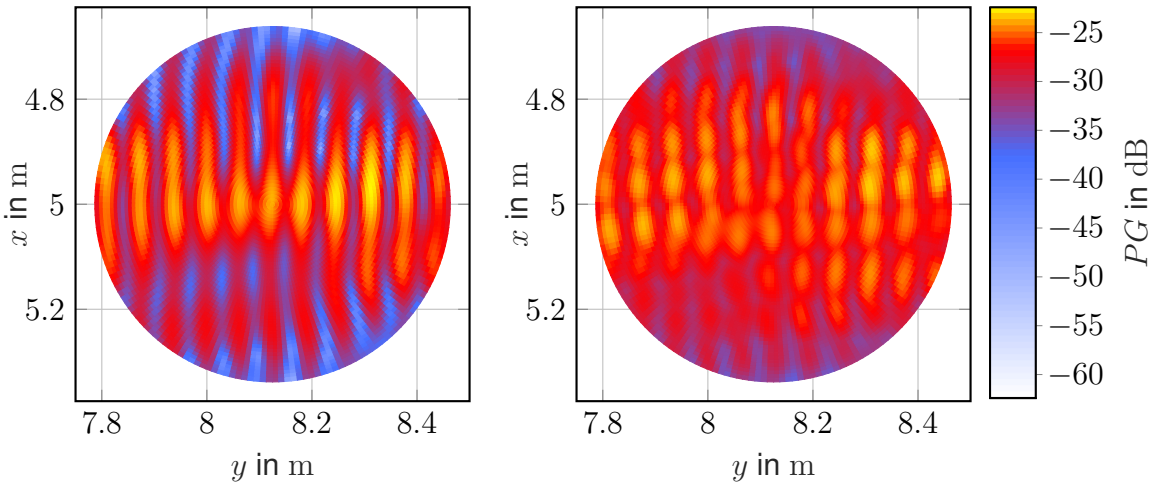

(a) Conventional MRT

(b) Beam diversity, $N_{\mathrm{R}} = 16$

Figure 4.2: Exploitation of beam diversity for initial access to EN devices in [10]: Path gains PG are evaluated on a circular disc in the xy-plane located around the focal point. The PG of conventional MRT in (a) is computed assuming full CSI. The PG in (b) is computed by predicting CSI using only geometric environment information and by varying the phases of the individual SMC beams randomly using $N_{\mathrm{R}} = 16$ realizations and taking the highest values.

known. However, beam sweeping in indoor scenarios suffers from fading due to severe multipath propagation, possibly originating from unknown objects in the environment. In [10], we demonstrate that *beam diversity* can be exploited to overcome these impairments: in a simultaneous multi-beam transmission from a single transmit array, the phases of the individual beams of the LoS and SMCs can be varied to reduce the necessary fading margin for the initial access to EN devices.

Using the simulation scenario depicted in Figure 4.1 and zooming in on the focal point reveals the strong standing wave pattern and multipath fading depicted in Figure 4.2 (a). If beam sweeping is employed to sequentially illuminate the environment, the strong deep fades caused by destructive interference of SMCs with the LoS impair the initial access to EN devices. To be woken up successfully, an EN device located at an unfavorable position of a deep fade needs a large fading margin M to be accounted for. This effectively reduces the potential power budget and resulting initial access distance. When exploiting beam diversity, however, illuminating the focal point via reflections from different SMC and varying the beam phases allows to even out the standing wave pattern around the focal point. Figure 4.2 (b) depicts the maximum path gains of $N_{\mathrm{R}} = 16$ random realizations of beam phases presented in [10]. Targeting an outage probability of less than $1\,\%$, a beam sweeping scheme using MRT (as depicted in Figure 4.2 (a)) would require an $M \approx 23\,\mathrm{dB}$ fading margin to compensate for deep fades in the focal point (see [10, 6]). A state-of-the-art EN device may have a front-end with a sensitivity[2] of $P_{\mathrm{r,\,min}} = -23\,\mathrm{dBm}$. Using the back-of-the-envelope power budget computations in [11, Eq. (6.21)], for simplicity, would yield an approximate

[2]We intentionally use the notation $P_{\mathrm{r,\,min}}$ to denote the front-end sensitivity (minimum required power for wake-up and backscatter communication) and make the distinguishment from the rectifier / charge pump sensitivity $P_{\mathrm{in}}^{\mathrm{sen}}$ in Sections 2.1.4 and 5.2.

initial access distance of

$$d_{\max} \approx \frac{\lambda}{4\pi}\sqrt{\frac{G_{\text{array}}}{PL_{\text{req}}}} \approx 9.85\,\text{m} \tag{4.5}$$

$$\text{with} \qquad PL_{\text{req}} = \frac{P_{\text{r,min}}}{P_{\text{t}}}\,M \qquad \text{and} \qquad G_{\text{array}} = L_{\text{t}}$$

when transmitting at $P_{\text{t}} = 1\,\text{W}$ and factoring in the required fading margin $M \approx 23\,\text{dB}$ with an array gain G_{array} equivalent to the total number of antennas for $L_{\text{t}} = 960$. This evaluation targets a Class 1 device or frontend in a Class 1 mode which has no capabilities of energy storage (please refer to Section 4.2.1 for more details on device classes). According to the RadioWeaves device classification [14, Section 3.1], devices of Class 1 have the lowest power consumption of all defined classes. We envision that all EN devices will feature a Class 1 mode [11, Section 6.3.2] that will aid the initial access and acquisition of CSI based on the first backscattered signal.
Exploiting beam diversity, i.e., simultaneously transmitting power to the focal point via multipath components (MPCs), as depicted in Figure 4.2 (b) reduces the necessary fading margin to $M \approx 11\,\text{dB}$ in the given example. According to the approximate calculation in (4.5) every $6\,\text{dB}$ fading margin halve the initial access distance. The improvement in fading margin of $\Delta M \approx 12\,\text{dB}$ through exploiting beam diversity could increase the initial access distance to $d_{\max} \approx 38.8\,\text{m}$ for the given transmit power and EN device sensitivity[3].

4.2 Link budget analyses for communication

WPT power budgets in terms of receivable power have been analyzed in Section 4.1. This section targets communication link budget analyses in terms of signal-to-noise ratio (SNR). Particularly, power-efficient backscatter communication with EN devices is investigated and its implications on receivable SNR and thus achievable data rates.

4.2.1 Communication with EN devices

In the REINDEER deliverable D1.1 [14, p. 32], 5 device classes were defined. Since the focus within this deliverable is on RF communication for EN devices, only Class 1 and Class 2 devices are eligible. For completeness, these definitions of Class 1, Class 2 and Class 3 devices are repeated.

- **Class 1:** EN devices, e.g., tags for tracking objects, that are supplied with RF energy through WPT. In the uplink, information is transmitted via backscatter communication only.
- **Class 2:** EN devices, with the capability of energy-storage and low power needs that only use backscatter communication in the uplink. A typical example could be an in-body sensor.
- **Class 3:** Battery-powered devices charged through mains-power or EN devices with energy storage charged wirelessly via WPT, with moderate functional capabilities, capable of actively transmitting radio signals. Energy-neutral augmented reality (AR) glasses are a representative example of this device class.

[3]The calculation serves as an example to demonstrate the potential of exploiting beam diversity. It must be noted, however, that the possible improvement in fading margin will be dependent on the location and distance of the EN device and its surroundings.

These device classes 1 and 2 should use RF backscattering for the uplink. Before discussing the uplink, the downlink will be examined.

4.2.2 Downlink data transfer

Downlink communication for EN devices will only occur sporadically for most EN devices, e.g., when an update, acknowledgment or data transfer is due. If data transfer has to take place, for example to send the display image to an electronic label, it will involve small data packages. This makes it possible to work with low data rates, allowing to use simple modulation techniques such as amplitude shift keying (ASK), frequency shift keying (FSK) or phase shift keying (PSK). To reduce the complexity, cost and power consumption of the EN device, it is recommended to use a similar modulation technique for both the downlink and uplink. This allows the demodulation and modulation hardware to be partially used for both cases. Since the uplink is more difficult to realize on a hardware level than the downlink, the downlink modulation technique will depend on the applied uplink modulation technique, which is discussed in Section 4.2.3.

To get an indication of the maximum feasible bit rate $R_{\max}$ for the downlink within an AWGN channel, the Shannon-Hartley theorem can be used:

$$R_{\max} \leq B \log_2(1 + \mathrm{SNR}) \tag{4.6}$$

with B the bandwidth of the channel in Hz. The SNR can be described using the spectral efficiency η_{sp}, the energy per bit E_{b} and the noise power spectral density N_0, resulting in:

$$R_{\max} \leq B \log_2 \left(1 + \eta_{\mathrm{sp}} \frac{E_{\mathrm{b}}}{N_0}\right). \tag{4.7}$$

The maximum achievable data rate is in the above equation linearly[4] dependent on the channel bandwidth, which in this case is determined by the EN device itself since the bandwidth depends on the hardware design. However, in lower SNR regimes, the noise power depends on this bandwidth as well. Equation 4.6 is an accurate link performance proxy for longer blocks lengths. Depending on the amount of data that needs to be transmitted, a penalty factor can be multiplied with the SNR, to account for the finiteness of the block lengths.

Often simple low-power control systems or microcontrollers will be used, making the sample rate a limiting factor. Given an equal bandwidth, a trade-off can be made between a more complex and energy-consuming design with higher spectral efficiency, e.g. with quadrature amplitude modulation (QAM) and thus higher data rate, or a simple design for example based entirely on ASK carrier modulation which consumes less power and provides lower data rates.

Figure 4.3 gives an overview of recently reported ASK, PSK and FSK demodulators found in literature with their respective power consumption and achievable data rates. All three demodulator techniques can achieve the lower data rates whilst demanding only a few $\mu\mathrm{W}$ of power, as described in the use cases in REINDEER deliverable D1.1 [14]. For increased data rates at this limited power budget, the best option according to the literature is to use ASK modulation,

[4] In fact, only in the bandwidth limited regime, i.e., for small bandwidths B, the channel capacity will increase almost linearly with the bandwidth. The SNR decreases with an increasing bandwidth and thus the channel capacity is an increasing, concave function of B [49, Section 5.2.2].

which is also relatively easy to implement using backscattering. The trade-off between power consumption and data rate with this technique seems to be the practically most suitable.

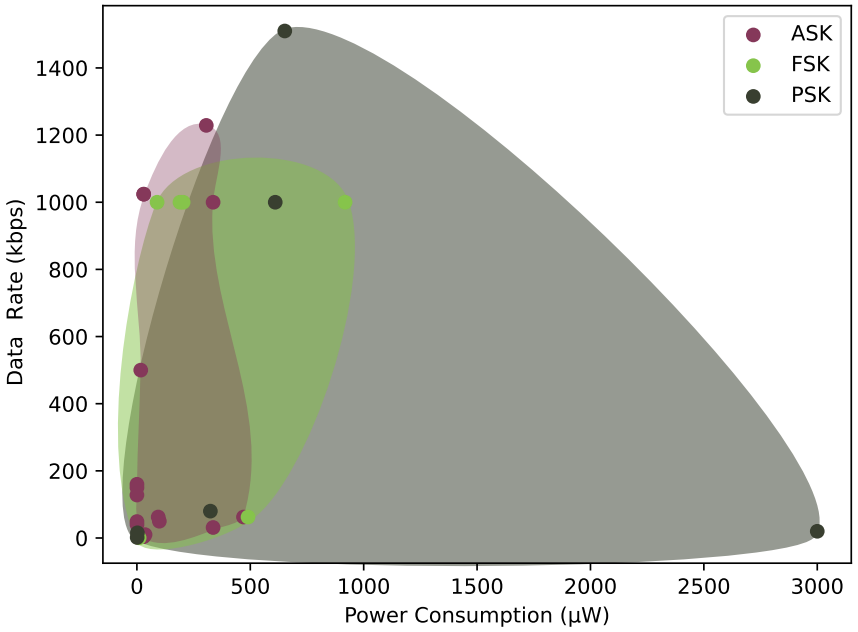

Figure 4.3: Overview of recently reported, low power ASK, FSK and PSK demodulators and their maximum achievable data rates.

4.2.3 Uplink (backscatter) data transfer

To enable uplink data transfer on energy-neutral devices, backscatter communication is considered. Compared to traditional RF communications, signals are no longer transmitted via a powered RF generator or active transmitter. In backscattering, incoming RF signals from a separate source are either reflected or absorbed to deliver information to another receiver. Backscattering is based on radar principles. For far field[5] communication, analysis and design are conventionally based on the previously mentioned Friis transmission equation and the radar range equation, like our channel model in Section 2.2. We start our derivation based on a SISO model to discuss relevant mechanisms involved in backscatter communication on a simplified model. In Section 4.2.4 we compute back-of-the-envelope data rates achievable in backscatter communication links. We eventually relate our derivations to a MISO model and to demonstrate gains achievable

Bistatic, dislocated link budget

The far field parameter used to characterize the scattering properties of a radar target is the radar cross section (RCS) σ. According to [4], it is defined as *a fictive area intercepting that amount of power, which, when scattered isotropically, produces at the receiver a density which is equal*

[5]The *antenna far field* is of concern here in contrast to the *array far field*. I.e., the transmitting and receiving antennas are separated by the Fraunhofer distance $d_{\mathrm{F}} = \frac{2D^2}{\lambda}$, where D is the largest dimension of the transmitting *antenna*, rather than the transmitting *array*.

to that scattered by the actual target. It depends on the relative position of target and transmitter/receiver, target geometry and material, frequency, angular orientation and transmitter/receiver polarization [28].

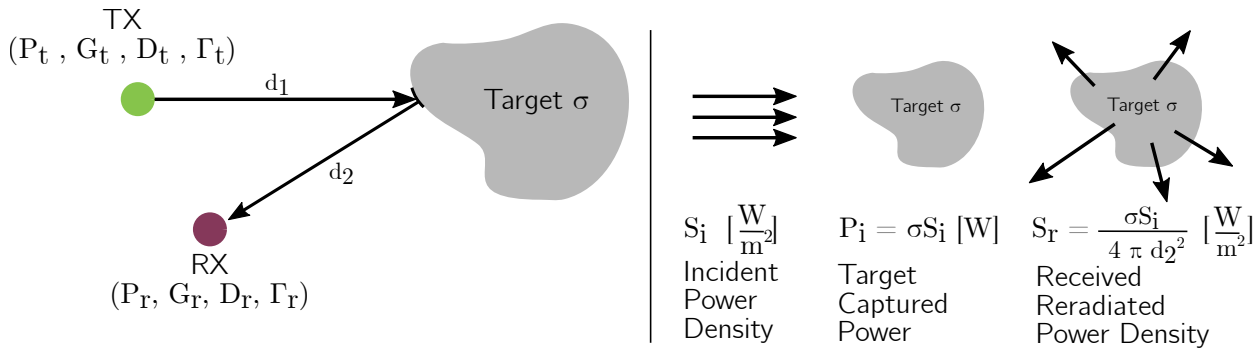

Figure 4.4: Simplified visualization of the RCS [9].

A more intuitive approach for the RCS in a bistatic setup, in which the transmitter and receiver at the infrastructure side are separated, is depicted in Figure 4.4. In this bistatic setup, d_1 represents the distance between the transmitting antenna and the backscatter device and d_2 the distance between the backscatter device and receiving antenna. The transmitted power P_t is radiated by the transmitter and some portion of it is observed by a target, at a distance d_1 from the source. The incident power P_i that is intercepted by the target is determined by the incident power density S_i and the RCS σ, so that the captured power is σS_i. This intercepted power is either reradiated as scattered power or absorbed as heat. Isotropic reradiation delivers a scattered power density S_r at distance d_2 from the target given by:

$$S_\mathrm{i} = \frac{P_\mathrm{t} G_\mathrm{t}}{4\pi d_1^2} \tag{4.8}$$

$$P_\mathrm{s} = \sigma S_\mathrm{i} = \sigma \frac{P_\mathrm{t} G_\mathrm{t}}{4\pi d_1^2} \tag{4.9}$$

$$S_\mathrm{r} = \frac{\sigma S_\mathrm{i}}{4\pi d_2^2}. \tag{4.10}$$

Combining the above equations with the Friis transmission equation gives the relation between the radar cross section, the transmitted power of the transmit antenna and the received power by the receiving antenna as a function of the different distances and the RCS in case of polarization-matched and aligned antennas:

$$P_\mathrm{r,b} = \sigma_i \left(1 - |\Gamma_\mathrm{t}|^2\right) \left(1 - |\Gamma_\mathrm{r}|^2\right) \left(\frac{\lambda}{4\pi d_1 d_2}\right)^2 \frac{G_{\mathrm{t},1} G_\mathrm{r}}{4\pi} \left|\boldsymbol{\rho}_\mathrm{t} \cdot \boldsymbol{\rho}_\mathrm{b}\right|^2 \left|\boldsymbol{\rho}_\mathrm{b} \cdot \boldsymbol{\rho}_\mathrm{r}\right|^2. \tag{4.11}$$

This equation is also known as the *bistatic radar range equation* that has already been used to model DM in our channel model in Section 2.2.2. In fact, an EN device acts like a single scatter point that is able to vary (i.e., modulate) its RCS and thus backscatter a desired signal. A digital or analog data signal coming from a EN device can *backscatter* this signal on a received incoming wave by altering its RCS value σ. The above equation provides a description of the RCS, but does not state clearly how it can be altered on a hardware level. In practice, the target

is implemented as an antenna with an antenna gain G whose RCS can be altered. Green [22] introduces a load-dependent radar cross section definition as:

$$\sigma_i = \frac{\lambda^2}{4\pi} G_{\mathrm{b}}^2 \left|\Gamma_{\mathrm{b},i} - A_{\mathrm{s}}\right|^2 . \tag{4.12}$$

It contains two important design parameters: the antenna mode $\Gamma_{\mathrm{b},i}$ and the structural mode A_{s}. The antenna mode is load dependent:

$$\Gamma_{\mathrm{b},i} \triangleq \frac{Z_i - Z_{\mathrm{a}}^*}{Z_i + Z_{\mathrm{a}}} \tag{4.13}$$

where Z_{a} is the target antenna impedance and Z_i the load impedance of this target antenna. The *antenna mode* describes the power absorbed in the load of a lossless antenna and the power which is reradiated by the antenna due to load mismatch. The index term i depends on the number of different antenna loads connected to the antenna, resulting in different backscattered signal amplitudes and phases. The second mode that was derived from (4.12) is the *structural mode* A_{s} scattering term which depends on the antenna shape, size and materials [44, 24]. The received, modulated backscatter power for a bistatic, dislocated setup becomes:

$$P_{\mathrm{r,b}} = \left(1 - |\Gamma_{\mathrm{t}}|^2\right)\left(1 - |\Gamma_{\mathrm{r}}|^2\right)\left|\Gamma_{\mathrm{b},i} - A_{\mathrm{s}}\right|^2 \frac{\lambda^4}{(4\pi)^4 d_1^2 d_2^2} G_{\mathrm{t},1} G_{\mathrm{r}} G_{\mathrm{b}}^2 \left|\boldsymbol{\rho}_{\mathrm{t}} \cdot \boldsymbol{\rho}_{\mathrm{b}}\right|^2 \left|\boldsymbol{\rho}_{\mathrm{b}} \cdot \boldsymbol{\rho}_{\mathrm{r}}\right|^2 . \tag{4.14}$$

By varying the antenna load, only the antenna mode of the RCS value is altered, resulting in a changing electromagnetic field at the receiving antenna. For analog signals, a linear load, like the transimpedance of a junction field effect transistor (JFET), can be changed depending on the incoming signal. For digital signals, the difference in RCS between a '1' and a '0' should be optimized for a maximal backscatter link distance. The most convenient method would be to use the Thevenin equivalent circuit of an antenna [39]. Solving this circuit for an antenna connected to a load Z_i, $i \in \{1, 2\}$ leads to a differential RCS $\Delta\sigma$ [36]:

$$\Delta\sigma = \frac{\lambda^2 G_b^2}{4\pi} \left|\Gamma_{b,0} - \Gamma_{b,1}\right| . \tag{4.15}$$

This is only true for minimum scattering antennas, as noted carefully in [36], where the antenna structural mode $A_{\mathrm{s}} = 1$. Extended research on different modulation techniques (ASK, FSK, PSK, QAM in [52]), shows that this is often (wrongly) supposed, neglecting the structural mode of the RCS equation, producing potentially sub-optimal backscatter link distance results. Ideally, this should incorporate both the antenna and structural modes. For optimal binary communication (with $i \in \{0, 1\}$), there are two constraints that should be kept in mind [5]:

1. The loads Z_0 and Z_1 should be chosen in a way that the total backscatter signal power is maximized: $\max(\sigma_0 + \sigma_1)$. This way, the chance to receive power above the reader's sensitivity is increased.
2. Minimize the bit error rate (BER) probability at the reader. The corresponding maximum likelihood detection in the presence of zero-mean, additive complex circularly symmetric Gaussian noise ($\mathcal{N}_0$), can be directly computed [50] with the Q-function. The probability of such error e detection is expressed as $\Pr\{e\} \triangleq Q\left(|h|\left|a\vec{E}_0\right|\frac{|\Gamma_0 - \Gamma_1|}{2\sqrt{\frac{\mathcal{N}_0}{2}}}\right)$. To minimize this BER, the reflection coefficient difference amplitude should be maximized: $\max(\Gamma_0 - \Gamma_1)$.

However, complex measurements are necessary to determine the *structural* mode of the RCS. As a solution, the antenna is commonly switched between short and open state, trading the potential improved backscatter link distance in for ease of use. The received backscattered signal is weak due to the energy loss when propagating, absorption by the antenna loads, the lower antenna gains in certain directions, and the negative influence of the structural mode. This makes the signal vulnerable to noise and fading.

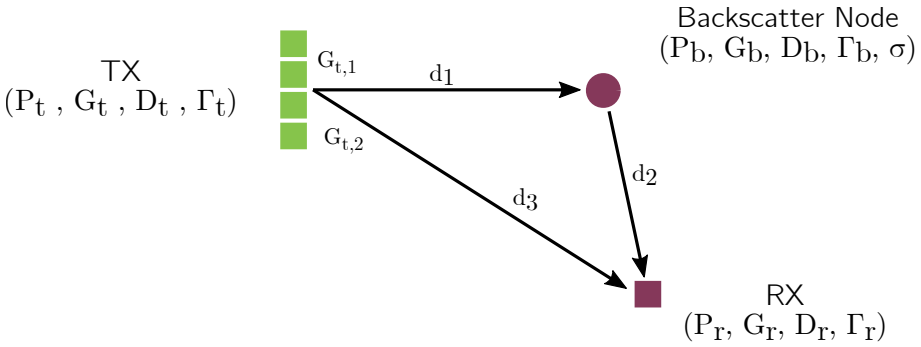

Figure 4.5: Bistatic, dislocated backscattering setup.

The total received signal power does not only depend on the signal coming from the backscatter device. The carrier wave transmitter and noise affect this signal as well (Figure 4.5). This total received signal power can be rewritten as:

$$\begin{aligned} P_{\mathrm{r,tot}} &= P_{\mathrm{r,t}} + P_{\mathrm{r,b}} + N \\ &= \left(1-|\Gamma_{\mathrm{t}}|^2\right)\left(1-|\Gamma_{\mathrm{r}}|^2\right)\left(\frac{\lambda}{4\,\pi\,d_3}\right)^2 P_{\mathrm{t}}\,G_{\mathrm{t},2}\,G_{\mathrm{r}}\,|\boldsymbol{\rho}_{\mathrm{t}}\cdot\boldsymbol{\rho}_{\mathrm{r}}|^2 + \\ &\sigma_i\,\left(1-|\Gamma_{\mathrm{t}}|^2\right)\left(1-|\Gamma_{\mathrm{r}}|^2\right)\left(\frac{\lambda}{4\pi d_1 d_2}\right)^2 \frac{G_{\mathrm{t},1}G_{\mathrm{r}}}{4\pi}\,|\boldsymbol{\rho}_{\mathrm{t}}\cdot\boldsymbol{\rho}_{\mathrm{b}}|^2\,|\boldsymbol{\rho}_{\mathrm{b}}\cdot\boldsymbol{\rho}_{\mathrm{r}}|^2 + N. \end{aligned} \tag{4.16}$$

Where the noise term is often assumed to be AWGN in literature, with a power of $N = N_0 B$ at bandwidth B and noise power spectral density N_0.

The SNR of the received signal can be written as:

$$SNR = \frac{P_{\mathrm{r,b}}}{P_{\mathrm{r,t}} + N}. \tag{4.17}$$

Due to the dense power spot obtained via the physically large array we envisioned and described in Section 3.1.2, the SNR of the received signal will be largely improved compared to the omnidirectional transmitters used in conventional setups.

Backscatter modulation

Load switching of a single-tone incident wave is adopted in this work as it presents the most simple form of ASK modulation i.e., on-off keying (OOK). It is easy to implement, inexpensive and has demonstrated its ability to perform backscattering in several wireless technologies [12, 25]. However, this modulation method has a major drawback, namely it is highly susceptible to noise. In the time domain, an RF source sends out the carrier wave $y(f_{\mathrm{c}}, t)$, a single tone sine wave with a frequency f_{c}, and the backscatter device changes the RCS at a frequency of Δf_{a}. A_1 and A_2

represent the path loss of the electromagnetic waves. In the bistatic setup, a separate antenna receives the sum of the carrier wave and the OOK demodulated signal:

$$R(t) = A_1\, y(f_c, t) + A_2\, \sigma(\Delta f_a, t) \cdot A_1\, y(f_c, t) \tag{4.18}$$

As backscattering is a mixing process, the OOK backscattered signals appear as sidelobes on the positive and negative side of the single-tone carrier wave in the spectrum. In other words, the reflective and incoming wave spectra overlap. This approach suffers from self interference as Δf_a is relatively small, and without proper cancellation can not be distinguished from the carrier wave due to the limited resolution of the receiver. This becomes apparent when two or more nodes are available in the same backscatter network. Not only can there be in-band interference between the transmitted and reflected signal, but between different backscattered signals as well. With increasing distance, these signals ultimately become too weak to be separated from the noise floor or from out-of-band interference.

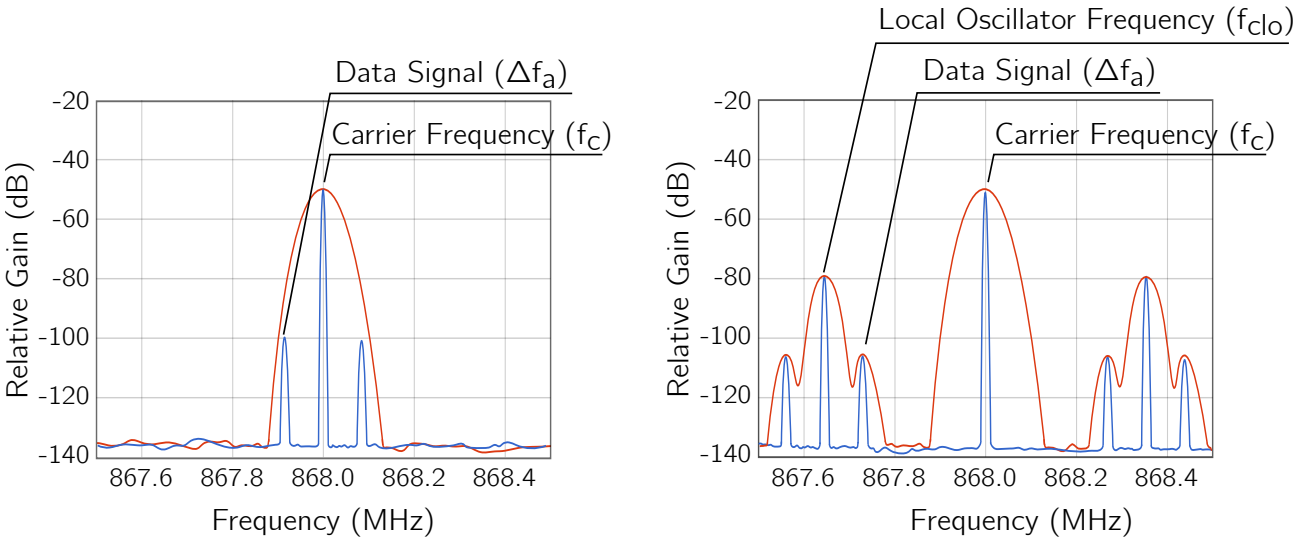

Figure 4.6: Frequency spectra of the combined direct and backscattered received RF signals without the local oscillator at the backscatter device (left). The blue and red lines on both figures represent the spectra for respectively a small and a large resolution bandwidth. By adding the local oscillator, the backscattered signals are shifted away from the carrier, improving distinctiveness and enabling reception at lower spectral resolution.

A solution for the two self-interference problems is achieved through frequency translation backscatter [54], where mixing capabilities of the backscatter principle are used to its advantage. This requires an extra component on the backscatter device. A local oscillator, generating a sine wave at a frequency f_{clo}, moves the signal away from the direct carrier in the frequency domain. The offset of $f_c \pm f_{\text{clo}}$ can be seen at both sides (Figure 4.6). On these two mirror frequencies, the received encoded signal again appears as a double sideband modulated signal. Assuming the RCS variation is defined by a sine wave, the second term of (4.18) can be rewritten with the product to sum identities as:

$$\begin{aligned} &\sin(f_a\, t) \cdot \sin(f_{\text{clo}}\, t) \cdot \sin(f_c\, t) = \\ &\quad \frac{1}{4}\Big(\sin\big((f_c - \Delta f_a + f_{\text{clo}})\, t\big) + \sin\big((f_c + \Delta f_a - f_{\text{clo}})\, t\big)\Big) \\ &\quad - \frac{1}{4}\Big(\sin\big((f_c - \Delta f_a - f_{\text{clo}})\, t\big) + \sin\big((f_c + \Delta f_a + f_{\text{clo}})\, t\big)\Big) \end{aligned} \tag{4.19}$$

The added local oscillator contributes to a higher power consumption, yet it is an excellent compromise for the gained backscatter link distance. Additionally, it allows for a multiple access implementation. By selecting a different local oscillator frequency for each mobile node, frequency division multiple access (FDMA) can be adapted. However, due to the double side band modulation, the maximum amount of potential simultaneously communicating nodes is halved. Complex single sideband mixers, such as in [56] with two separate loads could cancel out one band but at the same time consume more energy and require a larger complexity on the mobile node. Carrier sensing can be performed at the signal generator, sensing the RF spectrum and selecting the carrier frequency at which the chance of possible collisions with ambient wireless traffic is lowest.

Backscatter demodulation

As this proposed method does not require any complex self-interference cancellation mechanism on a hardware or software level, a simple radio can be used to demodulate the backscatter signal to retrieve the necessary information out of the RF-signal at the receiver. With the addition of the local oscillator on the backscatter device, two types of demodulation can be performed:

1. OOK demodulation. The digitized signal drives a multiplexer that forwards either the local oscillator or no signal at all. Consequently, the load is switched at the local oscillator frequency f_{clo} or it does not get switched. In the spectrum, this appears as a signal f_{clo} away from the RF carrier frequency that gets turned on and off. As aforementioned, OOK is very susceptible to noise, and the drift of the local oscillators can make the amplitude demodulation on the receiving radio impossible.
2. FSK demodulation. As the data signal Δf_{a} can be considered as a signal modulated in frequency, this data signal can be observed on both sides of the local oscillator frequency. The demodulation is often done by performing a frequency translation and a decimating FIR filter on one of the sidebands. With this, only the portion of the wideband signal with the data signal is saved to a buffer for later use.

In Figures 4.7 and 4.8, a snapshot of both the spectrum and the received signal of a backscattered signal in the time domain can be observed. FSK is used for demodulating the backscattered signal. This constant envelop modulation is more robust against fading and non-linear amplification. Additionally, FSK can achieve a lower BER for the same signal-to-noise ratio. The two sides of the spectrum are plotted, clearly showing the powerful RF carrier wave, the local oscillator frequency, and the two data sidebands.

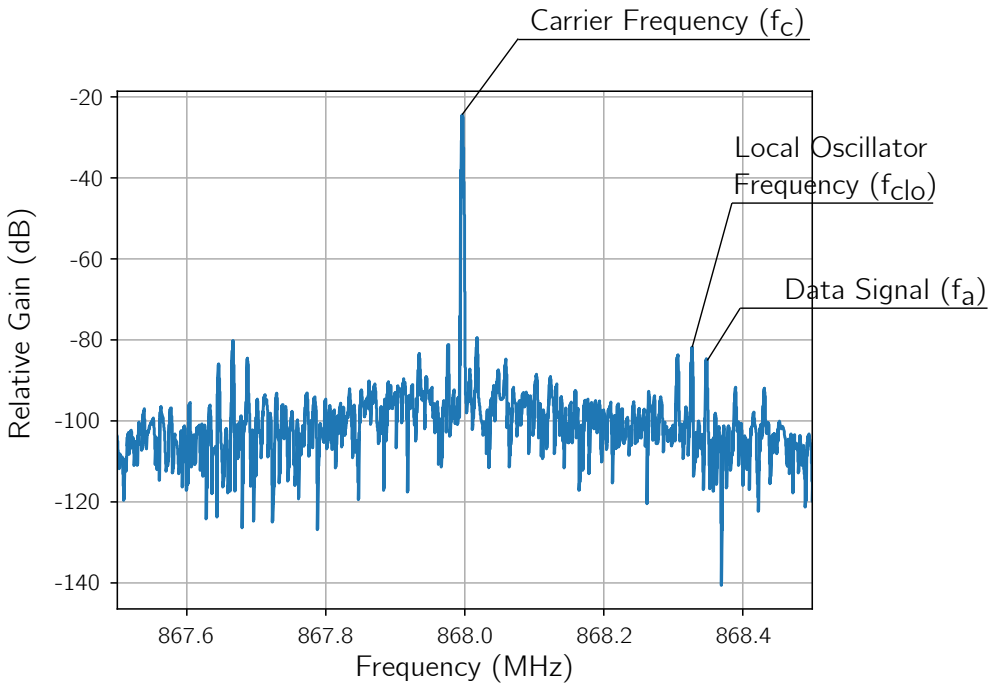

Figure 4.7: Spectrum of a received backscattered signal, showing the two symmetric sidebands with the RF carrier frequency as center.

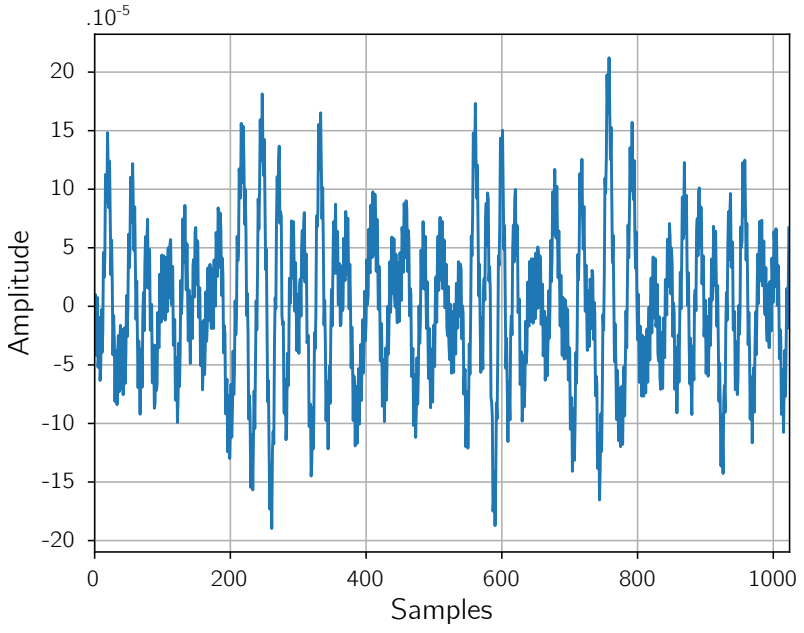

Figure 4.8: $1\,\mathrm{ms}$ of samples from an FSK-demodulated backscattered signal in the time domain.

The achievable data rates clearly depend on the used hardware, with the receiver radio sampling speed and backscatter switch hardware being important components.

4.2.4 Feasible backscatter data rate

The feasible data rate for ASK backscatter communication can be approximated when replacing the SNR-term in the Shannon-Hartley theorem in (4.6) with the according backscatter SNR in (4.17). For this latter equation, the differential received backscatter signal power coming from the backscatter device $\Delta P_{\mathrm{r,b}}$ is introduced, including the aforementioned differential RCS term. In the ideal case of LoS, perfectly tuned antennas and no polarization at both the receive and transmit antenna, this equation becomes:

$$\Delta P_{\mathrm{r,b}} = P_{\mathrm{t}}\,\Delta\sigma\,\frac{\lambda^2\,G_{\mathrm{t}}\,G_{\mathrm{r}}}{(4\pi)^3\,d_1^2\,d_2^2}\,. \tag{4.20}$$

Within an AWGN channel, the minimum received noise is defined by the noise floor and depends on the noise figure F of the used hardware, the bandwidth B and the noise power density N_0. The latter is defined by the temperature T in Kelvin and Boltzmann constant k.

$$N = 10\log_{10}\left(kT\,\frac{\mathrm{Hz}}{1\,\mathrm{mW}}\right) + F + 10\log_{10}(B) \tag{4.21}$$

At $19\,℃$, the noise power density is equal to $-173.98\,\mathrm{dBm/Hz}$. The maximum data transfer determined by Shannon-Hartley theorem becomes:

$$\begin{aligned} R_{\max} &\leq B\cdot\log_2(1+\mathrm{SNR}) \\ &\leq B\cdot\log_2\left(1+\frac{P_{\mathrm{t}}\,\Delta\sigma\,\frac{\lambda^2\,G_{\mathrm{t}}\,G_{\mathrm{r}}}{(4\pi)^3\,d_1^2\,d_2^2}}{P_{\mathrm{t}}\,\frac{\lambda^2\,G_{\mathrm{t}}\,G_{\mathrm{r}}}{(4\pi)^2\,d_3^2}+N}\right)\,. \end{aligned} \tag{4.22}$$

In what follows, a numerical example for a true-to-life use case is resolved for a bistatic, dislocated backscatter setup in an indoor environment as depicted in Fig. 4.5. We make the following assumptions, as summarized in Table 4.2. Both the transmit and receive antenna are $\lambda/2$ dipoles with a gain of $G_{\mathrm{t},1} = G_{\mathrm{t}_2} = G_{\mathrm{R}} = 2.15\,\mathrm{dBi}$. The center frequency for the backscatter communication is chosen at $868\,\mathrm{MHz}$, which results in a wavelength of $0.35\,\mathrm{m}$. The chosen differentials RCS at this frequency is based on measurements performed on a NXP UCODE 7 RFID tag in [35] and equals $-15\,\mathrm{dBsm}$ or $0.0316\,\mathrm{m}^2$. d_1, d_2 and d_3 are respectively set to: $9\,\mathrm{m}$, $7.5\,\mathrm{m}$ and $13.5\,\mathrm{m}$. Regarding the noise figure, a representative number has been taken from the datasheet of the TI™ CC2590 $2.4\,\mathrm{GHz}$ RF Front End, with a worst case value around $5\,\mathrm{dB}$ [47, Figure 3]. The maximum transmit power P_{t} and bandwidth B are defined by the 802.11 WiFi standard, operating in the sub-GHz (802.11ah), $2.4\,\mathrm{GHz}$ and $5\,\mathrm{GHz}$. For the first band, the transmit power and bandwidth are respectively limited to $10\,\mathrm{dBm}$ and $1\,\mathrm{MHz}$, for the latter two, these values are $20\,\mathrm{dBm}$ and $20\,\mathrm{MHz}$.

The upper half of Table 4.3 summarizes the maximum data rates for the introduced SISO system at different frequencies with the aforementioned, favourable parameters in Table 4.2. We analyze two cases: In the first use case, no local oscillator is used to shift the data signal away from the carrier frequency. Equation (4.22) remains unaltered and for lower bandwidths, there is a linear relationship between this bandwidth and the maximum data rate. In the second use case, a local oscillator is added to the backscatter device. The noise term of the SNR-equation is no longer

Table 4.2: Overview of the data used in for the feasible data rate calculations.

Physical modality	Symbol	Frequency	Value
Antenna gains	$G_\mathrm{t}, G_\mathrm{r}$		$2.15\,\mathrm{dBi}$
Array gain	G_array		$30\,\mathrm{dB}$
Differential RCS	$\Delta\sigma$		$-15\,\mathrm{dBsm}$
Distances	d_1, d_2, d_3		$9\,\mathrm{m}$, $7.5\,\mathrm{m}$, $13.5\,\mathrm{m}$
Noise figure	F		$5\,\mathrm{dB}$
Wavelength	λ	$868\,\mathrm{MHz}$	$0.346\,\mathrm{m}$
		$2.4\,\mathrm{GHz}$	$0.125\,\mathrm{m}$
		$5.0\,\mathrm{GHz}$	$0.060\,\mathrm{m}$
Transmit power (802.11)	P_t	$868\,\mathrm{MHz}$	$10\,\mathrm{dBm}$
		$2.4\,\mathrm{GHz}$	$20\,\mathrm{dBm}$
		$5.0\,\mathrm{GHz}$	$20\,\mathrm{dBm}$
Bandwidth (802.11)	B	$868\,\mathrm{MHz}$	$1\,\mathrm{MHz}$
		$2.4\,\mathrm{GHz}$	$2\,\mathrm{MHz}$
		$5.0\,\mathrm{GHz}$	$2\,\mathrm{MHz}$

defined by the carrier wave signal, coming from the transmit antenna, as this can be filtered out easily. The altered Shannon-Hartley equation becomes:

$$\begin{aligned} R_\mathrm{max} &\leq B \cdot \log_2\left(1 + \mathrm{SNR}\right) \\ &\leq B \cdot \log_2\left(1 + \frac{P_\mathrm{t}\,\Delta\sigma\,\frac{\lambda^2\,G_\mathrm{t}\,G_\mathrm{r}}{(4\pi)^3\,d_1^2\,d_2^2}}{N}\right). \end{aligned} \tag{4.23}$$

The maximum data rate will follow the natural logarithm function and saturate with the increasing bandwidth. Note that the maximum bandwidth in this case depends on the local oscillator frequency. If the bandwidth exceeds this frequency, the carrier frequency will be received as well, and Equation (4.22) should be applied. Compared to the achieved data rates in other literature (Table 4.4), the data rate is increased at lower carrier strengths but for smaller distances. For similar distances and carrier strengths, the altered Shannon-Hartley equation gives comparable results.

Table 4.3: Overview of the maximum, best-case data rate. The term MISO relates to the fact that the array gain is only exploited in the downlink to the EN device and not in the (backscattered) uplink from the EN device, closely corresponding to the initial access problem described in Section 4.1.2.

SISO data rates	$868\,\mathrm{MHz}$	$2.4\,\mathrm{GHz}$	$5.0\,\mathrm{GHz}$
R_max $(\mathrm{kbit/s})$, no local oscillator	0.15	0.29	0.29
R_max $(\mathrm{kbit/s})$, with local oscillator	913	1315	360
MISO data rates	$868\,\mathrm{MHz}$	$2.4\,\mathrm{MHz}$	$5.0\,\mathrm{GHz}$
R_max $(\mathrm{kbit/s})$, no local oscillator	138	277	277
R_max $(\mathrm{Mbit/s})$, with local oscillator	9.79	18.35	14.13

After analyzing the data rates of SISO backscatter communication systems and the parameter involved, we move a step further and consider a MISO system. That is, we consider a setup

Table 4.4: Overview of backscatter communication in different technologies.

Signal source	**Reference**	**Range** (m)	**Carrier strength** (dBm)	**Bit rate** (kbit/s)	**Tag power cons.** (µW)
WiFi	Passive WiFi [27]	31	30	1000/110 000	14.5/59.2
	HitchHike [58]	54	30	222	33
LoRa	LoRea [54]	3400	28	2.9	70
	PloRa [38]	300	21	6.3	220
BLE	BLE backscatter [13]	30	23	1000	623
Ambient FM	FM backscatter [55]	1.5	up to 70	3.2	11.1

closely related to what is depicted in Figure 4.5. This is done with the initial access challenge kept in mind and the procedure introduced in Section 4.1.2: A transmitting array illuminates the EN device, possibly through geometry-based[6] beamforming, and thereby exploiting some array gain $G_{\text{array}} = 30\,\text{dB}$. In this procedure, the receiving RW element or array may be trying to pick up signals from devices located at arbitrary positions and therefore no array gain is exploited on the receiving side (therefore the term *MISO system*). This MISO configuration benefits from two advantages regarding the backscatter uplink: The first advantage can be found in the Shannon theory when using point-to-point MISO, where equation 4.6 can be rewritten as:

$$R_{\max} \leq B \cdot \log_2 \left(1 + \frac{L_{\text{t}}\, P_{\text{t}}\, \Delta\sigma\, \frac{\lambda^2\, G_{\text{t}}\, G_{\text{r}}}{(4\pi)^3\, d_1^2\, d_2^2}}{N} \right) . \tag{4.24}$$

This means that the data rate will be further improved with an increasing number of RW elements $L_{\text{t}} \approx G_{\text{array}}$. The second advantage can be found at the mobile nodes. Since the physically large arrays can focus the power at the EN device, a small amount of this transmitted power would be captured by the receiving RW element (or array), away from this large transmitting array. For this reason, (4.24) can be used to calculate the maximum data rate, whilst eliminating the power hungry local oscillator at the EN device. In the lower half of Table 4.3, the achievable data rates are computed for such MISO systems operating at different frequencies and for the parameters given in Table 4.2. It must be noted that the gains made by employing the discussed MISO system do not yet leverage the full potential of the RW infrastructure. On the receiving side, there can also be an array gain leveraged after a possible initial access phase. This will again drastically boost the achievable data rates.

[6] In contrast to reciprocity-based beamforming, since measured CSI may not be available in the initial access phase.

Chapter 5

Hardware requirements of EN devices

In this chapter the hardware requirements for EN devices operated through the RadioWeaves infrastructure are discussed. During the evolution of this project, we have identified the need of device classes because we think that some of the given requirements related to the use-case objectives are rather heterogeneous, so one single solution might not be efficient in terms of hardware complexity, power consumption and overall system costs. For further details on the device classes[1], please refer to REINDEER deliverable D1.1 [14, p. 32] or Section 4.2.1.

5.1 Hardware architecture choices

Related to the device classes, the initial access to the EN device is a crucial aspect for the entire system design. A very basic requirement illustrates this: Imagine a Class 1 EN device, or even a higher-class[2] device, ran out of power and there is a need to communicate with this device remotely. In this scenario, the infrastructure needs to identify and localize the device in order to start inquiry, (i.e., trigger the transmission by a transponder) beamforming and charging. It is obvious that any device to be charged solely by the RadioWeaves infrastructure is required to support the basic class, Class 1. In Section 4.1.2 we have demonstrated a method for solving the initial access problem based on an exemplary front-end sensitivity of $P_{\mathrm{r,min}} = -23\,\mathrm{dBm}$ (a typical value for a Class 1 EN device front-end).

Another aspect is the resolution of a plurality of EN devices located in a dense application scenario. Therefore, specific methods are necessary to separate one after the other sequentially to guarantee the intended communication with a specific EN device. Class 1 supportive devices need to be powered while communicating to maintain continuous operation and data transmission. Furthermore, the current consumption of the communication unit must be extremely low to reach good inquiry coverage of several meters between the EN device and the RadioWeaves infrastructure. That means that a low complexity demodulator circuit is required. The basic one, as we think, is an amplitude modulation (AM) demodulator and communication is achieved by AM of the power or another auxiliary carrier instantaneously. In case of an auxiliary carrier approach, it needs to be ensured that the power carrier does not interfere with the auxiliary carrier, avoiding confusion of the EN device demodulator or decoding circuit.

[1] The device classes range from Class 1 (no explicit energy storage, backscatter communication) to Class 5 (mains-powered, substantial communication capabilities).

[2] EN devices may typically cover device classes 1-3 (see [14, Section 3.1]).

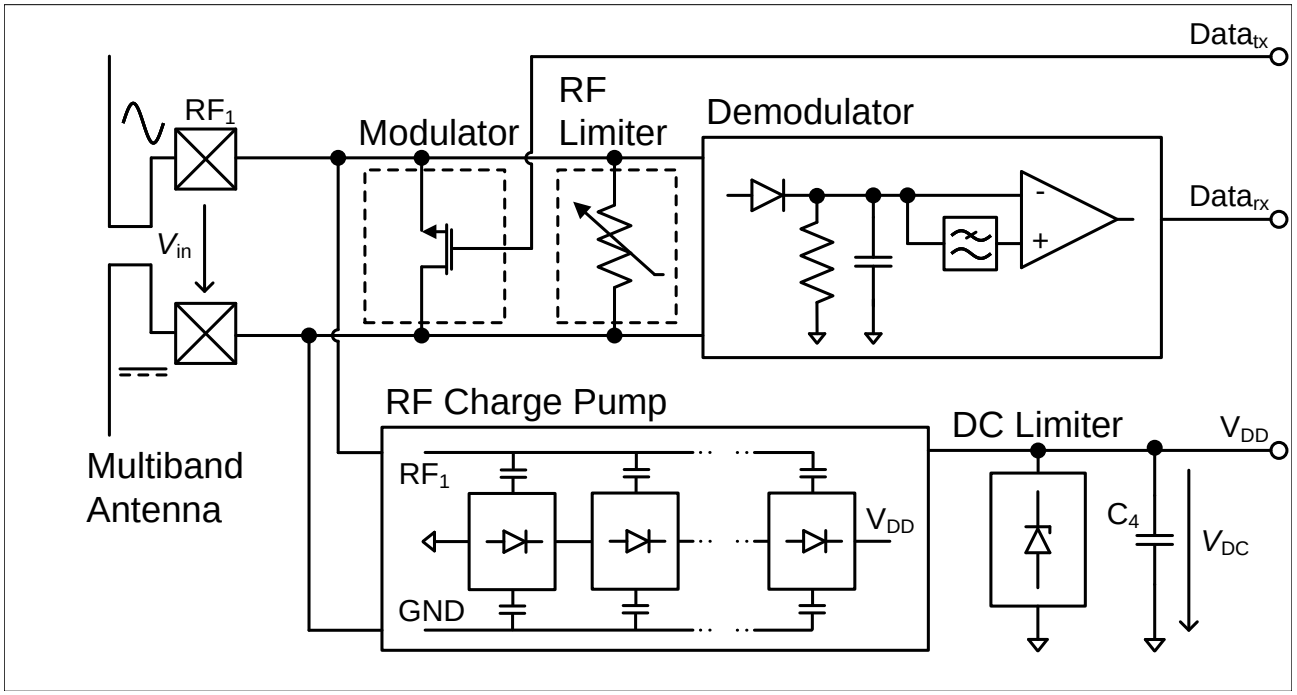

Figure 5.1: Basic architecture of a broad band EN device Class 1.

As a consequence, hardware designs targeting Class 1 support, are the most challenging ones, because they require a very detailed study on ultra-low power hardware building blocks able to be integrated on an integrated circuit (IC). In general, there are two options feasible coming with complementary pros and cons.

The first option comprises one singe RF front-end combining all functions. The fundamental architecture associated with it is illustrated in Figure 5.1. It comprises a multiband antenna directly matched to the RF input terminal and electrostatic discharge (ESD) diodes to protect these inputs. A modulator transistor is used to realize efficient backscatter modulation. An RF limiter is used to keep the input signals in range. A low complexity AM demodulator is used to decode the incoming bit stream. The RF charge pump forms the energy harvesting circuit, its output voltage is passed across a DC limiting device, and finally capacitor C_4 is used to store the collected energy. This architecture has the advantage that it requires only one single antenna, which saves space and production costs.
Unfortunately, the design complexity needs to be well balanced between harvesting and the communication/positioning performance and the use-case diversities. This means, for instance, the broader the definition of the harvesting frequency range, the communication bandwidth and datarates are, the higher the requirements on the antenna design, charge pump, and modulator will be.

Another alternative is illustrated in Figure 5.2. It is much more flexible on the design but comes with higher chip size and production costs as well as larger transponders. The main advantage is that the design criteria can be tackled independently from each other. This means that every single harvesting path has its individual antenna and matching solution resulting in an overall better harvesting efficiency. Furthermore, the communication path is separated from the energy harvesting paths. This enables out-of-band communication without AM carrier modulation and consequently the SNR in (4.17) can be increased. Furthermore, wideband (WB) or even UWB antenna designs are feasible to support precise localization [3] with this approach.

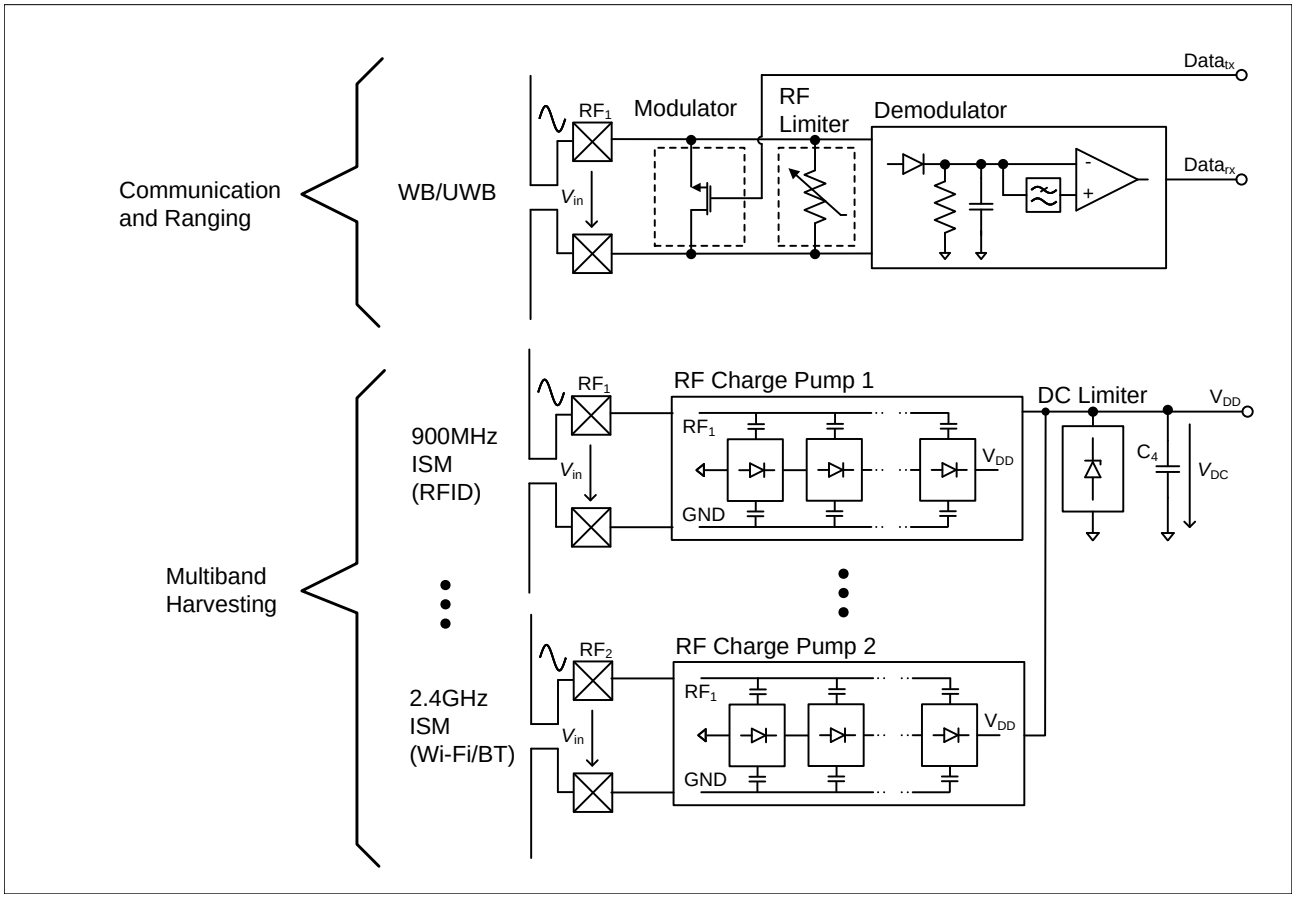

Figure 5.2: Basic architecture of a multi-band EN device Class 1.

As a conclusion, the choice which flavor to use (a single or multiple-antenna variant) depends heavily on the EN device form factor. In case of an ultra-low-cost solution, the single-antenna variant will be chosen, normally with only one single harvesting frequency supported in case the energy harvesting capabilities originated by a low ambient RF energy coverage is low, for instance, item level tagging applications. Single-antenna multi-band harvesting solutions get attractive when there is room for efficiency losses, tolerated by the application use-case. This might also be favorable for a Class 1 supporting higher class device, where this mode is only necessary to inform the RadioWeaves infrastructure that the device ran out of power and needs to be charged. Since the energy demand of such devices is generally high, shorter distances to the RadioWeave antennas may be necessary which goes hand-in-hand with an acceptable efficiency loss of the Class 1 auxiliary circuit.

Multi-antenna multi-band harvesting solutions get attractive for use-cases requiring high localization accuracy, multi-band communication and medium to higher power demanding applications, for instance in ad-hoc networks. Usually, a hybrid Class 1 or Class 2 type of EN device.

5.2 Power harvesting efficiency evaluation

In this section, we outline required and realistic efficiency numbers in relation to RF power transfer of EN devices based on simulation and measurement data. We further describe requirements on these aspects for EN devices operating efficiently in the RadioWeaves infrastructure.

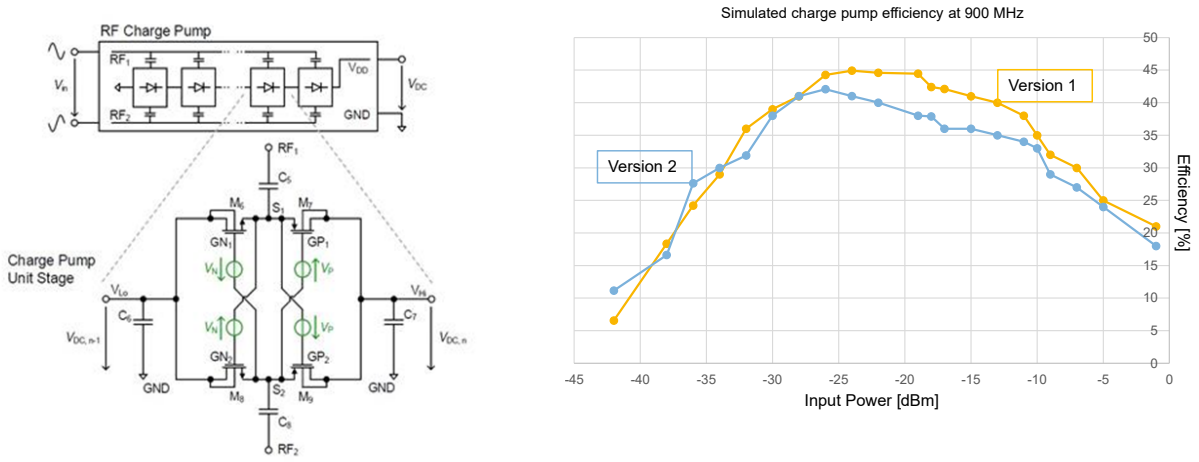

(a) Charge pump design.

(b) Simulation data of two IC versions.

Figure 5.3: Charge pump design and simulation: A charge pump design from NXP Semiconductors has been designed and simulated in Cadence® at an operating frequency of $900\,\mathrm{MHz}$.

We start with simulations related to the core module of the analog front end (AFE). It is the rectifier, or more especially, the charge pump. Because the charge-pump is the key building-block on the EN device defining the main contributor to the power harvesting efficiency. In Figure 5.3 (a) we show the basic structure of an RF charge pump. It consists of a chain of individual rectifiers sitting in parallel. In order to have a high efficiency in a CMOS process, the rectifiers are built with metal-oxide semiconductor field effect transistors (MOSFETs), instead of generic diodes. In Figure 5.3 (b) we show the simulated power conversion efficiency versus input power evaluated on two different IC versions. Usually, a charge pump is designed to exhibit its maximum efficiency when operated at the targeted minimum input power level, i.e., its sensitivity, where it can fully operate. State-of-the-art circuitries operating at $900\,\mathrm{MHz}$ have a sensitivity limit of around $-25\,\mathrm{dBm} \leq P_{\mathrm{in}}^{\mathrm{sen}} \leq -23\,\mathrm{dBm}$. In this range, we see that simulations of modern semiconductor technologies result in a maximum efficiency of $45\,\%$ is achievable at $900\,\mathrm{MHz}$. This target number should be the same when an operation at $2.45\,\mathrm{GHz}$ is considered. However, this does not account for leakage effects or other losses on the signal distribution layers inside the IC with respect to higher operating frequencies. Thus, it is expected that the actual efficiency will be less and that with higher frequency, the overall efficiency is getting worse. However, these $45\,\%$ should be taken as a design target of a EN device supporting reasonable RF harvesting functionality.

To demonstrate the harvesting capabilities and to assess the actual efficiency numbers including matching losses, we have conducted wired and wireless measurements. These results are also a good basis to support the theoretical investigations in relation to the RadioWeave power downlink efficiency outlined in the previous chapter. Based on the wired measurement setup depicted in Figure 5.4, we have connected a VNA to the EN device fixture through a $30\,\mathrm{cm}$ long cable (with a characteristic impedance of $50\,\Omega$) and matched the system to $50\,\Omega$ on its terminals. In addition, the Tx is connected to a spectrum analyzer, used to visualize and to analyze the measurement data.

The EN device fixture consists of a Balun used to balance between the single-ended VNA signal incident to the fixture and the differential signal input, the charge pump has been designed for. The output of the Balun is connected to a matching network (MN). The MN is defined in a way, that it matches the charge pump impedance to the Balun at a specific frequency to gain good

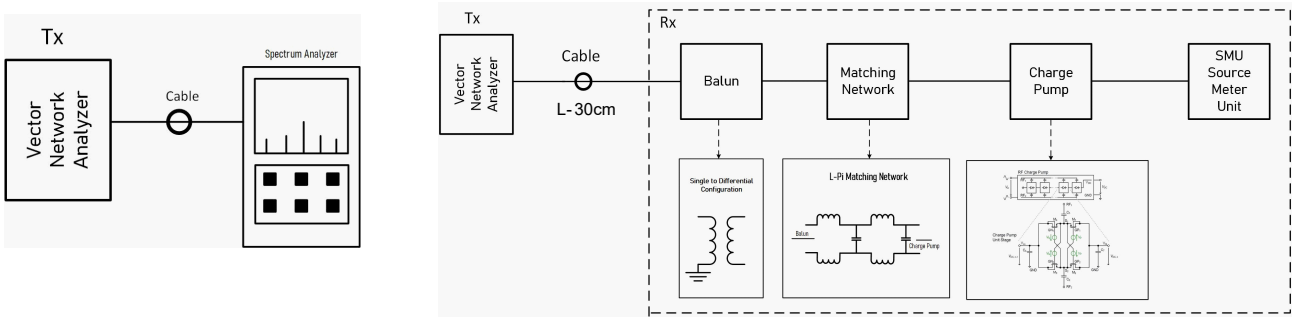

Figure 5.4: Wired energy harvesting measurement setup.

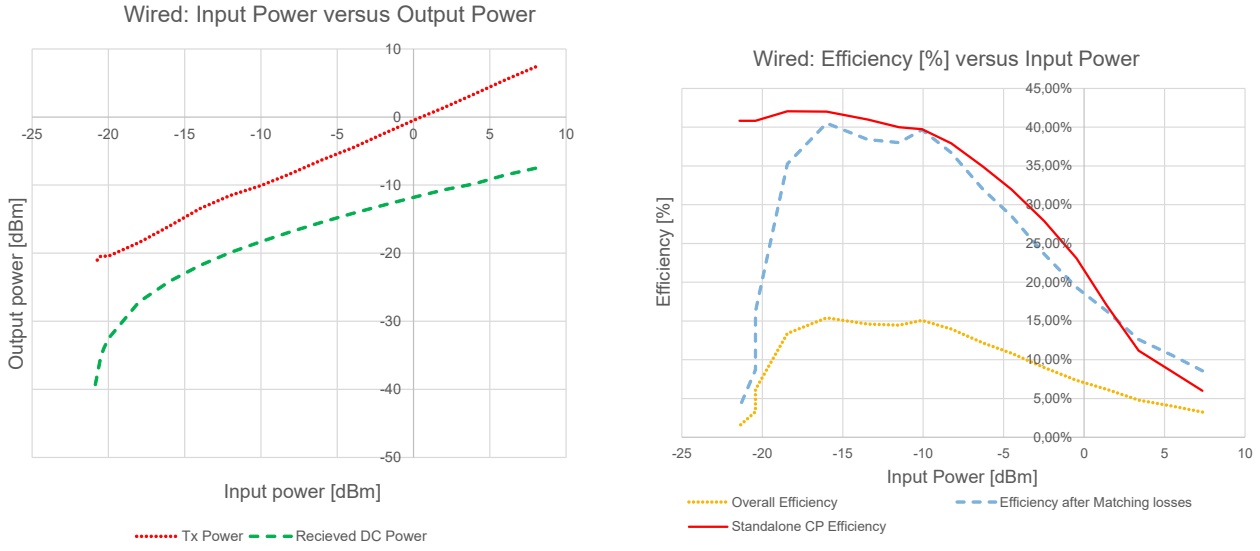

(a) Power input/output loss.

(b) Charge-pump efficiency.

Figure 5.5: Wired measurement results at $900\,\mathrm{MHz}$.

power transfer across the entire chain. The output of the charge pump is connected to a source meter used to measure the instant power transfer.

In order to have a reference baseline, we have extracted the individual efficiency numbers from a $900\,\mathrm{MHz}$ based measurement series. These results are illustrated in Figure 5.5. From Figure 5.5 (a), we can see the power input to output relation, where the input is the RF Tx power from the VNA and the output is the DC power at the charge-pump output. The transfer loss is about $10\,\mathrm{dB}$ to $12\,\mathrm{dB}$ in the range from $-15\,\mathrm{dBm}$ to $0\,\mathrm{dBm}$ input power. Consequently, this results in an overall efficiency of about $15\,\%$ (including an additional cable loss of $4\,\mathrm{dB}$). A break down to the individual efficiency contributors is illustrated in Figure 5.5 (b). By deducing all these losses, we could prove that the standalone charge pump efficiency extracted from the Cadence® circuit simulations matches the measurements in this region. By comparing $40\,\%$ (charge pump only) against $15\,\%$ (overall), roughly $38\,\%$ of efficiency is lost in the Balun and matching network. Thus, it comes out clearly, that in case a highly efficient harvesting EN device is intended, a dedicated matching network needs to be avoided. However, we still see (since the fixture, i.e., Balun and Matching Network, are linear) that the trend of the simulated CP (nonlinear) efficiency is well visible in the measurement results.

By investigating the same scenario at $2.4\,\mathrm{GHz}$ the results look a bit different as illustrated in

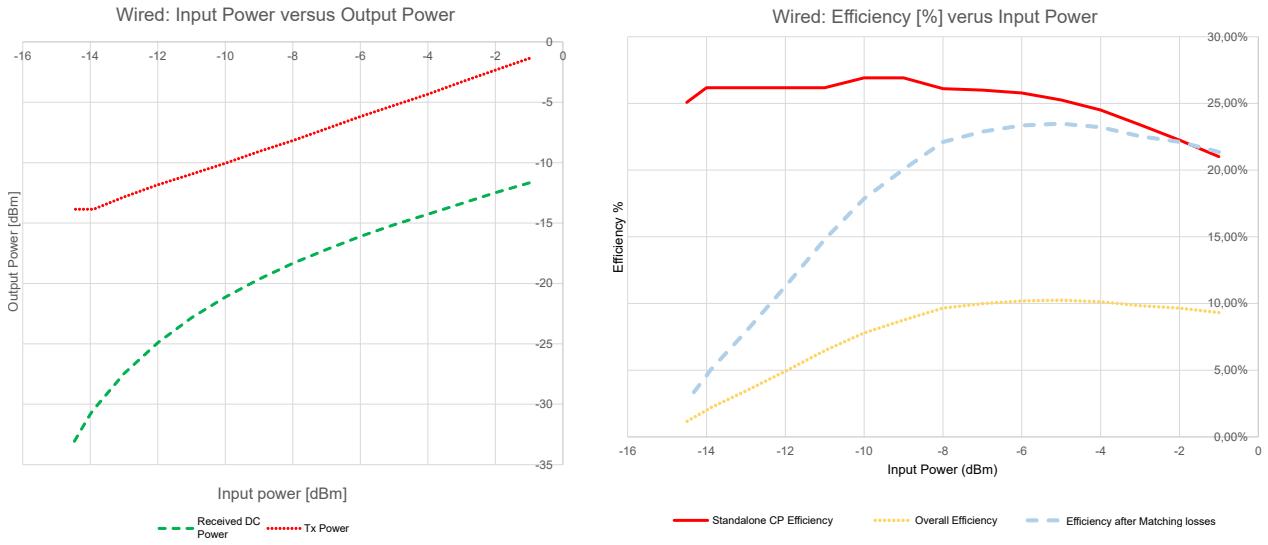

(a) Power input/output loss.

(b) Charge-pump efficiency.

Figure 5.6: Wired measurement results at $2.4\,\mathrm{GHz}$.

Table 5.1: Actual power harvested in dBm versus distance and frequency around $2.4\,\mathrm{GHz}$.

d	**Operating frequency in** GHz								
	2.34	2.38	2.40	2.44	2.48	2.50	2.54	2.58	2.60
	Output power in dBm								
$50\,\mathrm{cm}$	-14.41	-12.27	-17.75	-21.26	-18.89	-15.83	-14.87	-16.04	-14.08
$80\,\mathrm{cm}$	-20.27	-19.50	-22.20	-18.47	-24.53	-20.01	-21.08	-19.50	-19.80

Figure 5.6. The overall efficiency drops down to $10\,\%$ compared to $15\,\%$ at $900\,\mathrm{MHz}$. What we have also seen is that the simulation results of the charge pump differ from the compensated measurement results as illustrated in Figure 5.6 (b). More precisely, when the power levels are high, e.g., around $0\,\mathrm{dBm}$, we obtain a good match. But, in the lower input power regions, there is a strong deviation between simulation and measurement. Most likely, the theoretical efficiency extracted from the circuit simulator is too optimistic for this frequency area of operation.

Finally, we are interested in the actual EN device use-case, which involves wireless harvesting within a specific range from the transmitting RadioWeaves. We want to understand what is the maximum range at which the successful power transfer and operation of an EN device can be achieved. Therefore, we have set up a measurement fixture illustrated in Figure 5.7.

The measurement setup consists of a VNA producing the Tx power incident to the Tx antenna. The evaluation board is placed at a variable distance between $0.5\,\mathrm{m}$ and $1.5\,\mathrm{m}$ to test the harvesting capabilities at $2.4\,\mathrm{GHz}$. The evaluation board was fabricated with a matching network designed for $2.4\,\mathrm{GHz}$ only. The Tx power was set to $20\,\mathrm{dBm}$, and the antenna gain was $-5\,\mathrm{dBi}$. Table 5.1 shows the received DC power measured at the charge pump output with the source meter.

From these measurement results it would be possible to harvest reasonable power out of an RF communication device operating in the $2.4\,\mathrm{GHz}$ frequency range operating an electronic circuity. In other words, a standard Wi-Fi access point ($P_\mathrm{t} = 20\,\mathrm{dBm}$, $G_\mathrm{t} = -5\,\mathrm{dBi}$) would be able to

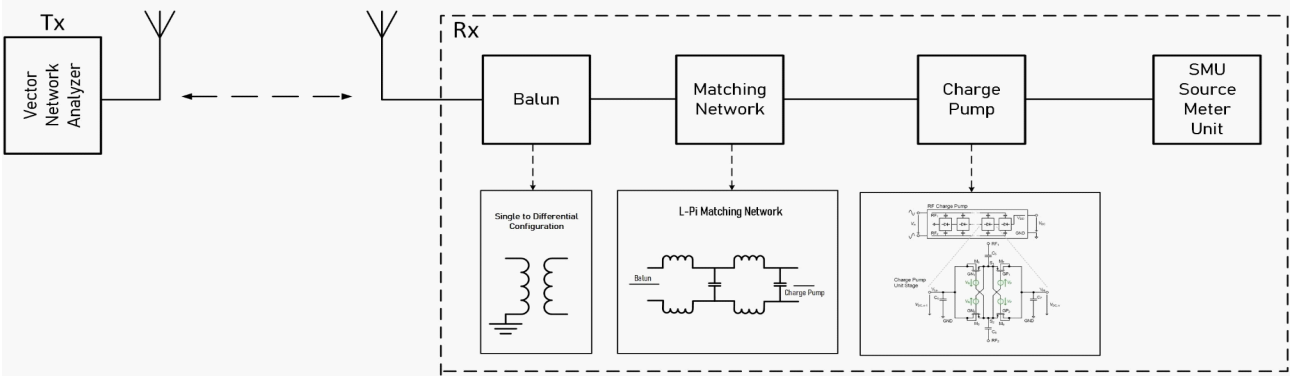

(a) Wireless energy harvesting measurement setup.

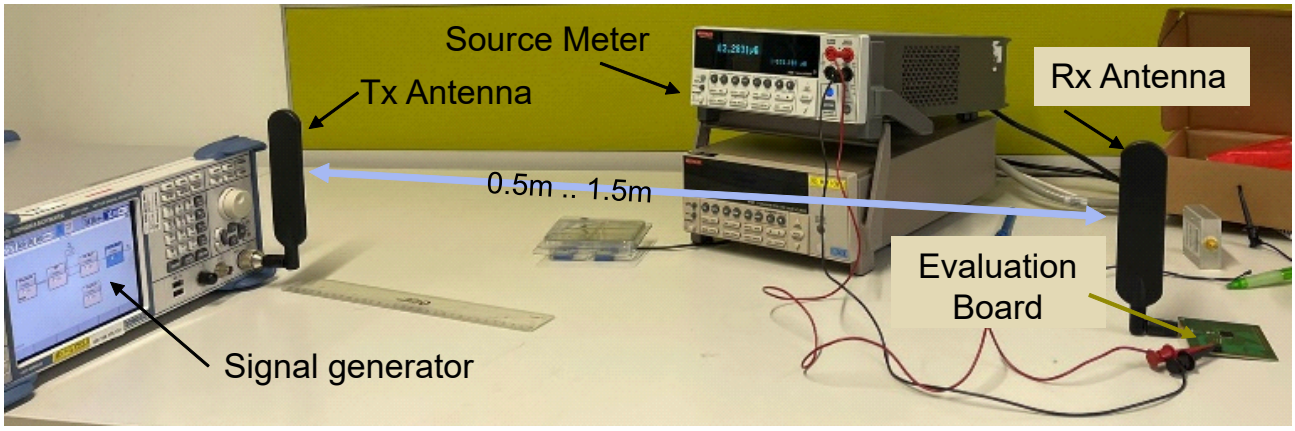

(b) Picture of the measurement setup.

Figure 5.7: Wireless measurement setup at $2.4\,\mathrm{GHz}$.

operate an EN device up to roughly $1\,\mathrm{m}$ distance, from the RF powering point of view, if only a single transmit antenna was used. As we have demonstrated, according to (4.5) on page 33, this distance can be enlarged by orders of magnitude by coherently supplying the device with power from multiple transmit antennas simultaneously.

To operate a EN device within the RadioWeaves infrastructure, several aspects in terms of WPT need to be considered. First, the achievable power harvesting efficiency of the core element, the charge-pump, should be high, where we report a maximum of around $45\,\%$. Which is $5\,\%$ off the theoretical limit of $50\,\%$. This is due to the fact that even in a perfectly matched RF system, only half the power can be transferred to the load [37, Ch. 13]. In case of the presence of a dedicated matching network consisting of conductors and inductors, about $40\,\%$ additional loss needs to be considered, which means that the overall efficiency drops from $40\,\%$ down to around $18\,\%$ to $20\,\%$ efficiency in this specific example. Usually, 3dB power loss can be given as a typical number because of the typical highly frequency dependent charge pump impedance.

Considering a DC-DC converter connected after the charge pump, additional losses need to be considered. Usually DC-DC converters (integrated designs) provide an efficiency greater than $85\,\%$, and can be seen as a minor contributor to the overall efficiency degradation. Out of the measurement series we see, that it would be possible to harvest sufficient power from a SISO communication system, still the range will be short and the available power for processing will be low (in the $10\,\mu\mathrm{W}$ region). However, in case the output power can be increased on one side and the pathloss can be reduced by employing a MISO system, harvesting several mW would be possible, as a target to reach with the RadioWeaves infrastructure as our measurement results in Section 2.3 and simulation results in Section 4.1.1 have shown.

5.3 Optimal antenna design

We also want to highlight the need of an optimized antenna design for achieving an efficient EN device architecture. From the measurements we have seen that about $40\,\%$ of efficiency are lost in a dedicated lumped element matching circuit. This is originating to a large extend from the fact that the capacitors and inductors (as well as the Balun) do have parasitic resistors. To avoid a physical matching network, the antenna needs to be directly matched to the input impedance of the harvesting IC [40], if possible. Another aspect to be taken into consideration is detuning subject to environmental changes. This can happen, for instance, if the EN device is worn in close proximity to the human body, for example by putting it into the trousers' back-pocket. This means that the antenna matching is a compromise between bandwidth and achievable peak efficiency at the resonance frequency. The matching process is described in accordance with Figure 5.8. First, we want to start with explaining the different parameters. R_antenna and X_antenna form the frequency dependent antenna impedance. R_input_ic and X_input_ic form the frequency dependent IC input impedance, where R_input_ic is constant across the frequency of interest. Here the antenna is defined in a way that it provides about $100\,\mathrm{MHz}$ bandwidth to cope with detuning effects and addresses the feasibility of different carrier frequencies at which the EN device is operating. On the other hand, it needs to be ensured that the antenna matches the conjugate complex of the input impedance of the EN device IC, as discussed in Section 2.1.2. These design criteria are usually optimized by means of a finite element analysis (FEM) antenna solver.

Figure 5.9 shows the application of the optimal antenna matching procedure. This prototype was fabricated for $2.4\,\mathrm{GHz}$, where the antenna is directly connected to the IC. In Figure 5.9 (b), the read range versus Tx power and frequency is illustrated. The read range corresponds to

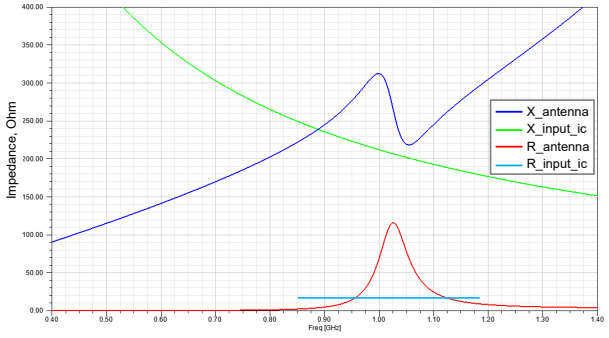

(a) Impedance versus frequency.

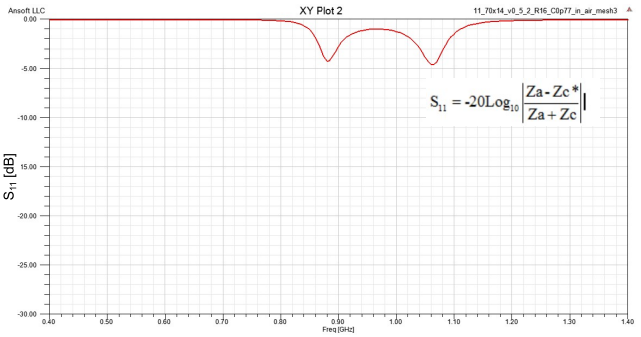

(b) Reflection coefficient S_{11}.

Figure 5.8: Proposed antenna matching strategy to avoid physical lumped-element matching networks: Simulations of impedance and reflection coefficients of the EN device harvesting unit consisting of an antenna and charge-pump.

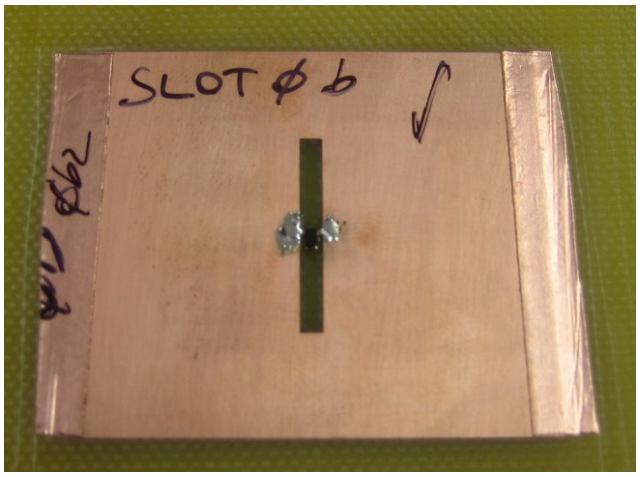

(a) Prototype.

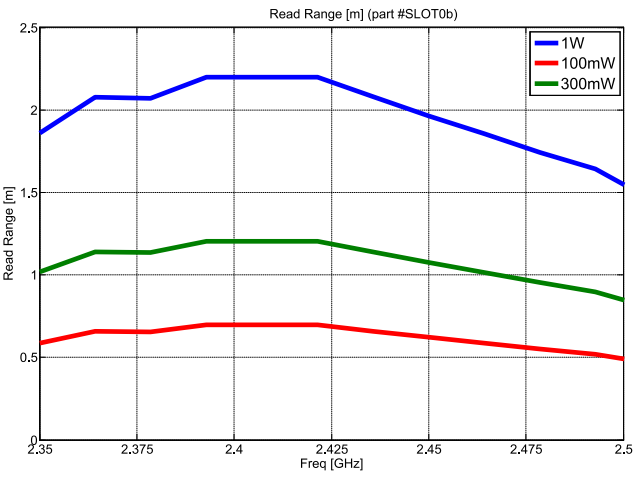

(b) Power harvesting threshold at $-14\,\mathrm{dBm}$.

Figure 5.9: Exemplary prototype of a $2.4\,\mathrm{GHz}$ EN device without dedicated matching network and measurements of the device read range.

the distance at which a receive power $P_\mathrm{r} = -14\,\mathrm{dBm}$ available at the input terminals, when operating a SISO system at the indicated transmit powers P_t. These results correspond well with the measurements performed previously.

Chapter 6

Summary

The interaction with EN devices is a fundamental feature of a RadioWeaves infrastructure. Various future use cases will build on the use of energy-efficient, sustainable, and cost-effective EN devices deployed at massive scale. To unleash these unprecedented capabilities of RadioWeaves, the predicted achievable gains need to be verified both by means of analytical computations and real-life measurements.

In this document, we have investigated the building blocks of state-of-the-art RF WPT systems in Section 2.1 and identified that significant gains can be made in the RF-to-RF transmission. Substantial work has been done with respect to channel modeling in Section 2.2. Particular emphasis has been put on the physically correct modeling of power wave amplitudes, such that the WPT efficiency is accurately represented. Our novel geometry-based channel model is formulated in terms of S-parameters which makes it directly comparable with VNA measurements. Combining expertise from both the fields of RF measurement and signal processing, we are able to accurately model RF WPT. We conducted synthetic aperture measurements in Section 2.3 that validate the physical correctness of our WPT channel model. We demonstrated that multipath propagation, i.e., a simultaneous multibeam transmission, can be exploited to increase the WPT power budget over what is achievable using a LoS beam only. Furthermore, we have shown that the prediction of channel vectors is possible using a geometric environment model with environment information only and without having measured CSI available, which is an enabling milestone for the initial access to EN devices, and resilient communication and WPT with moving devices. In the future we will demonstrate the prediction of channel vectors using both the LoS and MPC beams. Our discussion in Section 3.1 encompasses regulatory compliance of conventional existing WPT systems and the compliance of future distributed, or physically large radio infrastructures. We demonstrated that spherical wavefront beamforming in the array near-field is very beneficial for compliance with power density limits but also with EIRP limits. The important compliance benefits of distributed radio infrastructures and lacking distinction from conventional (e.g., SISO, or concentrated/centralized radio architectures) systems may necessitate an adaptation of regulations. Based on power density compliance limits, we derived the maximum regulatory-compliant power budgets of EN devices operating with a constant gain antenna or a constant aperture antenna at various frequencies. In Section 4.1 these power budgets were first derived and then used to compute the achievable initial access distance of an exemplary RadioWeaves deployment. A possible scheme for solving the initial access problem to EN devices has been proposed. Exploiting beam diversity, we were able to reduce the necessary fading margin and extend the initial access distance. Backscatter communication enables communication

with ultra-low power EN devices. Its operating principle and implications on transponder antenna design and load modulation were discussed in Section 4.2. Possible transponder architectures are presented in Section 5. Selected designs were analyzed by means of circuit-level simulations and VNA measurements. Both the charge pump, due to its limited achievable efficiency, as well as the matching network, due to the strongly nonlinear transponder chip impedance, have been identified as key components impacting the overall WPT system efficiency. To overcome the impairments imposed by matching losses, a design procedure has been proposed that aims to match the transponder antenna directly to the chip.

This document reveals the potential of a RadioWeaves infrastructure when interacting with EN devices. Some of the fundamental performance limits (e.g., maximum regulatory-compliant power budgets, achievable initial access distance, etc.) have been derived. Together with the system-level model, they outline the capabilities of future distributed radio architectures in terms of RF WPT and efficient backscatter communication. We provided tools for the evaluation of achievable performance, and in particular an accurate channel model for a physically accurate representation of the RF-to-RF transmission of power. Verified through realistic synthetic aperture measurements, the channel model constitutes the foundation for subsequent algorithmic developments for the efficient and resilient interaction with EN devices that a RadioWeaves infrastructure allows. These algorithms will be published in the REINDEER deliverable D4.2 [43], and will have a strong connection to algorithms for position estimation and environment learning that will be derived in deliverable D3.3 [42], since many of the achievable gains of RadioWeaves rely on its geometric environment-awareness.

Appendix A

Derivations

A.1 Linear-circular polarization gain

Let $\boldsymbol{\rho}_\mathrm{r}$ denote the polarization vector of a circularly polarized receiving antenna and $\boldsymbol{\rho}_\mathrm{t}$ the polarization vector of a linearly polarized incident wave. The incident wave propagates in a direction $\boldsymbol{e}_S$, thus its polarization vector is located in a plane orthogonal to the direction of propagation. Let $\boldsymbol{e}_\theta$ and $\boldsymbol{e}_\varphi$ denote orthogonal unit-vectors in that plane, then the linearly polarized incident wave may have a polarization vector oriented at some arbitrary angle α within the plane:

$$\boldsymbol{\rho}_\mathrm{t} = \boldsymbol{e}_\theta \, \cos\alpha + \boldsymbol{e}_\varphi \, \sin\alpha = \begin{bmatrix} \cos\alpha \\ \sin\alpha \end{bmatrix} . \tag{A.1}$$

The circularly polarized receiving antenna has a complex-valued polarization vector of the form [4]

$$\boldsymbol{\rho}_\mathrm{r} = \boldsymbol{e}_\theta \, \frac{1}{\sqrt{2}} \pm j \, \boldsymbol{e}_\varphi \, \frac{1}{\sqrt{2}} = \begin{bmatrix} \frac{1}{\sqrt{2}} \\ \pm j \frac{1}{\sqrt{2}} \end{bmatrix} \tag{A.2}$$

where both real and imaginary components are aligned with $\boldsymbol{e}_\theta$ and $\boldsymbol{e}_\varphi$ for brevity. The exact orientation is irrelevant for this derivation, however, since any alignment mismatch is modeled using the angle α. Both real and imaginary components need to be equal in magnitude to represent circular polarization [4]. The polarization gain (in terms of amplitude) is

$$\left| \boldsymbol{\rho}_\mathrm{t}^\mathsf{T} \boldsymbol{\rho}_\mathrm{r} \right| = \left| \begin{bmatrix} \cos\alpha & \sin\alpha \end{bmatrix} \begin{bmatrix} \frac{1}{\sqrt{2}} \\ \pm j \frac{1}{\sqrt{2}} \end{bmatrix} \right| = \tag{A.3}$$

$$\frac{1}{\sqrt{2}} \left| (\cos\alpha \pm j \, \sin\alpha) \right| = \frac{1}{\sqrt{2}} = -3\,\mathrm{dB}, \tag{A.4}$$

regardless of the orientation angle α.

A.2 Polarization rotation matrix

A linearly polarized wave with polarization vector

$$\boldsymbol{\rho}_{\mathrm{t}} = \boldsymbol{e}_{\theta}\,\rho_{\theta} + \boldsymbol{e}_{\varphi}\,\rho_{\varphi} = \begin{bmatrix}\rho_{\theta}\\ \rho_{\varphi}\end{bmatrix} \tag{A.5}$$

incident to a surface may undergo a polarization rotation due to its reflection at the surface. The rotation is modeled by a rotation matrix

$$\boldsymbol{R} = \begin{bmatrix}\cos\alpha & -\sin\alpha\\ \sin\alpha & \cos\alpha\end{bmatrix} \tag{A.6}$$

where α is the incurring counterclockwise rotation angle, rotating the polarization in the (θ, φ)-plane orthogonal to the direction of propagation $\boldsymbol{e}_S$. The polarization vector of the reflected wave is thus

$$\widetilde{\boldsymbol{\rho}}_{\mathrm{t}} = \boldsymbol{R}\,\boldsymbol{\rho}_{\mathrm{t}} = \begin{bmatrix}\rho_{\theta}\,\cos\alpha - \rho_{\varphi}\,\sin\alpha\\ \rho_{\theta}\,\sin\alpha + \rho_{\varphi}\,\cos\alpha\end{bmatrix}\,. \tag{A.7}$$

Bibliography

[1] Panos N Alevizos and Aggelos Bletsas. Sensitive and nonlinear far-field RF energy harvesting in wireless communications. *IEEE Transactions on Wireless Communications*, 17(6):3670–3685, 2018.

[2] Panos N Alevizos, Georgios Vougioukas, and Aggelos Bletsas. Nonlinear energy harvesting models in wireless information and power transfer. In *2018 IEEE 19th International Workshop on Signal Processing Advances in Wireless Communications (SPAWC)*. IEEE, 2018.

[3] Daniel Arnitz, Ulrich. Muehlmann, and Klaus Witrisal. UWB ranging in passive UHF RFID: proof of concept. *Electronics Letters*, 46:1401 – 1402, October 2010.

[4] C A Balanis. *Antenna Theory: Analysis and Design*. John Wiley & Sons, Hoboken, NJ, 3 edition, 2005.

[5] A. Bletsas, A. G. Dimitriou, and J. N. Sahalos. Improving backscatter radio tag efficiency. *IEEE Transactions on Microwave Theory and Techniques*, 58(6):1502–1509, 2010.

[6] Gilles Callebaut, Liesbet Van der Perre, François Rottenberg, Jianan Bai, Unnikrishnan Kunnath Ganesan, Sai Subramanyam Thoota, Erik G. Larsson, Emma Fitzgerald, Liang Liu, Jesus Rodriguez Sanches, Pål Frenger, Andres Reial, Benjamin J. B. Deutschmann, Thomas Wilding, and Klaus Witrisal. Methods for communication and initial access with RadioWeaves. Deliverable ICT-52-2020 / D3.2, REINDEER project, 2022.

[7] Mustafa Cansiz, Dogay Altinel, and Gunes Karabulut Kurt. Efficiency in RF energy harvesting systems: A comprehensive review. *Energy*, 174:292–309, 2019.

[8] Jorge R. Costa, Carla R. Medeiros, and Carlos A. Fernandes. Performance of a crossed exponentially tapered slot antenna for UWB systems. *IEEE Transactions on Antennas and Propagation*, 57(5):1345–1352, May 2009.

[9] Bert Cox. *Hybrid RF-acoustic Ranging for Energy Efficient Indoor Positioning*. Doctoral thesis, KU Leuven, 2022.

[10] Benjamin J. B. Deutschmann, Thomas Wilding, Erik G. Larsson, and Klaus Witrisal. Location-based initial access for wireless power transfer with physically large arrays. In *WS08 IEEE ICC 2022 Workshop on Synergies of communication, localization, and sensing towards 6G (WS08 ICC'22 Workshop - ComLS-6G)*, Seoul, Korea (South), May 2022.

[11] Ove Edfors, Romulo Brazil, Herbert Petautschnig, Gilles Callebaut, Thomas Feys, Liesbet Van der Perre, Erik G. Larsson, Ove Edfors, Emma Fitzgerald, Liang Liu, Jesus Rodriguez Sanchez, William Tärneberg, Pal Frenger, Benjamin Deutschmann, Thomas Wilding, and Klaus Witrisal. Radioweaves high-level architecture and processing distribution strategies. Deliverable ICT-52-2020 / D2.1, REINDEER project, January 2022.

[12] Joshua F. Ensworth and Matthew S. Reynolds. Every smart phone is a backscatter reader: Modulated backscatter compatibility with bluetooth 4.0 low energy (BLE) devices. In *IEEE International Conference on RFID*, pages 78–85, 2015.

[13] Joshua F. Ensworth and Matthew S. Reynolds. Ble-backscatter: Ultralow-power IoT nodes compatible with bluetooth 4.0 low energy (BLE) smartphones and tablets. *IEEE Transactions on Microwave Theory and Techniques*, 65(9):3360–3368, 2017.

[14] Juan Francisco Esteban, Martina Truskaller, Luana Fabrete, Alexandra Stanek, Daan Delabie, Liesbet Van der Perre, Erik G. Larsson, Sarvendranath Rimalapudi, Emma Fitzgerald, Fredrik Tufvesson, Ove Edfors, Andres Reial, Benjamin Deutschmann, Klaus Witrisal, Thomas Wilding, Ivo Vandeweerd, Marcus Borrmann, Ulrich Mühlmann, and Juan Francisco Esteban. Use case-driven specifications and technical requirements and initial channel model. Deliverable ICT-52-2020 / D1.1, REINDEER project, September 2021.

[15] European Council. 1999/519/EC: Council recommendation of 12 July 1999 on the limitation of exposure of the general public to electromagnetic fields (0 Hz to 300 GHz), July 1999.

[16] European Council. 2006-771-EC: Commission decision of 9 November 2006 on harmonisation of the radio spectrum for use by short-range devices, November 2006.

[17] European Council. Commission implementing decision (EU) 2017/1483 of 8 August 2017 amending decision 2006/771/EC on harmonisation of the radio spectrum for use by short-range devices and repealing decision 2006/804/EC, August 2017.

[18] European Council. Commission implementing decision (EU) 2018/1538 of 11 October 2018 on the harmonisation of radio spectrum for use by short-range devices within the 874-876 and 915-921 MHz frequency bands, October 2018.

[19] European Council. Assessment of electronic and electrical equipment related to human exposure restrictions for electromagnetic fields (0 Hz to 300 GHz), December 2020.

[20] European Council. Commission implementing decision (EU) 2022/179 of 8 February 2022 on the harmonised use of radio spectrum in the 5 GHz frequency band for the implementation of wireless access systems including radio local area networks and repealing decision 2005/513/EC, February 2022.

[21] Klaus Finkenzeller. *RFID Handbook: Fundamentals and Applications in Contactless Smart Cards, Radio Frequency Identification and Near-Field Communication*. Wiley & Sons, 3 edition, 2010.

[22] Robert Blair Green. *The general theory of antenna scattering*. PhD thesis, The Ohio State University, 1963.

[23] Xiaoqiang Gu, Simon Hemour, and Ke Wu. Far-field wireless power harvesting: Nonlinear modeling, rectenna design, and emerging applications. *Proceedings of the IEEE*, 2021.

[24] R. C. Hansen. Relationships between antennas as scatterers and as radiators. *Proceedings of the IEEE*, 77(5):659–662, 1989.

[25] Vikram Iyer, Vamsi Talla, Bryce Kellogg, Shyamnath Gollakota, and Joshua Smith. Inter-technology backscatter: Towards internet connectivity for implanted devices. In *Proceedings of the 2016 ACM SIGCOMM Conference*, page 356–369, 2016.

[26] D.H. Johnson and D.E. Dudgeon. *Array Signal Processing: Concepts and Techniques*. Prentice-Hall Series in Signal. Prentice Hall, 1993.

[27] Bryce Kellogg, Vamsi Talla, Shyamnath Gollakota, and Joshua R. Smith. Passive Wi-Fi: Bringing low power to Wi-Fi transmissions. In *13th USENIX Symposium on Networked Systems Design and Implementation*, pages 151–164, March 2016.

[28] Eugene F. Knott, John F. Schaeffer, and T. Michael Tulley. *Radar Cross Section*. SciTech Publishing, USA, 2004.

[29] Josef Kulmer, Fuxi Wen, Nil Garcia, Henk Wymeersch, and Klaus Witrisal. Impact of rough surface scattering on stochastic multipath component models. In *2018 IEEE 29th Annual International Symposium on Personal, Indoor and Mobile Radio Communications (PIMRC)*, pages 1410–1416, 2018.

[30] Ilkka Laakso. *Uncertainty in computational RF dosimetry*. Doctoral thesis, School of Electrical Engineering, 2011.

[31] Triet Le, Karti Mayaram, and Terri Fiez. Efficient far-field radio frequency energy harvesting for passively powered sensor networks. *IEEE Journal of Solid-State Circuits*, 43(5):1287–1302, 2008.

[32] Erik Leitinger, Paul Meissner, Christoph Rudisser, Gregor Dumphart, and Klaus Witrisal. Evaluation of position-related information in multipath components for indoor positioning. 33(11):2313–2328, November 2015.

[33] Zhongtao Liu, Zheng Zhong, and Yong-Xin Guo. Enhanced dual-band ambient RF energy harvesting with ultra-wide power range. *IEEE Microwave and Wireless Components Letters*, 25(9):630–632, 2015.

[34] Andreas F. Molisch. *Wireless Communications*. Wiley Publishing, 2nd edition, 2011.

[35] Daniel Neunteufel, Florian Galler, and Holger Arthaber. Comprehensive measurement of complex-valued delta radar cross-section. In *2018 6th International EURASIP Workshop on RFID Technology (EURFID)*, pages 1–7, 2018.

[36] Pavel Nikitin, K.V.s Rao, and R.D. Martinez. Differential RCS of RFID tag. *Electronics Letters*, 43:431–432, February 2007.

[37] Sophocles J. Orfanidis. *Electromagnetic Waves and Antennas*. Rutgers University, 2016.

[38] Yao Peng, Longfei Shangguan, Yue Hu, Yujie Qian, Xianshang Lin, Xiaojiang Chen, Dingyi Fang, and Kyle Jamieson. Plora: A passive long-range data network from ambient lora transmissions. SIGCOMM '18, page 147–160, 2018.

[39] K. V. S. Rao, P. V. Nikitin, and S. F. Lam. Antenna design for UHF RFID tags: a review and a practical application. *IEEE Transactions on Antennas and Propagation*, 53(12):3870–3876, 2005.

[40] K.V.S. Rao, P.V. Nikitin, and S.F. Lam. Impedance matching concepts in RFID transponder design. In *Fourth IEEE Workshop on Automatic Identification Advanced Technologies (AutoID'05)*, pages 39–42, 2005.

[41] REINDEER project. Hardware requirements to support energy transfer to energy-neutral nodes. Deliverable ICT-52-2020 / D2.3, unpublished (March 2023).

[42] REINDEER project. Position estimation and environment learning. Deliverable ICT-52-2020 / D3.3, unpublished (March 2023).

[43] REINDEER project. Signal processing for WPT and uplink signalling, exploiting environment awareness. Deliverable ICT-52-2020 / D4.2, unpublished (March 2023).

[44] George T. Ruck, Donald E. Barrick, William D. Stuart, and Clarence K. Krichbaum. *Radar cross section handbook*. New York: Plenum Press, 1970.

[45] Martijn Saelens, Jeroen Hoebeke, Adnan Shahid, and Eli De Poorter. Impact of EU duty cycle and transmission power limitations for sub-GHz LPWAN SRDs: an overview and future challenges. *EURASIP Journal on Wireless Communications and Networking*, 2019(1):219, 2019.

[46] Chaoyun Song, Yi Huang, Jiafeng Zhou, Paul Carter, Sheng Yuan, Qian Xu, and Zhouxiang Fei. Matching network elimination in broadband rectennas for high-efficiency wireless power transfer and energy harvesting. *IEEE Transactions on Industrial Electronics*, 64(5):3950–3961, 2016.

[47] Texas Instruments. CC2590 2.4-GHz RF Front End, 14-dBm output power. product data sheet SWRS080, Texas Instruments, September 2008.

[48] Le-Giang Tran, Hyouk-Kyu Cha, and Woo-Tae Park. RF power harvesting: a review on designing methodologies and applications. *Micro and Nano Systems Letters*, 5(1):1–16, 2017.

[49] David Tse and Pramod Viswanath. *Fundamentals of Wireless Communication*. Cambridge University Press, USA, September 2005.

[50] David Tse and Pramod Viswanath. *Fundamentals of wireless communication*. Cambridge University Press, Cambridge, England, June 2012.

[51] Liesbet Van der Perre, Erik G. Larsson, Fredrik Tufvesson, Lieven De Strycker, Emil Björnson, Ove Edfors, Lieven De Strycker, Emil Bjornson, and Ove Edfors. RadioWeaves for efficient connectivity: analysis and impact of constraints in actual deployments. In *2019 53rd Asilomar Conference on Signals, Systems, and Computers*, pages 15–22. IEEE, November 2019.

[52] N. Van Huynh, D. T. Hoang, X. Lu, D. Niyato, P. Wang, and D. I. Kim. Ambient backscatter communications: A contemporary survey. *IEEE Communications Surveys Tutorials*, 20(4):2889–2922, 2018.

[53] H L Van Trees. *Optimum Array Processing: Part IV of Detection, Estimation, and Modulation Theory*. Detection, Estimation, and Modulation Theory. Wiley, 2002.

[54] Ambuj Varshney, Carlos Pérez-Penichet, Christian Rohner, and Thiemo Voigt. Lorea: A backscatter architecture that achieves a long communication range. In *Proceedings of the 15th ACM Conference on Embedded Network Sensor Systems*, 2017.

[55] Anran Wang, Vikram Iyer, Vamsi Talla, Joshua R. Smith, and Shyamnath Gollakota. FM backscatter: Enabling connected cities and smart fabrics. In *Proceedings of the 14th USENIX Conference on Networked Systems Design and Implementation*, page 243–258, 2017.

[56] Po-Han Peter Wang, Chi Zhang, Hongsen Yang, Dinesh Bharadia, and Patrick P. Mercier. A 28 μW IoT tag that can communicate with commodity WiFi transceivers via a single-sideband QPSK backscatter communication technique. In *IEEE International Solid- State Circuits Conference - (ISSCC)*, pages 312–314, 2020.

[57] Di Wu, Yong Zeng, Shi Jin, and Rui Zhang. Environment-aware and training-free beam alignment for mmwave massive MIMO via channel knowledge map. In *2021 IEEE International Conference on Communications Workshops (ICC Workshops)*, pages 1–7. IEEE, June 2021.

[58] Pengyu Zhang, Dinesh Bharadia, Kiran Joshi, and Sachin Katti. Hitchhike: Practical backscatter using commodity WiFi. In *Proceedings of the 14th ACM Conference on Embedded Network Sensor Systems CD-ROM*, page 259–271, 2016.